

**GREEN SYNTHESIS OF FLUORESCENT CARBON DOTS FROM PAPAYA
PEELS FOR PHOTOCATALYSIS AND ANTIBACTERIAL APPLICATION**

LIM JIN YI

**A project report submitted in partial fulfilment of the
requirements for the award of Bachelor of Engineering
(Honours) Chemical Engineering**

**Lee Kong Chian Faculty of Engineering and Science
Universiti Tunku Abdul Rahman**

April 2019

DECLARATION

I hereby declare that this project report is based on my original work except for citations and quotations which have been duly acknowledged. I also declare that it has not been previously and concurrently submitted for any other degree or award at UTAR or other institutions.

Signature : _____

Name : LIM JIN YI

ID No. : 1404644

Date : 2019-05-06

APPROVAL FOR SUBMISSION

I certify that this project report entitled **“GREEN SYNTHESIS OF FLUOROSCENT CARBON DOTS FROM PAPAYA PEELS FOR PHOTOCATALYSIS AND ANTIBACTERIAL APPLICATION”** was prepared by **LIM JIN YI** has met the required standard for submission in partial fulfilment of the requirements for the award of Bachelor of Engineering (Honours) Chemical Engineering at Universiti Tunku Abdul Rahman.

Approved by,

Signature : _____

Supervisor : _____

Date : _____

Signature : _____

Co-Supervisor : _____

Date : _____

The copyright of this report belongs to the author under the terms of the copyright Act 1987 as qualified by Intellectual Property Policy of Universiti Tunku Abdul Rahman. Due acknowledgement shall always be made of the use of any material contained in, or derived from, this report.

© 2019, Lim Jin Yi. All right reserved.

ACKNOWLEDGMENTS

The project would not be accomplished without the assistance and contribution from few parties. First and foremost, I would like to express my appreciation to my research supervisor, Dr. Sim Lan Ching for her precious advices, guidance and enormous patient throughout the project.

Besides, deepest gratitude to Universiti Tunku Abdul Rahman (UTAR) for providing platform and necessary equipment in completing my final year project. Moreover, I would like to thank the lab officers for their technical support during the experiment. In addition, thanks to the fruit hawker for providing the waste papaya peels needed for the research.

Last but not least, I would like to thank to my family and friends who had encouraged and assisted me during the project.

ABSTRACT

In this study, carbon dots (CDs) were successfully synthesised from papaya peels via hydrothermal treatment. The prepared CDs were used as photocatalysts to study the antibacterial performance in inactivation of *E.coli*. However, the bactericidal activity of CDs was indistinct as the blank sample displayed better disinfection rate over the CDs-added samples. The results implied ultraviolet-driven germicidal rate was higher than the germicidal rate of ROS produced by CDs. The outcome was suggested to be attributed to the high water solubility of CDs in aqueous solution which hindered its photocatalytic performance. Furthermore, CDs/g-C₃N₄ photocatalyst with different CDs' weight percentages had been synthesised by incorporating the prepared CDs into graphitic carbon nitride, g-C₃N₄. The composites prepared had been tested for their photocatalysis performance in Bisphenol A (BPA) photodegradation. Characterisations including Scanning Electron Microscopy-Energy Dispersive X-ray (SEM-EDX), UV-visible Diffuse Reflectance Spectra (UV-DRS) and Photoluminescence (PL) analysis, Fourier Transform Infrared Spectroscopy (FTIR) as well as X-ray Diffractometer (XRD) were carried out. The CDs/g-C₃N₄ exhibited broader light absorption range from UV to NIR spectrum over pure g-C₃N₄ due to the presence of CDs that acted as spectral sensitizers. Although CDs/g-C₃N₄ prepared did not show upconverted photoluminescence (UCPL) properties, the photosensitizing properties of CDs dominated the UCPL properties to improve the performance of BPA degradation. The photocatalytic performances of CDs/g-C₃N₄ photocatalysts were remarkably better than the pristine g-C₃N₄. The photodegradation rate was found to be increased with the loading of CDs. CDs/g-C₃N₄ with 20 wt.% of CDs achieved photodegradation rate as high as 86.04%, which was 30 % higher than the photodegradation rate of pure g-C₃N₄. The enhancement of photodegradation performance was ascribed to the efficient charge separation, wide light absorption range and narrowing of band gap by CDs. The scavengers test also revealed that superoxide radicals as well as holes were the main contributors in the photodegradation of BPA.

TABLE OF CONTENTS

DECLARATION	ii
APPROVAL FOR SUBMISSION	iii
ACKNOWLEDGMENTS	v
ABSTRACT	vi
TABLE OF CONTENTS	vii
LIST OF TABLES	x
LIST OF FIGURES	xii
LIST OF SYMBOLS / ABBREVIATIONS	xiv

CHAPTER

1	INTRODUCTION	1
	1.1 Conventional Wastewater Treatments for EDCs Removal	1
	1.2 Heterogeneous Photocatalysis	2
	1.3 Problem Statement	3
	1.4 Aims and Objectives	5
	1.5 Scope of Study	5
2	LITERATURE REVIEW	6
	2.1 Endocrine Disrupting Chemicals (EDCs) and <i>Escherichia Coli</i> (<i>E. coli</i>)	6
	2.2 Heterogeneous Photocatalysis	9
	2.2.1 Principle and Working Mechanisms of Heterogeneous Photocatalysis	9
	2.2.2 Photocatalyst	13
	2.3 Carbon Dots (CDs)	14
	2.3.1 Structures of Carbon Dots (CDs)	15
	2.3.2 Synthesis Route of Carbon Dots	15

	2.3.3	Hydrothermal Treatment	17
2.4		Graphitic Carbon Nitride (g-C ₃ N ₄)	20
	2.4.1	Structures and Properties of g-C ₃ N ₄	20
	2.4.2	Synthesis Route of g-C ₃ N ₄	21
2.5		Application of CDs	23
2.6		Photocatalytic Application of CDs/g-C ₃ N ₄ and CDs-Incorporated Photocatalysts	23
3		METHODOLOGY AND WORK PLAN	30
	3.1	Raw Materials and Chemicals	30
	3.2	Equipment and Instrument	31
	3.3	Overall Research Methodology and Flow Diagram	33
	3.4	Experimental Procedures	34
	3.4.1	Preparation of Carbon Dots (CDs)	34
	3.4.2	Preparation of Pure Graphitic Carbon Nitride (g-C ₃ N ₄)	35
	3.4.3	Preparation of CDs/g-C ₃ N ₄ Composites	35
	3.4.4	Characterisation of CDs/g-C ₃ N ₄ Composites	36
	3.4.5	Preparation of <i>E. coli</i> Culture	36
	3.4.6	Antibacterial Application of CDs	37
	3.4.7	Photocatalysis Degradation of BPA by CDs/ g-C ₃ N ₄ Composites	38
	3.4.8	Scavengers Test	39
4		RESULTS AND DISCUSSION	41
	4.1	Characterisation of Photocatalyst	41
	4.1.1	Scanning Electron Microscopy Equipped with Energy Dispersive X-ray (SEM-EDX)	41
	4.1.2	Fourier Transform Infrared Spectroscopy (FTIR)	44
	4.1.3	UV-vis and Photoluminescence Spectroscopy	48
	4.1.4	UV-visible Diffuse Reflectance Spectra (UV-vis DRS)	50
	4.1.5	X-ray Diffraction (XRD)	54

4.2	Antibacterial Application of CDs under Solar Irradiation	57
4.3	Application of CDs/g-C ₃ N ₄ Composites in BPA Degradation under Solar Irradiation	62
4.4	Scavengers Test	65
4.5	Costing and Sustainability	68
5	CONCLUSION AND RECOMMENDATIONS	70
5.1	Conclusion	70
5.2	Recommendations for Future Work	71
	REFERENCE	72
	APPENDICES	82

LIST OF TABLES

2.1	Types of EDCs, their Respective Sources and Health Effects	7
2.2	Types of Pathogenic <i>E.coli</i> and Their Respective Diseases	8
2.3	Advantages and Disadvantages of Different CDs Synthesis Methods	16
2.4	Treatment Conditions, Quantum Yield, and Applications of CDs Prepared from Different Types of Organic Precursors	19
2.5	List of Precursors and their Respective Treatment Temperatures	22
2.6	Summary of Literature Reports on the Degradation Efficiency CDs embedded Composites	26
3.1	List of Chemicals Used	30
3.2	List of Equipment Used	31
3.3	List of Instrument Used	32
3.4	Light Intensity during the Antibacterial Test	38
3.5	Light Intensity during the Photodegradation of BPA	39
3.6	Light Intensity during the Scavengers Test	39
4.1	Surface Elemental Composition of Photocatalysts	43
4.2	FTIR Table (Infrared Spectroscopy Absorption Table - Chemistry LibreTexts, 2014)	45
4.3	Summary of Band Gap Energy of Photocatalysts	52
4.4	Intensities of Diffraction Peaks at 2θ of $27. \times \times ^\circ$	54
4.5	Inactivation Rate of <i>E.coli</i>	58
4.6	Viable <i>E.coli</i> after 30 min	58
4.7	Viable <i>E.coli</i> after 60 min	59

4.8	Viable <i>E.coli</i> after 90 min	60
4.9	Viable <i>E.coli</i> after 120 min	61
4.10	Photodegradation Rate of BPA by CDs/g-C ₃ N ₄ Composites	62
4.11	Photodegradation Rate of BPA by CDs/g-C ₃ N ₄ Composites	68
4.12	Energy Consumption for Preparation of CDs and CDs/g-C ₃ N ₄	68
4.13	Material used for Preparation of CDs and CDs/g-C ₃ N ₄	69

LIST OF FIGURES

2.1	Schematic Diagram of Mechanisms of Heterogeneous Photocatalysis (Pawar and Lee, 2015.)	10
2.2	Schematic Diagram of Mechanism of Photocatalytic Disinfection (Wang, Yu and Wong, 2012).	13
2.3	Chemical Structure of Carbon Dots (Lim, Shen and Gao, 2015)	15
2.4	Tri-s-triazine (heptazine) structure of g-C ₃ N ₄ (Ong et al., 2016)	20
3.1	Flow Diagram of Research Methodology	34
3.2	Experiment Setup of Antibacterial Application	38
3.3	Experiment Setup of BPA Photodegradation	39
3.4	Experiment Setup of Scavengers Test	40
4.1	SEM images for (a) g-C ₃ N ₄ , (b) CDs/g-C ₃ N ₄ (0.10), (c) g-C ₃ N ₄ (0.15), (d) CDs/g-C ₃ N ₄ (0.20)	42
4.2	EDX results for (a) g-C ₃ N ₄ , (b) CDs/g-C ₃ N ₄ (0.10), (c) g-C ₃ N ₄ (0.15), (d) CDs/g-C ₃ N ₄ (0.20)	44
4.3	FTIR Spectra of CDs/g-C ₃ N ₄ Composite	47
4.4	UV-vis Absorption Spectrum of CDs Solution. Inset shows the Fluorescence of CDs under Daylight (Left) and UV Light Irradiation at 365 nm (Right)	49
4.5	Emission Spectra of CDs Solution under Different Excitation Wavelength	50
4.6	UV-DRS Absorption Spectra of g-C ₃ N ₄ and CDs/g-C ₃ N ₄ Composites	51
4.7	Tauc Plot of of g-C ₃ N ₄ and CDs/g-C ₃ N ₄ Composites	53
4.8	XRD Spectra of g-C ₃ N ₄ Composites	56

4.9	<i>E.coli</i> Inactivation Rate	58
4.10	Concentration of BPA across Time during Photodegradation by Photocatalysts	63
4.11	First-order Kinetic Plots of BPA Photodegradation by Photocatalysts	63
4.12	First-order Reaction Rate Constants of Photocatalysts	64
4.13	BPA Concentration across Time during Photodegradation for Scavengers Test	66
4.14	First-order Kinetic Plots of BPA Photodegradation for Scavengers Test	67
4.15	First-order Reaction Rate Constants of Photocatalysts for Scavenger Test	67

LIST OF SYMBOLS / ABBREVIATIONS

C_o	Initial concentration of BPA
C	Final concentration of BPA
DF	Dilution factor
$h\nu$	Photon Energy
λ	Wavelength
C_1	Concentration of stock solution, ppm
V_1	Volume of stock solution, mL
C_2	Concentration of diluted solution, ppm
V_2	Volume of diluted solution, mL
AOPs	Advanced oxidation processes
BPA	Bisphenol A
BQ	Benzoquinone
CB	Conduction band
CDs	Carbon Dots
CQDs	Carbon Quantum Dots
DMSO	Dimethyl sulfoxide
e^-	Electron
<i>E. coli</i>	<i>Escherichia coli</i>
EDCs	Endocrine disrupting chemicals
EDTA-2Na ⁺	Ethylenediamine-tetraacetic acid disodium salt
eV	Electron volt
FTIR	Fourier Transform Infrared
g-C ₃ N ₄	Graphitic carbon nitride
HPLC	High Performanace Liquid Chromatography
h^+	Positive hole
H ₂ O ₂	Hydrogen peroxide
$\cdot\text{HO}_2$	Hydroperoxyl radical
IPA	Isopropyl alcohol
$\cdot\text{O}_2^-$	Superoxide anion radical
$\cdot\text{OH}$	Hydroxyl radical
PL	Photoluminescence

QY	Quantum yield
SEM-EDX	Scanning Electron Microscopy-Energy
UPLC	Up-converted photoluminescence
UV	Ultraviolet light
UV-vis	UV-visible
UV-vis DRS	UV-visible Diffuse Reflectance Spectra
VB	Valence band
XRD	X-ray Diffractometer

LIST OF APPENDICES

APPENDIX A: Sample Calculations	82
APPENDIX B: EDX Results	85
APPENDIX C: FTIR Results	87
APPENDIX D: HPLC Results	92
APPENDIX E: Calibration Curve of BPA Concentration	93
APPENDIX F: XRD Results	94

CHAPTER 1

INTRODUCTION

1.1 Conventional Wastewater Treatments for EDCs Removal

Wastewater treatment is an essential process to treat the municipal and industrial wastewaters in order to meet the discharge standards with minimal environmental issues. The typical wastewater treatment plant is designed to remove the suspended solids, pathogens, organic matters, and nutrients. A conventional wastewater treatment plant comprises of physical, chemical, biological or the combination of these treatments to treat the wastewater. In recent years, the treatment of endocrine disrupting chemicals (EDCs) in wastewater has gained more concerns from the public. The current technologies for EDCs removal include activated sludge, activated carbon adsorption, membrane separation, chlorination and advanced oxidation processes (AOPs) (Ameta et al., 2018). Among them, activated sludge is the most common treatment unit for EDCs removal which applies the biological treatment concept. However, this method requires a longer hydraulic residence time to remove the estrogenic activities. Besides, a larger installation space for the aerobic and anaerobic ponds is needed (Mujtaba, Srinivasan and Elbashir, 2017). Moreover, some chemicals will be adsorbed onto the activated sludge and re-introduced into the environment if the bio-solids are used for the agricultural purpose (Scruggs et al., 2004.). In addition, chlorination also has been used for the EDCs removal and disinfection since it is cost effective. However, chlorination needs a long retention time and tends to form carcinogenic disinfection by-products (DBPs) due to the reaction between chlorine and EDCs (O'Shea and Dionysiou, 2012).

The membrane separation, activated carbon adsorption, and AOPs are the advanced technologies in the wastewater treatment system. In term of EDCs removal via granular activated carbon treatment, the major limitation of this technology is the requirement of regeneration and replacement after the activated carbon has reached the adsorption capacity. The EDCs adsorbed onto the carbon pores may also require additional treatment before it is disposed of. Moreover, the performance of the activated carbon unit will decline with the presence of natural organic matters which compete for the adsorption sites and block the pores (Lin, 2011). Another advanced technology for EDCs removal is membrane technology. However, this technology is

not widely applied in the wastewater treatment plants since it is very expensive and high energy intensive.

Advanced oxidation processes (AOPs) have first proposed in 1980 to treat the portable water and are then applied in the wastewater treatment (Deng and Zhao, 2015). Unlike other treatment processes, AOPs are chemical treatments processes which primarily designed to remove the inorganic and organic contaminants. It degrades the pollutants in the water by producing the oxidising agents such as hydroxyl ($\cdot\text{OH}$) radicals which can oxidise the pathogens, refractory organic pollutants and disinfection by-products (Balabanič et al., 2012). The main attractive points of AOPs over other treatment processes include a lesser amount of sludge produced, a fast reaction rate, non-selective oxidation and complete mineralization of pollutants (Krishnan et al., 2017). Furthermore, AOPs are more economically feasible compared to membrane separation and activated carbon treatment. There are six common types of AOPs including photocatalysis, electrolysis, radiation, sonolysis, Fenton-based treatment as well as ozonation (O'Shea and Dionysiou, 2012). Among these processes, ozonation and photocatalysis are more commonly discussed for their performance and capabilities in EDCs removal. However, the high energy demand for ozone generation has become one of the major drawbacks. Furthermore, bromate (carcinogenic substances) will form during ozonation if the water to be treated contains bromide (Aljundi, 2011). On the other hand, photocatalysis has attracted more concern in recent years as one of the alternatives for EDCs treatment process. Unlike ozonation, since the reaction can take place under an ambient condition with the presence of light, the energy requirement is low which make it economically feasible. Besides, the degraded products from the reaction are non-hazardous thus no secondary pollutants are produced (Chong et al., 2010).

1.2 Heterogeneous Photocatalysis

Photocatalysis is described as an acceleration of a photoreaction by adding of a catalyst. During a photoreaction, the molecules are broken down into smaller units as the result of light absorption. A photocatalyst can absorb the light energy or photons, generate charges carriers and transfer the energy to the desired reactants which causes a chemical transformation of the reactants (Khan, Adil and Al-Mayouf, 2015a). The electrons exist in the valance band (VB) will be excited to conduction

band (CB) and initiate a series of redox reactions when the light energy absorbed is equal or more than the band gap energy,. Consequently, powerful oxidants, hydroxyl radicals ($\cdot\text{OH}$) are formed by the oxidation of water or hydroxide ions. The photocatalyst itself will not be consumed or altered during the reaction. There are two types of photocatalysis which include homogenous photocatalysis and heterogeneous photocatalysis.

In this study, the focus will be given on the heterogeneous photocatalysis. A heterogeneous photocatalysis involves different phases of reactants and catalyst (Ameta et al., 2018). Metal oxides and semiconductors such as chromium (III) oxide (Cr_2O_3), vanadium dioxide (VO_2) and titanium dioxide (TiO_2) are the most common photocatalysts used in the heterogeneous photocatalysis (Umar and Aziz, 2013). Numerous studies on heterogeneous photocatalysis have been done in recent decades especially in environmental pollution and clean energy production fields. Researchers have found its effectiveness in the degradation of pollutants, carbon dioxide reduction, bio-related applications as well as solar water splitting. The implementation of heterogeneous photocatalysis in wastewater treatment process has drawn a large interest in recent years due to its ability in decomposing a wide range of contaminants. It has been classified as one of the AOPs which can generate reactive free radicals to oxidise the pollutants.

1.3 Problem Statement

The importance of clean water and sanitation has gained more concern in recent years as the concept of sustainable development arisen in the public. Water-borne diseases caused by the bacteria, viruses, and pollutants are the major causes of human morbidity and mortality in many under-development countries. Discharging of non-well treated municipal and industrial wastewater into the water bodies will lead to EDCs pollution. In this study, Bisphenol A (BPA) is adopted as the model pollutant because of its lethal health effects. For instance, BPA has found to be the culprits for several endocrine disorders such as infertility, increasing the risk for obesity, breast and prostate cancers as well as alteration in the immune function (Konieczna, Rutkowska and Rachoń, 2015).

Besides, *Escherichia coli* (*E. coli*) is identified as the model bacterium in this study because of the raising essential to remove it in the environment. The *E. coli* is commonly found in the water bodies via farm runoff and discharge of feedstock

manure. Accidentally consumption of *E. coli* can cause abdominal pain, diarrhoea and fever. Serious infection can lead to kidney injury and even death. Therefore, it is an urge to develop an effective treatment in order to remove the EDCs and pathogens in the wastewater before it is discharged into the water bodies and eventually entered the food chains.

Semiconductor graphitic carbon nitride, denoted as $g-C_3N_4$ is a fascinating photocatalysts used in pollutants degradation. It is well known for its moderate band gap, which is around 2.7 eV, with the corresponding wavelength of 460 nm (Wen et al., 2017). This moderate band gap allows absorption of light within the ultraviolet to near visible light range thus increases the photocatalytic activity under sunlight irradiation. Moreover, $g-C_3N_4$ consists of a conduction band position which is suitable for redox reactions. Apart from that, $g-C_3N_4$ also possesses other advantages such as high chemical stability, non-toxic, water-resistivity, biocompatibility and easy preparation with low cost (Dong et al., 2014). However, the $g-C_3N_4$ also encounter some limitations such as insufficient visible light absorption due to narrow light absorbance range, small total surface area and specific site for photoreaction as well as fast recombination rate of photo-induced charge carriers (Xu et al., 2018). These drawbacks have limited its performance in the photocatalysis.

Carbon dots (CDs) are chosen as the photocatalyst applied in the antibacterial experiment. Besides, CDs also selected as co-catalysts to overcome the limitations and shortages of the pure $g-C_3N_4$. CDs are well known for the up-converted photoluminescence (UPLC) properties, biocompatibility and wide absorption range between the UV, visible and near infrared region (NIR) (Wang and Hu, 2014). However, the high water solubility of pure CDs has limited its photocatalytic performance in an aqueous environment (Sim et al., 2018). Thus, CDs are incorporated into $g-C_3N_4$ to overcome its solubility problem. Besides, insufficient visible light absorption problem encountered by pure $g-C_3N_4$ can be tackled since CDs allow wider light absorption range in the entire solar spectrum.

In this study, papaya peels collected from the fruit stall will be used as the precursors to synthesize green carbon dots. The inappropriate disposal of the fruits waste could lead to hygiene issues, such as breeding of cockroaches and rat. Moreover, the degraded fruit wastes also associated with awful smell. The fruit wastes also contribute to the amount of rubbish thus require more resources and energy for disposal.

1.4 Aims and Objectives

The objectives of this study are stated below:

- (i) To prepare CDs from papaya peels using hydrothermal treatment.
- (ii) To characterize the physicochemical properties of CDs/g-C₃N₄ photocatalyst using various characterisation techniques.
- (iii) To investigate the photocatalytic degradation of BPA using the synthesised photocatalysts under irradiation of sunlight.
- (iv) To assess the antibacterial activities of CDs against *E. Coli*.

1.5 Scope of Study

The scope of study in this research include preparation of CDs through a green approach, synthesise CDs/g-C₃N₄ composites with different CDs weightage, characterisation of the prepared photocatalysts, evaluation of the antibacterial performance of CDs and photodegradation performance of CDs/g-C₃N₄. The CDs will be synthesised from waste papaya peels through hydrothermal treatment. Besides, g-C₃N₄ will be prepared via pyrolysis of urea. The characterisations of photocatalysts include UV-vis Absorption and Photoluminescence (PL) analysis, Field Emission Scanning Electron Microscope (FESEM), Fourier Transform Infrared (FTIR), X-ray Diffraction (XRD), as well as UV-visible Diffuse Reflectance Spectra (UV-DRS) analysis.

The prepared CDs will be applied in the inactivation of *E.coli* to study its antibacterial performance. Besides, the CDs/g-C₃N₄ will be used to photodegrade the Bisphenol A (BPA). The final concentration of BPA in the solution will be analysed by using High Performance Liquid Chromatography (HPLC). Scavengers test will be performed in order to find out the major radical species that involve in the photocatalysis. The main parameters that are going to be controlled for the antibacterial test by CDs is the CDs dosage while for the photodegradation test is the CDs loading in the CDs/g-C₃N₄ photocatalysts.

CHAPTER 2

LITERATURE REVIEW

2.1 Endocrine Disrupting Chemicals (EDCs) and *Escherichia Coli* (*E. coli*)

EDCs have been defined as the exogenous chemicals which are able to disrupt the normal functions and activities of natural hormones (Bergman et al., 2012). For instance, EDCs can interfere with the synthesis, secretion, metabolism and transport of the natural body-synthesised hormones (Gore et al., 2014). In wildlife, EDCs has altered the reproductive function and behaviour of the organisms. In the human being, alteration of the endocrine systems by EDCs will lead to many adverse health effects. For example, EDCs can cause abnormalities in reproductive and immune systems, neurobehavioral disorder, obesity and even development of cancers (Monneret, 2017).

According to the potential EDCs list reported by the Europe Commission, 320 out of 575 substances tested are found to be endocrine disruptors (Brussels, 2007). EDCs can be either natural compounds or synthetic products. However, they are mostly found in man-made chemicals such as industrial solvents, pharmaceutical agents, pesticides and even in the consumer products. Common examples of EDCs include bisphenol A (BPA), phthalates, polychlorinated biphenyls (PCBs), dioxins and dichlorodiphenyltrichloroethane (DDT). For instance, BPA is mainly produced and used in the plastics industry (polycarbonate plastic) and food can lining (epoxy resins) (Ribeiro, Ladeira and Viegas, 2017). BPA is identified to be detrimental to human health as it can act as an estrogen agonist and androgen antagonist which interrupt the normal cells' functions (Huang et al., 2012). Furthermore, some of the EDCs such as dioxin and PCB are persistence organic pollutants (POPs) and can bio-accumulate in the ecosystems.

Discharge of ineffectively treated wastewater from the industries, leakage of the EDCs from the disposed consumer products and leaching from landfill sites have found to be the major sources of EDCs water pollution. These chemicals will take up by the aquatic life and eventually enter the major food chain. Human being is exposed to EDCs via ingestion of contaminated water and food, skin contact, inhalation of polluted air, and transfer of EDCs from pregnant mother to foetus. The

types of EDCs, their respective sources and health effects are demonstrated in Table 2.1.

Table 2.1: Types of EDCs, their Respective Sources and Health Effects

Types of EDCs	Sources	Health effects	Reference
Bisphenol A (BPA)	Food can linings, plastic containers	Breast cancer, diabetes, obesity, liver and heart diseases	Huang et al., 2012; Konieczna, Rutkowska and Rachoń, 2015
Dioxin	Metal smelting, incineration of municipal wastes	Affect sperm quality and lower the sperm count, male infertility	Gore et al., 2014;
DDT	Pesticides, industrial waste	Obesity, reproductive, kidney and neurological diseases	Kabasenche and Skinner, 2014
Phthalates	Cosmetics, personal care products, medical tubing, detergent, lubricating oil	prostate disease and testicular cancer, diabetes, thyroid irregularities	Gore et al., 2014; Monneret, 2017
PCB	Lubricant, electrical insulator	Neurological disorder, testicular cancer, breast cancer	Helmfrid et al., 2012

Conventional wastewater treatments such as coagulation, flocculation, filtration and disinfectant are not purposely designed for EDCs removal. In recent years, advanced oxidation processes have gained more concern due to its high effectiveness in degrading a large range of pollutants via the redox reactions. The

fast reaction rate, mild end products and non-selective degradation with reasonable operating cost have made it become a promising technology for EDCs degradation.

The rod-shaped *Escherichia Coli* (*E. coli*) is type of gram-negative bacteria which belongs to the *Enterobacteriaceae* family (Buckle, 2015). The *E. coli* is often discharged into the surface water sources through untreated faeces and wastewater effluent. The sewage overflows, agricultural runoff as well as improperly treated effluent from farm and slaughterhouse are the main sources of the *E. coli* water pollution. The *E. coli* is normally used as the faecal indicator bacterium (FIB) to monitor the level of faecal contamination since it is the major microorganism present in the water bodies (Korajkic et al., 2013). The *E.coli* can be transmitted through the consumption of polluted food and water as well as person-to-person contact via the oral-faecal route.

The *E. coli* can either be pathogenic or commensal forms. The commensal *E. coli* are harmless to the humans and animals host. It colonises the gastrointestinal tract of the host and aids in the breakdown of specific carbon compounds (Lim, Yoon and Hovde, 2010). On the contrary, the pathogenic *E. coli* are carrying the virulence genes and will cause diseases. The *E. coli* pathotypes can be classified into six groups according to the host clinical symptoms and the virulence factor. For instance, the enterohaemorrhagic *E. coli* (EHEC) which belong to the *Shiga toxin producing E. coli* (STEC) is the culprit of haemorrhagic colitis (HC) as well as haemolytic uremic syndrome (HUS) which will give rise to severe renal failure and even death (Jang et al., 2017). The types of pathogenic *E. coli* and their respective diseases are shown in Table 2.2.

Table 2.2: Types of Pathogenic *E.coli* and Their Respective Diseases

Types of Pathogenic <i>E. coli</i>	Disease	References
<i>Shiga toxin-producing E. coli</i> (STEC)	Haemolytic uraemic syndrome (HUS), hemorrhagic colitis (HC)	Jang et al., 2017
<i>Enteroaggregative E. coli</i> (EAEC)	Persistent diarrhea, sporadic diarrhea, low-fever, nausea, borborygmi, tenesmus	Okhuysen and DuPont, 2010; Hebbelstrup Jensen et al., 2014

Table 2.2 (Continued)

<i>Enteropathogenic E. coli</i> (EPEC)	pediatric endemic diarrhoea	Ochoa and Contreras, 2011
<i>Enterotoxigenic E. coli</i> (ETEC)	Traveler's diarrhea, porcine and bovine diarrhoea	Palaniappan et al., 2006
<i>Enteroinvasive E. coli</i> (EIEC)	Watery diarrhea, dysentery	Palaniappan et al., 2006
<i>Diffusely adherent E. coli</i> (DAEC)	Diarrhea in children	Palaniappan et al., 2006

2.2 Heterogeneous Photocatalysis

Heterogeneous photocatalysis has developed rapidly in the last few decades after the photocatalytic water splitting on TiO₂ electrodes was firstly proposed by Honda and Fujishima in 1972 (Fujishima and Honda, 1972). Its applications in environmental remediation, water splitting and carbon dioxide reduction have drawn much attention from the researchers. Heterogeneous photocatalysis is belonging to the advanced oxidation processes (AOPs) family and is applied in the wastewater treatment for pollutants removal and antibacterial purposes. It is an alternative for the conventional wastewater treatment plant for both pathogens and pollutants removal since no residues of the organic pollutants, disinfectant by-products (DBPs) and sludge are produced (El Saliby et al., 2016). Besides, the complete degradation of pollutants, ambient operating conditions as well as low operating cost also extended its application in wastewater treatment (Chong et al., 2010).

2.2.1 Principle and Working Mechanisms of Heterogeneous Photocatalysis

Heterogeneous photocatalysis is described as a catalytic process that speeds up the photochemical reaction rate in the presence of the photocatalyst (Ibhadon and Fitzpatrick, 2013). It works by degrading the pollutants via a series of redox reactions when the pollutants come into contact with the photocatalysts under light irradiation. The steps involved in the photocatalysis include the light absorption by the photocatalyst, generation of electron-hole pairs, separation of charge carriers followed by the degradation of pollutants (Zhu and Wang, 2017).

As shown in Figure 2.1, heterogeneous photocatalysis is initiated by the absorption of photons by the photocatalyst. When the photocatalyst absorbs the photons ($h\nu$) having the same amount or higher energy than its band gap energy, the electrons (e^-) present in the valence band (denoted as VB) will be excited into conduction band (denoted as CB), causing formation of the electron-hole pairs (Molinari et al., 2017). The positive holes (h^+) left behind in the VB and electrons in the CB will move toward the photocatalyst's surface. However, some of the positive holes in VB will recombine with the electrons in CB owing to the electrostatic force. Heat is generated and the subsequent redox reactions are terminated due to the recombination of photo-induced charges carriers (Pawar and Lee, 2015.). Therefore, in order to achieve a good performance of the photocatalytic activities, the recombination rate has to be controlled by either doping or surface passivation. Equations 2.1 and 2.2 show the chemical equations of electron-hole formation and recombination respectively.

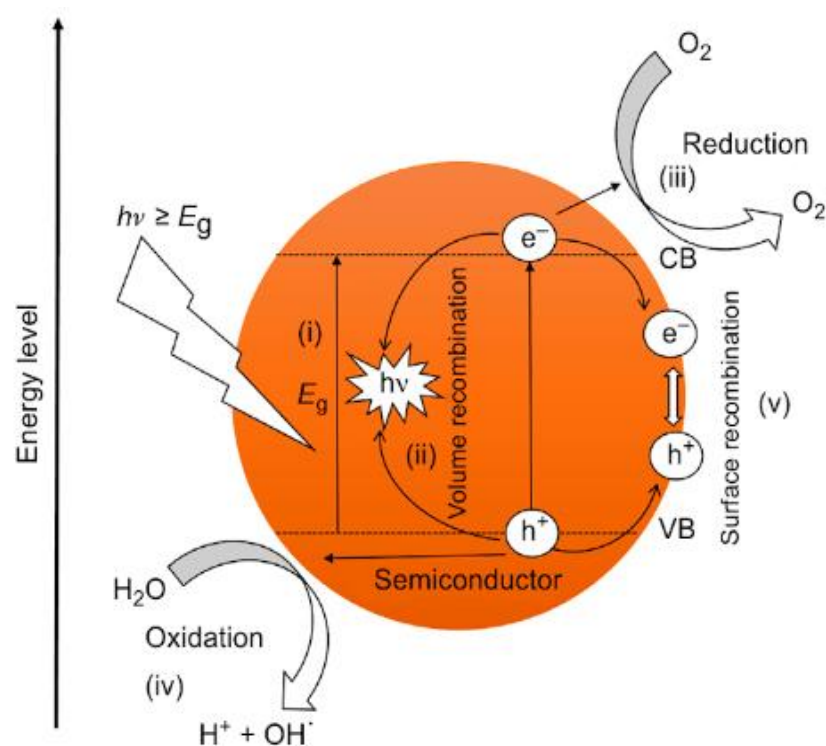
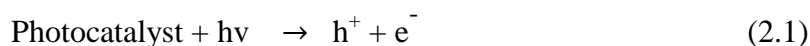


Figure 2.1: Schematic Diagram of Mechanisms of Heterogeneous Photocatalysis (Pawar and Lee, 2015.)

Formation of electron-hole pairs:

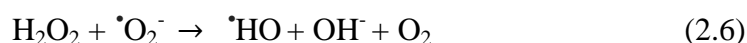


Recombination of electrons and holes:



The holes and electrons (charges carriers) at the surface of the photocatalyst will undergo a series of reduction and oxidation to produce highly reactive radicals which eventually oxidize the adsorbed pollutants (Yasmina et al., 2014). The electrons reduce the oxygen molecules into superoxide radical ($\cdot\text{O}_2^-$). The reaction between $\cdot\text{O}_2^-$ and hydrogen ions in the water forms the intermediate hydroperoxyl radicals ($\cdot\text{HO}_2$). Then, $\cdot\text{HO}_2$ will further react with $\cdot\text{O}_2^-$ to produce hydrogen peroxide (H_2O_2), which is a strong oxidizing agent. The reaction between $\cdot\text{O}_2^-$ and H_2O_2 results in more hydroxyl radicals ($\cdot\text{OH}$) being produced. The strong oxidizing radicals will degrade the pollutants into water and carbon dioxide. The series of chemical equations of the pollutants degradation are shown in Equations 2.3 to 2.8 (Wong, 2017).

Formation of reactive radicals:



Degradation of pollutants:

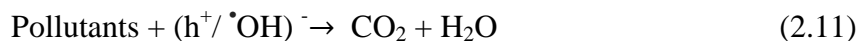


In addition, the positive holes will also take part in the water remediation. The holes can oxidise both the water molecules and hydroxide ions into hydroxyl radicals ($\cdot\text{OH}$). Besides, the holes can also directly oxidise the pollutants into carbon dioxide and water (Umar and Aziz, 2013). The chemical equations involved are shown in Equations 2.9 – 2.11.

Formation of hydroxyl radicals:



Degradation of pollutants:



In the application of photocatalytic disinfection, the reactive oxygen species (ROS) including holes, hydroxyl radical, superoxide radical anion, and hydrogen peroxide are responsible for the inactivation of the protozoa, gram positive bacterial, gram negative bacteria and viruses (Carré et al., 2014). The ROS will attack the cell membrane of the viruses and pathogens. The damaged cell membrane leads to leakage of electrolytes and intercellular components such as protein, RNA, and potassium ions (K^+) which are vital for the bacteria survival (Foster et al., 2011). This has made photocatalysis a potential candidate for disinfection treatment in the wastewater treatment plants. Photocatalytic disinfection can render a high disinfection performance without the formation of DBPs which are normally found in the conventional disinfection treatment. Besides, the photocatalytic disinfection is lower in cost compared to the conventional water disinfection treatments such as ozonation and chlorination which require expensive chemicals and equipment (Ouyang et al., 2016). Figure 2.2 illustrates the working mechanism of photocatalytic disinfection by a photocatalyst.

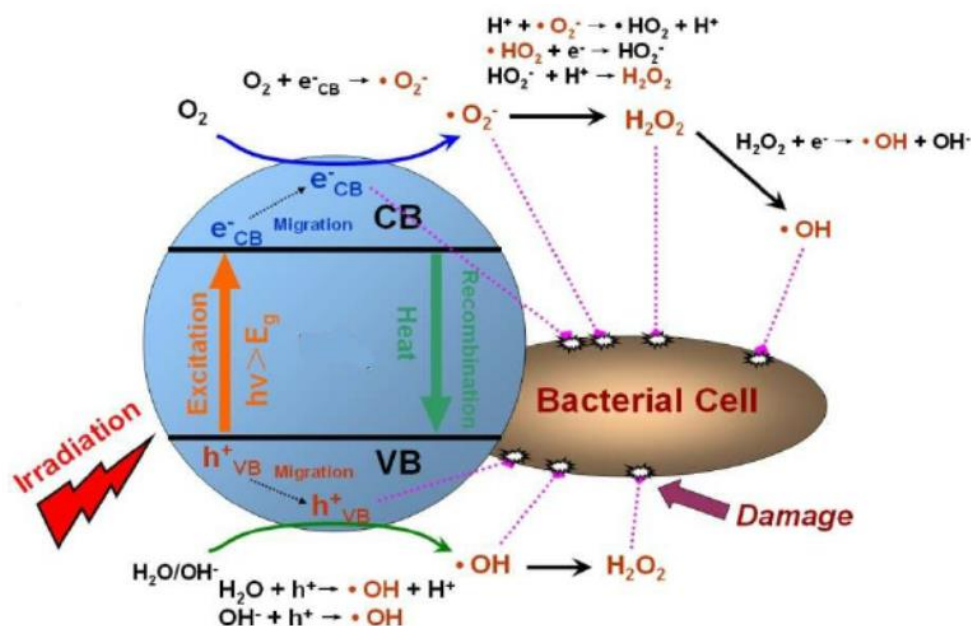


Figure 2.2: Schematic Diagram of Mechanism of Photocatalytic Disinfection (Wang, Yu and Wong, 2012)

2.2.2 Photocatalyst

A photocatalyst is essential to initiate a photocatalytic reaction. It is defined as a substance which absorbs photons from light source and forms electron-hole pairs to initiate the chemical reactions of the reactants with itself remains chemically unchanged after the reaction (Khan, Adil and Al-Mayouf, 2015b). The photocatalytic performance of the photocatalyst depends on its physiochemical properties which include the morphology, chemical composition, electronic structure arrangement, and band gap energy. In addition, other factors such as the physical stability, toxicity, light harnessing, charges recombination rate and charges transport property, availability as well as economic feasibility also have to take into consideration for the selection of a photocatalyst.

Conventionally, semiconductor materials have been used as the photocatalysts in a photocatalytic reaction. For instance, heterogeneous photocatalysts such as zinc oxide (ZnO), tin (IV) oxide (SnO₂), titanium dioxide (TiO₂), and cerium (IV) oxide (CeO₂) have shown their high efficiency in water remediation, water splitting, antibacterial and hydrogen production fields. Among them, TiO₂ is the most fascinating photocatalysts attributed to its chemical inertness, cost compatibility, high quantum yield and photostability. However, there are few challenges of using TiO₂ as a photocatalyst in practical applications. The limitations

include its low adsorption of hydrophobic pollutants, high aggregation tendency, fast recombination rate of charges carriers, deactivation as well as difficult separation and recovery in the post-treatment process (Dong et al., 2015). Besides, the low exploitation of visible light due to its wide band gap (around 3.2 eV) has restricted its performance under solar irradiation. This is because the wider band gap is more efficient in harvesting UV light (280-315 nm) instead of visible light (400-700 nm) (Shon et al., 2008). However, UV light only attribute to 5% of the entire solar spectrum while visible light attribute to 45% (Kumar, Karthikeyan and Lee, 2018a). In order to overcome this limitation, alteration of the band gap by shifting the absorption band from ultraviolet light to visible light region is required. This can be done by doping TiO₂ with transition metal, for example, vanadium (V), chromium (Cr) and nickel (Ni) (Ibhadon and Fitzpatrick, 2013).

Apart from titanium dioxide, zinc oxide (ZnO) is another type of photocatalyst which is widely used in the photocatalysis. ZnO has bandgap energy of 3.34 eV at room temperature, which is very similar to the band gap of TiO₂. Therefore, its photocatalytic capabilities are similar to TiO₂ as well (Nazarkovsky et al., 2017). However, ZnO is cheaper than TiO₂ which is more economically feasible in the practical applications. Besides from facing the same limitations such as rapid recombination rate of photogenerated charges and broad band gap as TiO₂, ZnO is prompt to photocorrosion (Lee et al., 2016). Moreover, cerium (IV) oxide, CeO₂ also shows a strong redox capability, non-toxicity and long-term stability properties which make it one of the promising photocatalysts (Ravishankar et al., 2015).

2.3 Carbon Dots (CDs)

Carbon dots (CDs) also termed as carbon quantum dots (CQDs) or carbon nanoparticles (CNPs), are a type of carbonaceous compounds with sizes smaller than 10 nm and spherical in shape (Gao et al., 2016). CDs are fluorescent nanomaterials which have excellent multi-photon excitation (up-conversion), highly tunable photoluminescence (PL), and impressive electron transfer properties (Himaja, Karthik and Singh, 2015). Carbon dots have drawn many attentions after its discovery during the purification of single-walled carbon nanotubes by Xu et al. (2004). It served as an alternative to the semiconductor-based quantum dots which are mostly toxic and high in production cost. The CDs have excellent optical properties, high photostability and aqueous solubility. Moreover, it is biocompatible,

non-toxic, and easy to synthesize with low cost. These properties have made CDs as the potential candidates for bioimaging, biosensing, and drug delivery applications (Himaja, Karthik and Singh, 2015).

2.3.1 Structures of Carbon Dots (CDs)

Carbon dots are commonly quasi-spherical in shape with sizes smaller than 10 nm. The structural arrangement can range from amorphous to nanocrystalline, depending on the precursors and synthesis methods. The CDs consist of sp^2/sp^3 carbon and oxygen-containing groups (Huang et al., 2017). The proposed structure of CDs is illustrated in Figure 2.3. CDs are also found to be attached with different functional groups including carboxyl, hydroxyl, carbonyl, epoxy and aldehydes groups (Himaja, Karthik and Singh, 2015). The hydroxyl, carboxyl have contributed to the water solubility and polymerization ability of the CDs (Zuo et al., 2015).

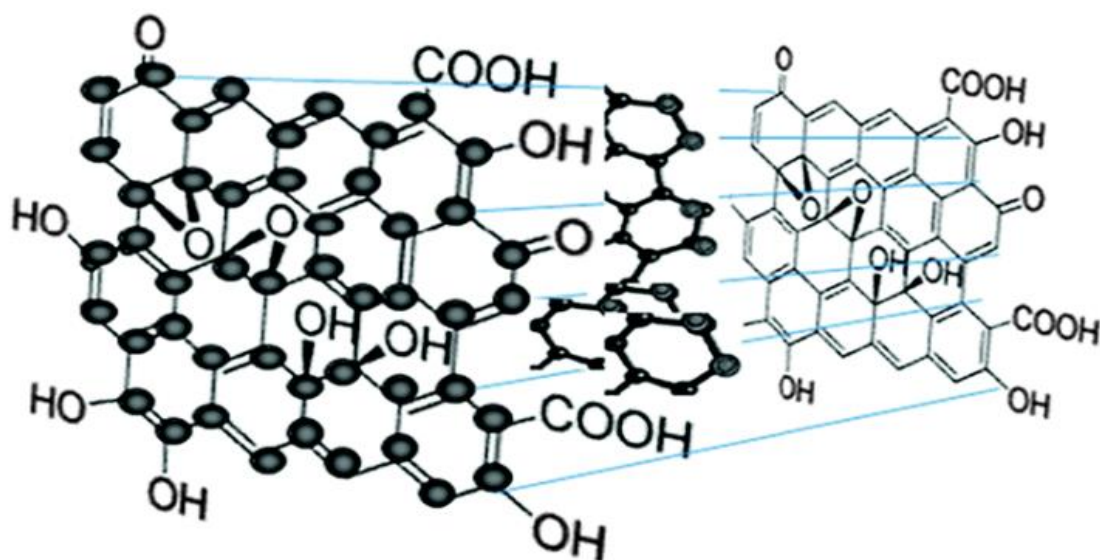


Figure 2.3: Chemical Structure of Carbon Dots (Lim, Shen and Gao, 2015)

2.3.2 Synthesis Route of Carbon Dots

The synthesis routes of CDs can be separated into “top-down” and “bottom-up” methods. The top-down approach is to break down larger carbon structures such as carbon and graphite nanotubes into the nano-sized CDs. The top-down method that have been used in CDs preparation include arc discharge, laser ablation and electrochemical oxidation (Sun and Lei, 2017). The top-down approach can produce CDs with good carbon lattice. However, the quantum yield (QY) is lower. Besides,

other drawbacks of this method include harsh reaction conditions, costly materials and equipment as well as longer preparation time (Choi et al., 2018). On the other hand, in the bottom-up method, the CDs are produced from the other molecule precursors such as carbohydrates and citric acid under specific conditions such as supply of heat. The heat energy is used for the transformation of the precursors' molecular structure (Wu, Liu and Yuan, 2017). The CDs prepared from this method will possess higher QY with a more amorphous structure. This method renders the advantage in controlling the composition and physical properties of the CDs by altering the carbonization conditions and the types of precursors. Besides, it is lower in production cost and therefore suitable for large-scale CDs production. However, it is difficult to control the morphology and the size distribution of the CDs formed as the particles will tend to agglomerate due to their strong surface tension (Yang et al., 2013). The bottom-up carbonization approach includes thermal decomposition, microwave irradiation, pyrolysis and hydrothermal treatment. The disadvantages and advantages of different synthesis pathways are summarized in Table 2.3.

Table 2.3: Disadvantages and Advantages of Different CDs Synthesis Methods

Approaches	Synthetic Methods	Advantages	Disadvantages	References
Top-down	Laser ablation	Room temperature-synthesis, surface states tunable	Low quantum yield, poor control of particles sizes, lab-scale production	Wang and Hu, 2014; Eatemadi et al., 2014
	Chemical ablation	Various sources, easily accessible	Harsh conditions, poor control of particles sizes, drastic processes	Eatemadi et al., 2014
	Electrochemical oxidation	Controllable size, high yield	Complex operation	Khor, 2018

Table 2.3 (Continued)

Bottom-up	Microwave irradiation,	simple process, one-step, low cost and eco-friendly, short reaction time, scalable	Poor control of particle size	Eatemadi et al., 2014
	hydrothermal treatment	Rapid process with only one step, effective, low cost, non-toxic	Poor control of particle size	Eatemadi et al., 2014
	pyrolysis	Simple operation, inexpensive, clean, non-toxic, large-scale production, One-step synthesis	Non-uniform size distribution	Khor, 2018; Tan et al., 2014

2.3.3 Hydrothermal Treatment

Hydrothermal treatment is the most commonly used method for CDs preparation via the bottom-up approach. The hydrothermal treatment for CDs preparation was firstly proposed by Zhang, Liu and Liu (2010). In this novel report, the CDs with high PL of 6.79 % and diameter of 2 nm were prepared by the one-step hydrothermal treatment of L-ascorbic acid. Hydrothermal treatment has gained much interest in these few years because of its simple, one-step reaction, low cost, environmental friendly and non-toxic synthetic route (Vasimalai et al., 2018).

In a hydrothermal treatment, an organic precursor solution is sealed and allowed for reaction in an autoclave at both high pressure and temperature (Wang and Hu, 2014). In the autoclave, since the pressure is very high, the boiling point of the water or solvent is elevated and produces the pressurized saturated solvent. The high temperature allows more heat supply to the precursors which induce the crystallization of the graphitic core and condensation of the carbonaceous building blocks (Khor, 2018). Besides, functionalization will occur simultaneously with the hydrothermal carbonization.

In the green hydrothermal treatment carbonization (HTC), natural precursors such as soy milk, orange juice, chitosan, and oatmeal have been used for the

preparation of green CDs. For instance, as reported by Sahu et al. (2012), CDs with photoluminescent (PL) quantum yield (QY) of 26% have been synthesized via hydrothermal treatment by using orange juice as the precursor. Besides, amino-functionalized CDs with a QY of 46% were prepared by Yang et al. (2012) via the hydrothermal treatment of chitosan at 180 °C. The prepared CDs were found to achieve a low cytotoxicity and good biocompatibility, which is suitable for the bioimaging application. Table 2.4 shows the treatment conditions, quantum yield, and applications of CDs prepared from different types of organic precursors.

Table 2.4: Treatment Conditions, Quantum Yield, and Applications of CDs Prepared from Different Types of Organic Precursors

Precursor	Treatment Condition	Quantum Yield, QY (%)	Application	Reference
Orange juice	120 °C for 50 min	26	Bio-imaging	Sahu et al., 2012
Chitosan	180 °C for 12 h	46	Bio-imaging	Yang et al., 2012
Soy milk	180 °C	2.6	Bio-imaging, electrocatalysis	Zhu, Zhai and Dong, 2012
Oatmeal	200 °C for 3 h	37.4	Bio-imaging	Yu et al., 2015
Hair	200 °C for 24 h	10.75	Hg ²⁺ sensing	Guo et al., 2016
Papaya juice	125-170 °C for 12 h	7	Cell imaging	Kasibabu et al., 2015
Citric acid with poly(ethylenimine)	110 °C for 2 h	48.3	Bio-imaging, bio-sensing	Li et al., 2017
Folic acid	170-200 °C for 5 h	-	Detection of nitrates	Lin et al., 2018
Lemon juice	120 °C for 3 h	16.7	Cell imaging	He et al., 2018

2.4 Graphitic Carbon Nitride (g-C₃N₄)

Carbon nitride is a solid state compound with a high ratio of N:C. It is made up from heterocycles of C and N with heptazine or triazine rings connected via sp² bonded N atom or -NH- groups (Miller et al., 2017). The unique electronic, chemical and optical properties make g-C₃N₄ an emerging material to complement carbon material in various applications.

2.4.1 Structures and Properties of g-C₃N₄

At ambient condition, g-C₃N₄ with tri-s-triazine-base is discovered as the most stable allotrope of the carbon nitride. It is a metal-free, polymeric n-type semiconductor made up of C, N, and impurity H. Graphitic carbon nitride is a two dimension π -conjugated layer structure with a distance of 0.326 nm between two layers (Zhao et al., 2018). The stacking layers are held together via the Van der Waals force. As shown in Figure 2.4, each layer is made up of tris-s-triazine (C₆N₇) connected with planer amino groups (Wang et al., 2017a). The presence of hydrogen impurities in the g-C₃N₄ due to incomplete condensation has resulted in surface defections. These surface imperfections have improved the catalytic activity of g-C₃N₄ by promoting the electron transfer to the catalyst's surface (Zhu et al., 2014). The two-dimensional sheets g-C₃N₄ possess a narrow band gap of around 2.7 eV (equivalent to the wavelength of around 460 nm) with the CB and VB redox potential values of -1.1 eV and +1.6 eV respectively which make it suitable for solar harvesting (García and Navalón, 2017).

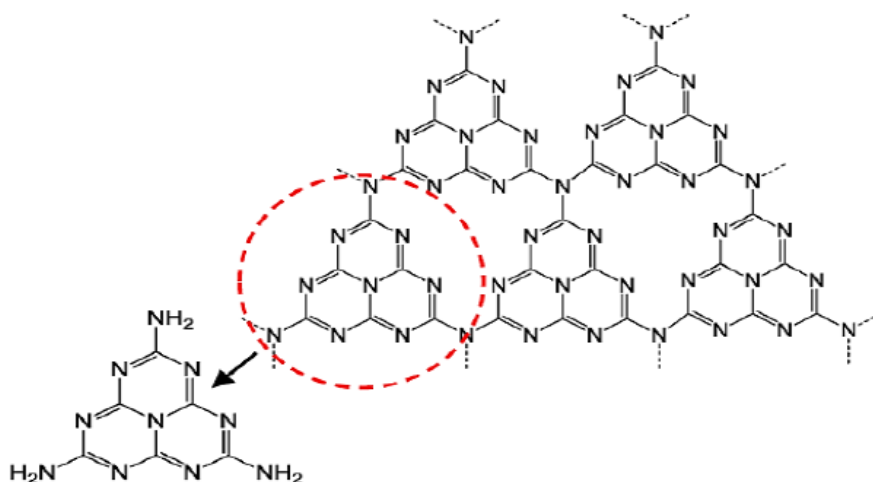


Figure 2.4: Heptazine (tri-s-triazine) structure of g-C₃N₄ (Ong et al., 2016)

Besides, g-C₃N₄ is rich in surface properties such as basis surface functional groups, electron-rich properties and H-bonding motifs which contribute to its practical application in catalysis (Schneider et al., 2016.). Furthermore, g-C₃N₄ shows a high chemical stability in both acid and alkaline solution. It is insoluble in water, toluene, ethanol, THF and diethyl ether because of the Van der Waals force acting between the layers stacking (Dong et al., 2014). In addition, g-C₃N₄ is reported to be thermally stable in the air that it is non-volatile up to 600 °C. The surface defects and nitrogen-rich sites provide active sites for substrate adsorption which improve the catalytic and photocatalytic performance (Kumar, Boukherroub and Shankar, 2018). Moreover, the ease of modification and functionalization, physiochemical stabilities, tunable optical properties (Kumar, Karthikeyan and Lee, 2018b), abundant in raw material, non-toxic and amenable for large-scale synthesis (Ong et al., 2016) also make g-C₃N₄ the most promising material in the water remediation and energy conversion industry.

2.4.2 Synthesis Route of g-C₃N₄

Graphitic carbon nitride can be fabricated by thermal nitridation, solid-state reaction, as well as vapour and chemical deposition. However, these synthesis methods require strict reaction conditions which make the process become more sophisticated (Dong et al., 2014). Thermal polymerization or thermal condensation is the facile and efficient synthesis pathway of g-C₃N₄. Pyrolysis is type of the thermal decomposition method to produce g-C₃N₄ at high temperature in the absent of oxygen. Nitrogen-rich and oxygen-free compounds such as melamine, urea, thiourea and cyanamide are used as the precursors in the pyrolysis. The nanostructure and physiochemical properties such as the porosity, specific surface area and PL of the g-C₃N₄ depend on the types of precursors used and the treatment conditions (Wang et al., 2017a). Yan et al. (2009) synthesised g-C₃N₄ from melamine by heating it at 500 °C for 2 h in a muffle furnace followed by the deammonation treatment at 500 - 580 °C. It is reported that the melamine was condensate at 297 - 390 °C and the further deammonation process has occurred at 545 - 630 °C. The treatment temperatures of the g-C₃N₄ preparation by using different precursors are shown in Table 2.5.

Table 2.5: Types of Precursors and their Respective Treatment Temperatures

Precursor	Treatment Temperature (°C)	Reference
Melamine, C ₃ H ₆ N ₆	500-580	Yan, Li and Zou 2009
Cyanamide, CH ₂ N ₂	550	Ong et al., 2016
Dicyandiamide, C ₂ H ₄ N ₄	550	Ong et al., 2016
Thiourea, CH ₄ N ₂ S	450-650	Ong et al., 2016
Urea, CH ₄ N ₂ O	520-550	Ong et al., 2016

The practical applications of pure g-C₃N₄ are hindered by few limitations. According to Zhao, Sun and Dong (2015), the surface area of g-C₃N₄ synthesised from these organic materials is usually below 10 m²/g, which is considered quite small for the catalytic process as the insufficient surface area would lead to lesser substrate adsorption. Besides, the narrow band gap which only allows absorption of visible light up to 460 nm has resulted in a large portion of sunlight irradiation (red region of visible light) being unutilized (Kang et al., 2018). The rate of photocatalytic reaction of g-C₃N₄ also limited by the rapid recombination of the photo-induced charges carriers (Yong et al., 2015). Nevertheless, these limitations can be overcome by doping with metal or non-metal impurities, formation of mesoporous structures and surface coupling hybridization as well as modification by carbonaceous components such as graphene oxide and carbon dots (Wang et al., 2017d). Doping with metal or non-metal atoms can improve the visible light harvesting properties by shifting the absorption range towards longer wavelengths. Furthermore, the formation of heterostructure can restrict the charges recombination rate and increase the quantum efficiency of the g-C₃N₄ (He, 2015). The mesoporous g-C₃N₄ also shows a high quantum efficiency with significant surface area which renders better light absorption induced by the internal scattering of the incident light (Kumar, Karthikeyan and Lee, 2018b). For instance, Zhu, Ren and Yuan (2015) have investigated the photocatalytic properties of the mesoporous phosphorus/g-C₃N₄. It is reported that the recombination rate of the charge carriers was impeded. This is attributed to the doping effect which has enhanced the relocalization of the electrons on the surface terminal sites. Besides, the interconnected nanosheets have reduced the diffusion distance of charges migration. Besides, the mesopores have provided

extra active sites for substrates adsorption which significantly improves the photocatalytic activity.

2.5 Application of CDs

Carbon dots have been studied widely in biomedical fields such as bio-sensing, bio-imaging and drug delivery due to its non-toxicity, good aqueous solubility, multi-colour photoluminescence (PL) and prominent biocompatibility (Emam et al., 2017). For instance, in the study done by Zhai et al. (2012), CDs have been utilized in the bio-imaging to label the L929 cell, which presents in the mouse and often used for toxicity testing. Besides, Zhu et al. (2012) also conducted a study on the two-photon fluorescence imaging of the MC3T3-E1 cells by utilizing near-infrared (NIR) excitation and carbon dots as the fluorescent probes. It was reported that the synthesized CDs showed an excellent photostability as no reduction in the PL was noticed after continuous excitation for 20 min. Moreover, the two-photo luminescence imaging of CDs internalized in human breast cells was studied by Cao et al. (2007). Additionally, many pieces of research also proposed CDs as a promising carrier for drug delivery. For example, Zeng et al. (2016) have demonstrated a localized cancer therapy in the mouse model by using the green light-emitting carbon dots as the trackable drug delivery carrier.

Apart from that, CDs application in molecules and metal ions sensing have also been studied. The PL properties of CDs can aid in the detection of molecules (Zhang and Yu, 2016). For example, the fluorescent aerogels dotted CDs with a QY of 40% has been used for nitrogen dioxide (NO₂) gas sensing (Wang et al., 2013b). Additionally, the use of CDs in antibacterial activity has been discussed by Jhonsi et al. (2018). In this report, CDs derived from and calf thymus DNA and m-tamarind have shown excellent antibacterial and antifungal performances in destroying both *C. albicans* and *E. coli* with an inhibition zone of 7–12 mm. Nevertheless, studies regarding the performance of CDs in disinfection applications are very limited despite its intriguing antibacterial properties.

2.6 Photocatalytic Application of CDs/g-C₃N₄ and CDs-Incorporated Photocatalysts

In this study, the CDs are incorporated into g-C₃N₄ to complement the shortages of each other in photocatalytic performances. The high water solubility of pure CDs

inhibits its practical applications in aqueous solution. To overcome this drawback, the insoluble g-C₃N₄ is used as a supported media to attach with CDs. Additionally, incorporation of CDs into g-C₃N₄ has embellish the photocatalytic performance which makes CDs/g-C₃N₄ an intriguing material for many photocatalytic applications. As mentioned previously, the fast recombination rate of electrons-holes pairs has limited the photocatalytic-related applications of the pristine g-C₃N₄. As a solution to this problem, an effective and efficient separation of the electron-hole pairs is desired. CDs can act as the effective electron-transfer material to assist the separation of the electron-hole pairs (Wang et al., 2017b). Besides, CDs can increase the quantum efficiency (QE) by broadening the solar-absorption range of the g-C₃N₄. Moreover, the CDs/g-C₃N₄ photocatalyst also able to raise the solar-to-hydrogen efficiency in the photocatalytic water splitting. In water splitting, CDs act as a co-catalyst for the hydrogen generation. Besides, it helps to prevent the poisoning of g-C₃N₄ by decomposing the hydrogen peroxide. This property is very useful in both water splitting and photocatalytic disinfection processes (Qu et al., 2018).

The CDs/g-C₃N₄ composite is a compromising material which can be used for various photocatalytic applications. Apart from the photocatalytic degradation of pollutant and disinfection, CDs/g-C₃N₄ is a potential photocatalyst which can be used for other purposes such as water splitting for hydrogen production, metal sensing, and photocatalytic degradation of dyes. Nevertheless, the studies regarding the applications of CDs/g-C₃N₄ composite are mostly focused on the water splitting performance regardless of its potential in other fields.

The water splitting is a promising technology for large scale hydrogen production with low production cost (Maeda and Domen, 2010). The utilization of CDs/g-C₃N₄ composites in the water splitting has been reported by Qu et al. (2018). It is found that the CDs has increased the charge separation efficiency of about 96% with the photoelectron transfer rate of $3.07 \times 10^9 \text{ s}^{-1}$, which significantly enhanced the hydrogen production performance. Furthermore, Wang et al. (2017d) has discussed the performance of L-ascorbic acid derived CDs/g-C₃N₄ in water splitting under UV light irradiation. It was reported that the hydrogen evolution rate has been improved due to the fast interface charges transfer.

Apart from water splitting, CDs/g-C₃N₄ also shows its potential to be used in the photocatalytic degradation. CDs/g-C₃N₄ is believed to improve the photodegradation of the pure g-C₃N₄. For example, the problem regarding

insufficient harvesting of visible light by pure $g\text{-C}_3\text{N}_4$ due to its narrow band gap can be overcome via incorporation of CDs. Moreover, CDs can function as the electron reservoirs thus restrain the recombination rate of charges carriers. According to study done by Wang et al. (2017b), the photocatalytic degradation of indomethacin by using CDs/ $g\text{-C}_3\text{N}_4$ was improved by the up-converted PL, narrowing band gap and efficient charge separation induced by CDs.

Apart from $g\text{-C}_3\text{N}_4$, there are studies about the incorporation of CDs with other materials to form photocatalyst composites. For example, Ke et al. (2017) has studied the performance of N-doped CDs/ TiO_2 in methylene blue (MB) degradation. It was reported that the degradation efficiency was 90 % within 120 min, which was higher than the pristine TiO_2 by 3.6 times. Moreover, Yu and Kwak (2012) also conducted research regarding the photocatalytic degradation of MB by using the CDs incorporated mesoporous hematite composites (CDs/MH). The photodegradation efficiency of MB was reported to be 97 % within 90 min. It was reported the surface area of the composites has risen to $187 \text{ m}^2/\text{g}$ and the charges recombination rate has reduced. Besides, the photocatalytic activity of CDs/ Fe_2O_3 composites against benzene gas has discussed by Zhang et al. (2011). In their research, the degradation efficiency of benzene gas was found to be improved from 37 % (pure Fe_2O_3) to 80% (CDs/ Fe_2O_3 /) due to the excellent UCPL of the CDs which promotes formation of photogenerated electron-holes pairs. Besides, it was reported that the conjugate network structure has enhanced the adsorption properties by the π - π interaction between the CDs and benzene molecules. The performances of CDs embedded photocatalysts are summarised in Table 2.6.

Table 2.6: Summary of Literature Reports on the Degradation Efficiency CDs embedded Composites.

Photocatalyst	Loading	Precursor	Organic Pollutant	Concentration of Initial Pollutant	Radiation Period (min)	Light Source	Degrade Efficiency (%)	Reference
CDs/TiO ₂	0 mL CDs	L-ascorbic acid	Methylene Blue	10 mg/L	120	500 W Xe lamp ($\lambda > 420$ nm)	32.4	Ke et al., 2017
	5 mL CDs						62	
	10 mL CDs						90	
	15 mL CDs						70	
CDs/Bi ₂ WO ₆	0 wt% CDs	Citric acid	Rhodamine B	10 ⁻⁵ mol/L	10	500 W Xe lamp	50	Zhang et al., 2017
	1 wt% CDs						69.7	
	3 wt% CDs						97	
	5 wt% CDs						95	
	0 wt% CDs						22.4	
	3 wt% CDs						33.4	

Table 2.6 (Continued)

CDs/MH	5 mL CDs	L-ascorbic acid	Methylene blue	20 mg/L	90	400 W halogen spotlight ($\lambda = 664$ nm)	97	Yu and Kwak, 2012
	0.0 wt% CDs							
	0.5 wt% CDs						40	
	1.0 wt% CDs						55	
CDs/BiOI	1.0 wt% CDs		Methylene orange	50 mg/L	50	150 W Xe ($\lambda = 420$ nm)	62	
	1.5 wt% CDs	Citric acid					98	Chen et al., 2016b
	2.0 wt% CDs						80	
CDs/Fe ₂ O ₃	-	-	Benzene	-	1440	Visible light	80	Zhang et al. 2011

Table 2.6 (Continued)

CDs/TiO ₂	0 mg						74.08	
	10 mg					8 W UV lamp	84.74	Chen et al.,
	20 mg	Starch	Rhodamine D	5 mg/L	120	($\lambda = 365$ nm)	91.28	2016a
	40 mg						86.92	

From the previous studies, it is discovered that the CDs were mostly applied in the bio-related sectors such as bio-imaging, drug delivery and bio-sensing due to its excellent biocompatibility and low cytotoxicity. On the other hand, the studies about the application of CDs in water remediation and antibacterial purposes are limited. Furthermore, it is found that the previous researches regarding the CDs preparation are mostly based on either L-ascorbic acid or a single, edible source, such as fruit juice, vegetables, flour and milk. Therefore, fruit waste (papaya peel) is used in this study as the precursor of CDs. Additionally, it is discovered there are limited studies regarding the incorporation of CDs into g-C₃N₄. Instead, previous researchers are more focused on the combination of CDs with other materials. Even for the studies about the CDs/g-C₃N₄ composites, most of them are focused on the water splitting performance. On the other hand, its applications in pollutants degradation are rarely discussed. Moreover, it is discovered that previous researches are mostly based on the use of artificial UV light to study the photocatalytic performance. In fact, this is not really practicable and economic feasible in real-life, large-scale applications since the generation of artificial UV light requires intensive energy and has to be conducted in a confined and protected space. By concluding the gap present in the literature, this research will emphasise on the application of the green CDs/g-C₃N₄ photocatalyst in photocatalytic degradation of pollutants by using sunlight as the sustainable driving energy. Moreover, the antibacterial properties of CDs in photocatalytic disinfection will also be studied in this research.

CHAPTER 3

METHODOLOGY AND WORK PLAN

3.1 Raw Materials and Chemicals

Biomass waste of papaya peels was selected as the precursor to synthesis CDs. The waste papaya peels were collected from the local fruit hawker in Sungai Long. The chemicals used in the experiment were of analytical grade and no further purification was needed. The *Escherichia coli* (*E. Coli*) was selected as the model bacterium while Bisphenol A (BPA) (Sigma Aldich, > 99 %) was selected as the model pollutant for the antibacterial and photodegradation experiments respectively. Besides, urea powder (Merck > 99 %) was used as the precursor for the preparation of graphitic carbon nitride (g-C₃N₄) via pyrolysis method. Distilled water had been used for preparation of CDs and CDs/g-C₃N₄ composites, cleaning and dilution in the experiment. The materials used are listed in Table 3.1.

Table 3.1: List of Chemicals Used

Chemicals	Purity (%)	Supplier	Purpose
Urea	99	Merck	Preparation of g-C ₃ N ₄
Ethanol	70	-	Sterilisation for the antibacterial application of CDs
Bisphenol A (BPA)	99	Sigma-Aldrich	Model pollutant for photodegradation test
Nutrient Broth	100	Merck	Preparation of <i>E.coli</i> culture
Nutrient Agar	100	Conda S.A	Preparation of agar plate
<i>E.coli</i>	100	ATCC [®] 25922 TM	Model bacterial antibacterial application of CDs

Table 3.1 (Continued)

Benzoquinone (BQ)	98	Sigma-Aldrich	Scavenger test (superoxide radical catcher)
Dimethyl sulfoxide (DMSO)	99	UniBar	Scavenger test (photo-induced electron catcher)
Ethylenediamine- tetraacetic acid disodium salt (EDTA-2Na ⁺)	98	Bio Basic Inc.	Scavenger test (holes catcher)
Isopropyl alcohol (IPA)	83.5	Bendosen	Scavenger test (hydroxyl radical catcher)

3.2 Equipment and Instrument

The equipment or devices used to prepare the photocatalysts and perform the experiment are listed in Table 3.2 while the instruments used for the photocatalysts characterisation are listed in Table 3.3.

Table 3.2: List of Equipment Used

Equipment/ Device	Purpose
Furnace	Preparation of g-C ₃ N ₄
Oven	Preparation of CDs and CDs/g-C ₃ N ₄
Sonicator	Preparation of BPA solution
Centrifuge machine	Separation of papaya peels residue from CDs solution Separation of <i>E.coli</i> from nutrient broth Separation of solid CDs/g-C ₃ N ₄ composites from the solution.
Shaking Incubator	Culture of <i>E.coli</i> for the antibacterial application
Incubator	Culture of <i>E.coli</i> in the agar plate

Table 3.2 (Continued)

Lutron LX-101 Lux meter	Measure the light intensity
Freeze Dryer	To dry the CDs solution into solid form

Table 3.3: List of Instrument Used

Instrument	Specification	Purpose
Fourier Transform Infrared Spectroscopy (FTIR)	Nicolet iS10	Identification of the functional groups present in the prepared CDs, g-C ₃ N ₄ and CDs/g-C ₃ N ₄ composite
High Performance Liquid Chromatography (HPLC)	Shimadzu LC-20A	Determination of the BPA concentration
Scanning Electron Microscopy-Energy Dispersive X-ray (SEM-EDX)	Hitachi Model S-3400N	Study of surface morphology and chemical elements present in the synthesised photocatalysts
X-ray Diffractometer (XRD)	Shimadzu XRD-6000	Identification of crystalline phase of in the synthesised catalyst
UV-vis Spectrophotometer	CARY 100	Study the light absorption properties of CDs
UV-visible Diffuse Reflectance Spectra (UV-vis DRS)	Shimadzu UV-2600	Comparison of the light-harvesting ability and band gap energy of the photocatalysts

Table 3.3 (Continued)

Photoluminescence (PL) spectroscopy	Perkin Elmer LS 55	Determination of the PL and UPLC properties of CDs
-------------------------------------	--------------------	--

3.3 Overall Research Methodology and Flow Diagram

The study comprises of two main parts include preparation of the photocatalysts and application of the prepared photocatalysts. Two types of photocatalysts (CDs and CDs/g-C₃N₄) were synthesised and the performance of CDs in antibacterial application as well as the performance of CDs/g-C₃N₄ composites in photodegradation of pollutant were studied. The project was performed according to the flow diagram showed in Figure 3.1.

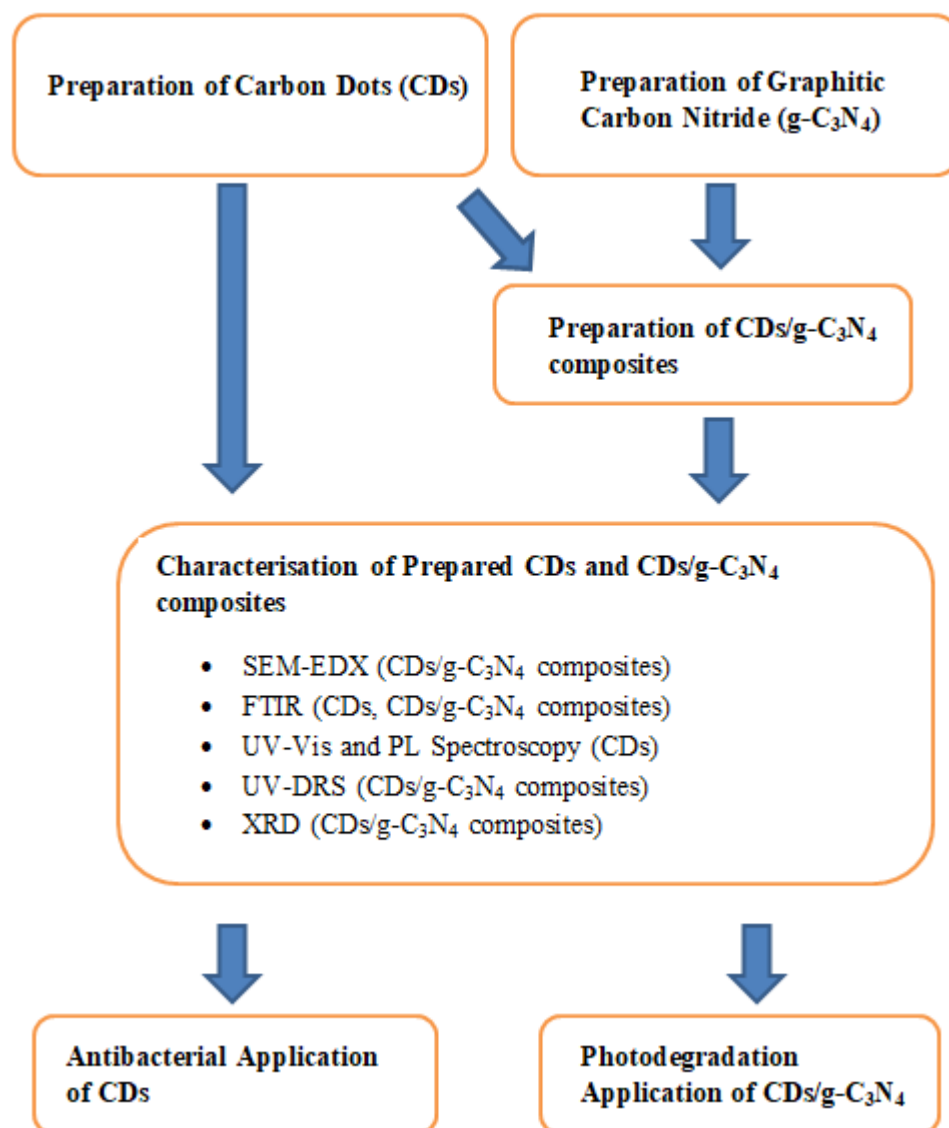


Figure 3.1: Flow Diagram of Research Methodology

3.4 Experimental Procedures

As mentioned, the experiment includes two main parts which are preparation of the photocatalysts and testing of their performance in antibacterial and photodegradation applications. The experimental works can be divided into the following sections:

3.4.1 Preparation of Carbon Dots (CDs)

The carbon dots (CDs) were prepared via the hydrothermal method. The preparation was carried out according to the procedure suggested by Khor (2018). The papaya peels collected were sliced into small pieces and heated in the oven at 80 °C overnight to remove the moisture content. Then, 5 g of the dried papaya peels pieces

was added into 100 mL distilled water. The mixture was then put into a 150 mL Teflon-lined stainless steel autoclave and was ready for hydrothermal treatment. It was heated at 200 °C for 4 h in the oven and then allowed to cool at ambient temperature. The obtained dark brown solution was then filtered with a 0.45 µm membrane filter to remove residues of papaya peels. Then, the filtrate was centrifuged at 5000 rpm for 15 min for further separation of the residues. The top layer of the centrifuged solution was extracted and freeze-dried for 24 h to remove the moisture content. The solid CDs produced were kept for further applications.

3.4.2 Preparation of Pure Graphitic Carbon Nitride (g-C₃N₄)

The g-C₃N₄ was prepared via pyrolysis. Urea powder was selected as the precursor for g-C₃N₄. The preparation of pure g-C₃N₄ was assimilated using Wong (2017) method. Firstly, the urea powder was placed into an alumina crucible and covered with the lid. The purpose of covering was to prevent the urea powder from reacting with the excess oxygen. The crucible was then wrapped with aluminium foil to prevent the g-C₃N₄ produced from escaping the crucible due to the suction in the furnace. The crucible was then heated in a furnace to 550 °C with a heating rate of 0.5 °C/min and was maintained at this temperature for 3 hours. The crucible was then cooled to the ambient temperature. The yellowish product, g-C₃N₄ formed was then ground into powder for the ease of storage and kept for future use.

3.4.3 Preparation of CDs/g-C₃N₄ Composites

The preparation of CDs/g-C₃N₄ photocatalysts was conducted based on the method suggested by Sim et.al (2018). In order to prepare composite with 10 wt% of CDs, 0.111 g of CDs was mixed with 1 g of pure g-C₃N₄. 70 ml of distilled water was added to dissolve the CDs and g-C₃N₄. The mixture was then transferred into a 150 ml Teflon-lined stainless steel autoclave, heated and maintained at 100 °C for 2 h. After that, the sample was allowed to cool down to room temperature. Then, the sample was centrifuged at 8000 rpm for 15 min and the top layer of the centrifuged solution was discharged while the residues were collected. The CDs/g-C₃N₄ composite was then left to dry at 60 °C overnight. CDs/g-C₃N₄ composites with different CDs concentrations (15 wt% and 20 wt%) were prepared by following the

same procedure. The samples prepared were denoted as CDs/g-C₃N₄ (0.10), CDs/g-C₃N₄ (0.15), CDs/g-C₃N₄ (0.20) according to the CDs concentrations.

3.4.4 Characterisation of CDs/g-C₃N₄ Composites

Photocatalyst characterisation is very important in order to understand the nature of the photocatalyst. The characterisation provided the information such as the composition, chemical structure and physiochemical properties about the photocatalyst. The knowledge regarding the characteristics of the photocatalyst was very important since it was directly related to the performance of the photocatalyst.

The scanning electron microscopy coupled with Energy Dispersive X-ray (SEM-EDX, Hitachi Model S-3400N) was used to obtain the topographical and elemental information of the CDs/g-C₃N₄ composites. The prepared photocatalysts were coated with a layer of gold by a sputter-coater machine. The SEM-EDX was run at accelerating voltage of 15 kV and SEM images were observed under magnification of 15000 \times . Besides, the functional groups of the CDs/g-C₃N₄ photocatalysts were determined by using the Fourier Transform Infrared (FTIR, Nicolet Is10) spectra. The analysis was performed at the infrared radiation with wavenumber ranged from 500 to 4000 cm⁻¹. The X-ray diffraction (XRD, Shimadzu XRD-6000) analysis was conducted to study the crystal structure of the photocatalysts. The samples were analysed in the range from 10 ° to 80 ° with a scanning speed of 1.2 ° per minute. Furthermore, ultraviolet diffuse reflectance spectra (UV-Vis DRS) of the CDs/g-C₃N₄ composites were performed using UV-vis NIR spectrophotometer (Shimadzu 2600) with a wavelength range of 200 nm to 800 nm. The UV-vis absorption of CDs solution was determined by using UV-vis spectrophotometer (CARY 100) within the wavelength range from 200 nm to 800 nm. The photoluminescence (PL) spectra of CDs solution were acquired with a PL spectrophotometer (Perkin Elmer LS 55) to explore the upconverted photoluminescence (UPLC) properties of the CDs solution. The PL analysis was conducted with excitation wavelengths ranged from 300 nm to 500 nm.

3.4.5 Preparation of *E. coli* Culture

The *Escherichia coli* (*E. coli*) culture was prepared according to the method suggested by Quek (2017). The preparation of *E. coli* was carried out in Laminar

Flow Chamber. Firstly, the *E. coli* was inoculated into a 100 mL nutrient broth. The culture medium was then incubated in the shaking incubator at 37 °C for 18 hours to allow the growth of the bacteria until a stationary phase. At this phase, the number of *E. coli* was maintained at the optimum value since equilibrium is achieved between the growth rate and death rate. After that, the culture broth was centrifuged at 5000 rpm for 15 min to separate the bacteria cells from the culturing medium. The separated cells were rinsed with sterilized 0.9 wt % saline water and the supernatant was disposed of. The cell density was controlled at 1×10^9 colony forming unit (CFU)/mL by using optical density (OD₆₀₀) measurements as well as dilution method as shown in the Appendix A.

3.4.6 Antibacterial Application of CDs

The antibacterial property of the CDs photocatalyst was investigated via photocatalytic disinfection under natural sunlight. The photocatalytic disinfection was carried out from 10 am to 12 pm in January 2019. 99 mL of 0.9 wt% saline water and 1 mL of *E. coli* stock solution (1×10^9 CFU/mL) was mixed well to prepare *E. coli* solution of 1×10^7 CFU/mL. Then, 0.1 g of CDs was added into the beaker and was stirred by a magnetic stirrer. After that, the mixture was placed in the dark for 30 min in order to reach an adsorption-desorption equilibrium. The mixture was then placed on the rooftop of UTAR KB block and covered with transparent glass shield to prevent contamination. The light intensity was measured by a Lutron LX-101 Lux meter and was recorded in Table 3.4.

The samples were collected every 30 min intervals for a duration of 2 h. The viable bacteria test was carried out by applying the spread plate method (Wang et al., 2013a). Each sample collected was filtered by using 0.45 µm membrane filters and successive diluted for four times. After that, 0.1 mL of the sample from every dilution was pipetted onto the surface of the agar plate. The sample was then spread evenly on the agar plate by placing the spreader on the surface of the agar while rotating the plate. Then, the agar plates are incubated overnight at 37 °C. The colony forming units (CFU's) was calculated by the aids of colony counting device. The number of viable *E. coli* presented in every mL of the original sample was calculated as shown in Appendix A.

Table 3.4: Light Intensity during the Antibacterial Test

Time Interval (min)	0	30	60	90	120
Light Intensity (100 lux)	984	827	1042	963	1129



Figure 3.2: Experiment Setup of Antibacterial Application

3.4.7 Photocatalysis Degradation of BPA by CDs/ g-C₃N₄ Composites

The performance of CDs/g-C₃N₄ photocatalyst was tested via the photocatalysis degradation of BPA under solar irradiation. The photocatalytic degradation was carried out from 10 am to 12 pm in February 2019. 0.1 g of CDs/g-C₃N₄ photocatalyst was added into a 200 mL solution with 20 mg/L of BPA. The solution was magnetically stirred in the dark and kept overnight to reach an adsorption-desorption equilibrium. After that, the mixture was placed under natural sunlight on the rooftop of UTAR KB block. The samples were taken every 30 min intervals for a duration of 2 h. The light intensity was recorded by using Lux meter and was shown in Table 3.5. The collected samples were then filtered with a 0.45 μm membrane filter to remove the composite residues. Finally, the samples were analysed with HPLC to determine the final concentration of the BPA. The column used was Hypersil GOLD (C-18, 250 mm × 4.6 mm, 5 μm). Mixture of water and acetonitrile (ACN) was used as the mobile phase with the water to ACN ratio of 60:40. Other conditions include temperature at 35 °C, injection volume of 1 μL and at the flowrate of 0.4 mL/min. The photodegradation rate of BPA was calculated by using Equation 3.1.

$$\text{Photodegradation rate, \%} = \frac{C_0 - C}{C_0} \times 100 \% \quad (3.1)$$

where

C_0 = initial concentration of BPA

C = final concentration of BPA

Table 3.5: Light Intensity during the Photodegradation of BPA

Time Interval (min)	0	30	60	90	120
Light Intensity (100 lux)	754	1077	1157	801	1006



Figure 3.3: Experiment Setup of BPA Photodegradation

3.4.8 Scavengers Test

Scavengers test was conducted to study the mechanism of the photocatalytic reaction by identifying the types of free radicals involved in the reaction. The scavengers used include benzoquinone (BQ), ethylenediamine-tetraacetic acid disodium salt (EDTA-2Na⁺), isopropyl alcohol (IPA) and dimethyl sulfoxide (DMSO). CDs/g-C₃N₄ (0.20) was chosen for the scavengers test due to its excellent performance in BPA photodegradation over other prepared photocatalysts. BPA solution with concentration of 20 ppm, mixed with CDs/g-C₃N₄ (0.20) and 0.002 moles/L of scavenger was prepared and magnetically stirred in dark for 24 h to achieve the adsorption-desorption equilibrium. The photodegradation was carried out for 2 h and the samples were taken every 30 min interval. The BPA concentrations of the samples were measured by using HPLC. Table 3.6 showed the light intensity recorded by Lux meter during the photodegradation experiment.

Table 3.6: Light Intensity during the Scavengers Test

Time Interval (min)	0	30	60	90	120
Light Intensity (100 lux)	769	1191	893	1187	920



Figure 3.4: Experiment Setup of Scavengers Test

CHAPTER 4

RESULTS AND DISCUSSION

4.1 Characterisation of Photocatalyst

Characterisation of CDs and CDs/g-C₃N₄ composites were conducted in order to study the physical and chemical properties of the prepared photocatalysts. The characterisations for CDs include FTIR, UV-vis and PL analysis while for CDs/g-C₃N₄ composites include SEM- EDX, FTIR, XRD and UV-vis DRS.

4.1.1 Scanning Electron Microscopy Equipped with Energy Dispersive X-ray (SEM-EDX)

The SEM was performed to study the surface morphology, topography and the structural properties of the pure g-C₃N₄ and CDs/g-C₃N₄ composites. The SEM images shown in Figure 4.1 were taken under the magnification of $\times 15.0k$. Figure 4.1 (a) shows the irregular crumpled lamellar structure of the pure g-C₃N₄ nanosheets with porous folding morphology. The wrinkled structure of the pure g-C₃N₄ offered good support for the attachment of the CDs as shown in Figure 4.1 (b-d). Besides, it was clearly showed that the CDs/g-C₃N₄ composites with higher CDs concentration exhibited more packed and agglomerated morphological nanostructure.

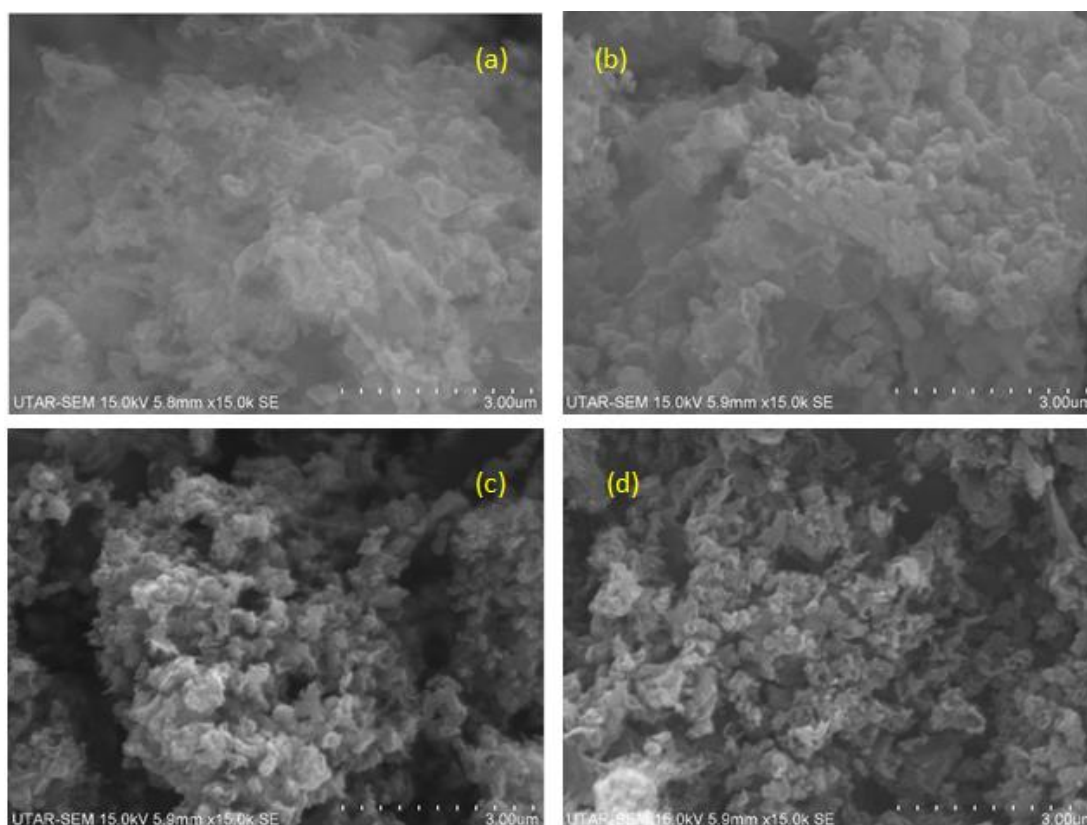


Figure 4.1: SEM images for (a) g-C₃N₄, (b) CDs/g-C₃N₄(0.10), (c) g-C₃N₄(0.15), (d) CDs/g-C₃N₄(0.20)

The surface composition and the concentration of the elements in the pure g-C₃N₄ and CDs/g-C₃N₄ were identified by using EDX analysis. Figure 4.2 depicts the EDX spectra while Table 4.1 summarises the surface concentrations of carbon (C), nitrogen (N) and oxygen (O) of the photocatalysts. In the data presentation, atomic percentage is shown instead of weight percentage. This is because the atomic percentage depending on the number of atom while the weight percentage is affected by the elemental atomic mass. In short, an element with a higher atomic mass would have higher weight percentage. The complete EDX results are shown in Appendix B. The detection of C and N elements indicated the presence of pristine g-C₃N₄ while the sharp peak of C was attributed to the presence of CDs (Amiri, Salehniya and Habibiyanjeh, 2016). Although the increment of C content did not increase with the concentration of CDs, it was observed that the C contents in all composites were higher than the pure g-C₃N₄. In addition, the presence of the O element in the pure g-C₃N₄ was mainly due to the reaction between the urea and oxygen during pyrolysis of the urea to prepare g-C₃N₄. In order to eliminate the O content, the pyrolysis shall be

conducted in argon gas environment. However, with the equipment constraint, such reaction condition was unable to be fulfilled. On the other hand, presence of O in the CDs/g-C₃N₄ not only ascribed to the oxidation during pyrolysis but also due to the content of O-containing functional groups in the CDs. This found out was tally with the FTIR results which revealed the presence of hydroxyl group in the composites.

Table 4.1: Surface Elemental Composition of Photocatalysts

Sample	Elemental Composition (at. %)		
	C	N	O
g-C ₃ N ₄	49.93	41.50	08.57
CDs/g-C ₃ N ₄ (0.10)	57.60	32.04	10.36
CDs/g-C ₃ N ₄ (0.15)	61.95	28.33	09.73
CDs/g-C ₃ N ₄ (0.20)	50.10	41.74	08.17

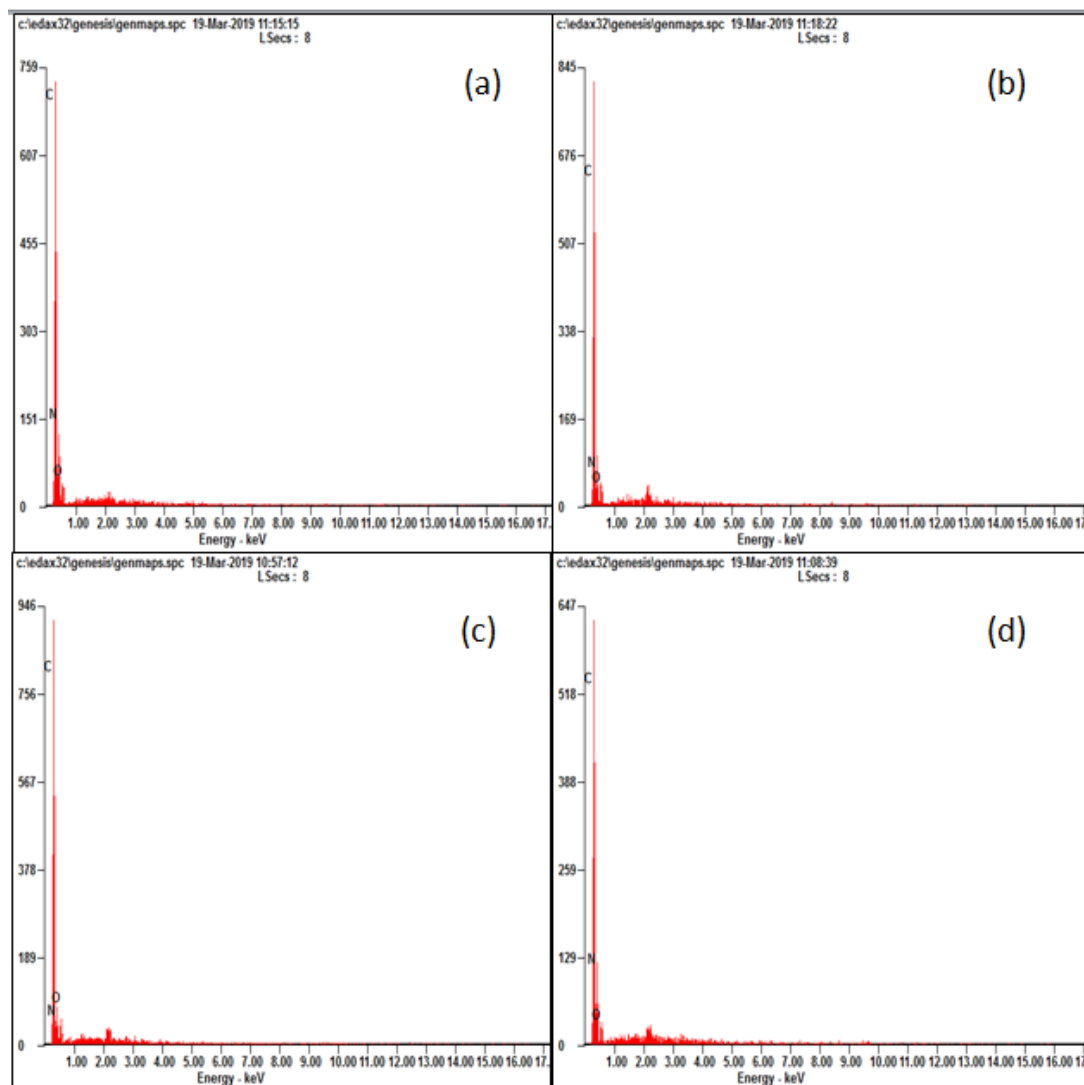


Figure 4.2: EDX results for (a) g-C₃N₄, (b) CDs/g-C₃N₄(0.10), (c) g-C₃N₄(0.15), (d) CDs/g-C₃N₄(0.20)

4.1.2 Fourier Transform Infrared Spectroscopy (FTIR)

The FTIR was conducted to identify the functional groups present in the synthesised photocatalysts. The analysis was performed in the wavenumber range from 500 cm⁻¹ to 4000 cm⁻¹. The types of vibrations were identified by referring to the wavenumber where the peak appeared to the IR table showed in Table 4.2. Figure 4.3 shows the FTIR spectra of the prepared photocatalysts. The FTIR spectra with distinct peak labels are attached in Appendix C.

Table 4.2: FTIR Table (Infrared Spectroscopy Absorption Table - Chemistry LibreTexts, 2014)

Wavenumber (cm ⁻¹)	Bonds	Vibration Types	Functional Groups
3350-3310	N-H	Stretching	Secondary amine
3300-2500	O-H	Stretching	Carboxylic acid
3200-2700	O-H	Stretching	Alcohol
1690-1640	C=N	Stretching	-
1650-1566	C=C	Stretching	Cyclic alkene
1650-1570	N-H	Bending	Amine
1385-1380	C-H	Bending	Alkane
1380-1390	C-H	Bending	Aldehyde
1250-1020	C-N	Stretching	Amine

For the FTIR spectra of CDs, a peak observed at 3233.33 cm⁻¹ was assigned to the O-H stretching of the alcohol and carboxylic acid group. Besides, the next peak observed at 1574.42 cm⁻¹ referred to the aromatic C=C stretching in the CDs structure. The C-H bending contributed to peak at 1385.50 cm⁻¹. Moreover, Wang et al. (2017c) also suggested the peak at 1385.50 cm⁻¹ was due to the vibration of carbonyl groups, C=O in the CDs. Peak occurred at 1068.20 cm⁻¹ corresponded to the C-N stretching. The FTIR spectrum again demonstrated that CDs was successfully synthesised from papaya peels.

In addition, for pure g-C₃N₄, the broad peaks between 3300 cm⁻¹ to 3100 cm⁻¹ were due to the stretching of primary and secondary amine group, N-H bonds and the interactions between intermolecular hydrogen bonding (Xin and Meng, 2013). The N-H vibrations denoted the existence of some uncondensed amine functional groups in the carbon nitride layer (Samanta et al. 2014). Besides, the peaks in the range of 1650 cm⁻¹ to 1200 cm⁻¹ with the exact peaks occurred at 1230.39 cm⁻¹, 1397.22 cm⁻¹, 1455.38 cm⁻¹ and 1629.06 cm⁻¹ were attributed to the stretching of sp³ C-N and sp² C=N bonds in the heptazine heterocycles. Moreover, the breathing mode of s-triazine unit contributed to the sharp peak at 806.56 cm⁻¹ (Lv et al., 2017).

For the CDs/g-C₃N₄ composites, the FTIR spectra were similar with the one of pure g-C₃N₄ as they were mainly composed of g-C₃N₄ and thus possess the same functional groups. The peaks in the range from 3300 cm⁻¹ to 3100 cm⁻¹ were

attributed to both stretchings of the N-H bonds and the O-H bonds. The O-H vibrations indicated the successful incorporation of CDs onto the surface of g-C₃N₄ due to substitution of hydrogen at the oxygen site H bond to the g-C₃N₄ lattice (Wong, 2017).

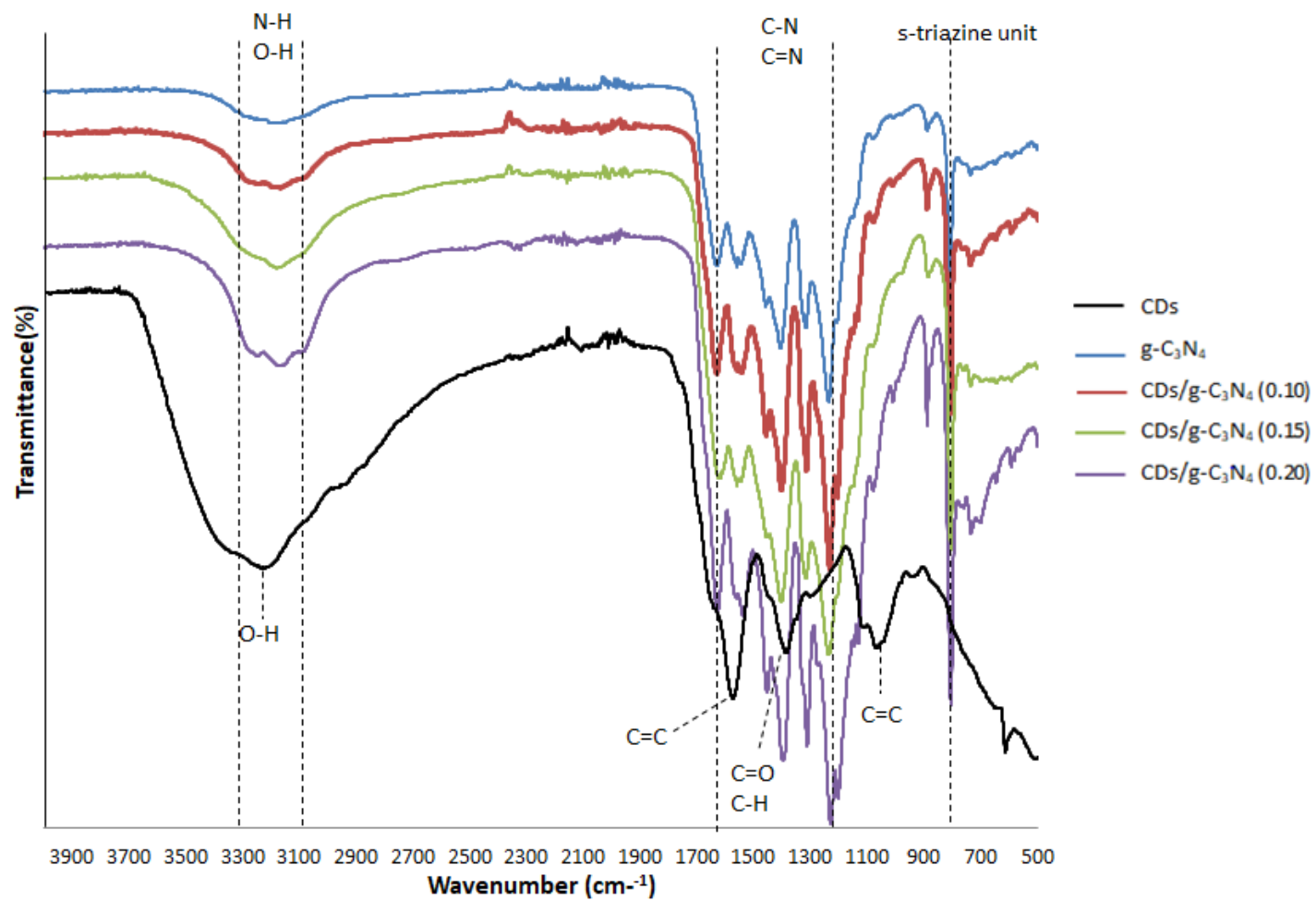


Figure 4.3: FTIR Spectra of Prepared Photocatalysts

4.1.3 UV-vis and Photoluminescence Spectroscopy

The UV-vis and photoluminescence spectroscopy was carried out to study the optical properties of the prepared photocatalysts. Figure 4.4 shows the fluorescence emission spectra and the UV-vis absorption of the CDs solution. As illustrated in the photo at the right corner of Figure 4.4, the original dark brown CDs solution under visible light exhibited bright green emission under UV excitation (365 nm) in dark room. Besides, UV-vis spectroscopy of CDs solution was conducted in the range from 200 nm to 800 nm. The broad peak appeared at around 315 nm to 340 nm was attributed to the $n-\pi^*$ transition of the C-O bonds (Vasimalai et al., 2018). The absorption intensity decreased gradually afterward indicated no carbonaceous materials had been formed from partial carbonization (Ramanan, et al., 2016).

Furthermore, the PL properties of CDs were studied by varying the excitation wavelength from 300 nm to 500 nm. Figure 4.5 illustrates the photoluminescence (PL) emission spectra of CDs across excitation wavelength from 300 nm to 500 nm. It was observed that the fluorescence emission peak of CDs appeared as a broad peak from UV region to visible light region. A strong PL emission peak was found at 400 nm with the excitation wavelength of 340 nm. Moreover, the emission spectrum was red-shifted to higher wavelength with decreased emission intensity when the excitation wavelength increased. However, no emission peak was found for excitation wavelength at 500 nm. The CDs prepared did not acquire the upconverted photoluminescence (UCPL) properties which can emit light at shorter wavelength than the excitation wavelength. The UCPL behaviour of CDs is attributed to the multi-photon activation process where two or more photons are absorbed simultaneously and lead to anti-Stokes type emission (Wang and Hu, 2014). In the study conducted by Wen et al.(2014), it was found that the CDs synthesized did not exhibit observable UCPL properties. Besides, it was suggested that the UCPL of CDs is actually the normal fluorescence with linear response rather than a multiple photon process and most of the CDs may not possess observable UCPL (Farshbaf et al., 2018). The plausible causes which affect the PL properties include the different particle sizes of the CDs, multiple distributions of the emissive site on the passivated CDs and the distribution of different surface energy traps and recombination of electron-hole pairs at the surface-confined defect states (De and Karak, 2013).

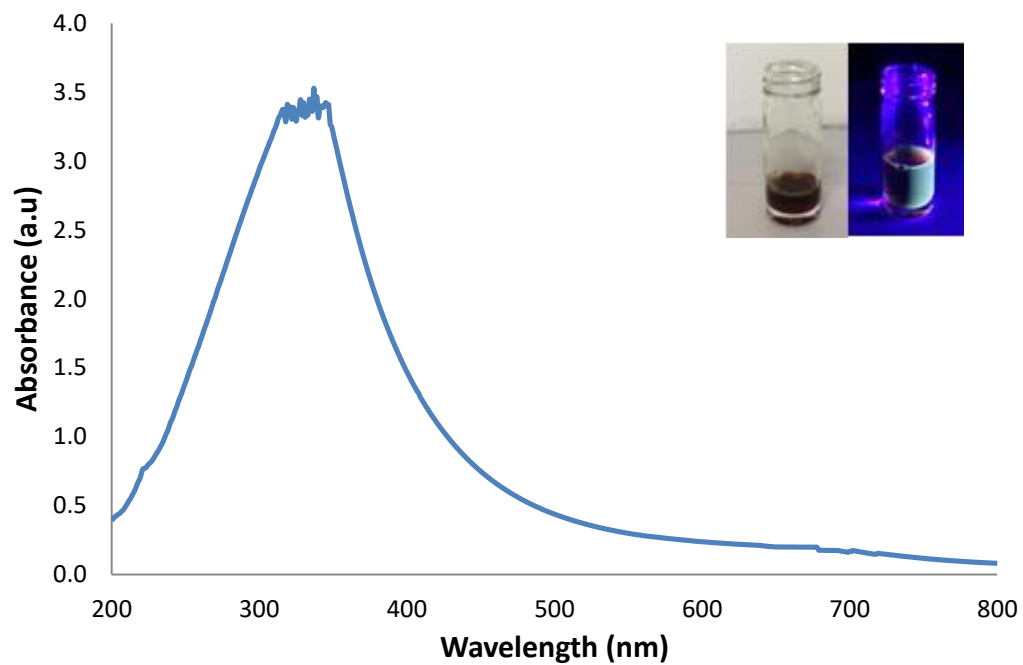


Figure 4.4: UV-vis Absorption Spectrum of CDs Solution. Inset shows the Fluorescence of CDs under Daylight (Left) and UV Light Irradiation at 365 nm (Right)

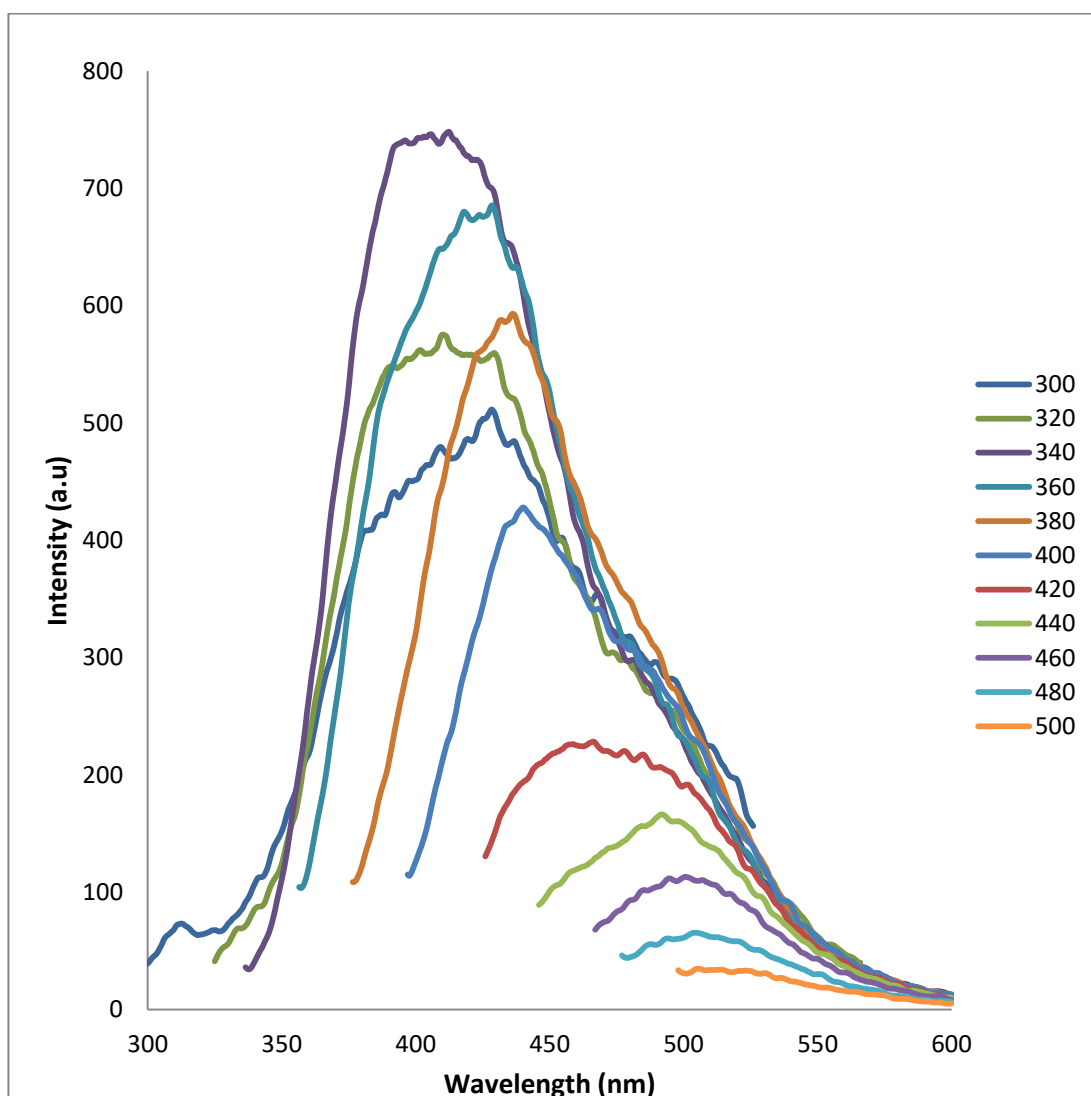


Figure 4.5: Emission Spectra of CDs Solution at Different Excitation Wavelengths

4.1.4 UV-visible Diffuse Reflectance Spectra (UV- vis DRS)

UV-vis DRS was performed to study the enhancement of light absorption properties and the changes in band gap energy after conjugation of CDs into the $g\text{-C}_3\text{N}_4$. As illustrated in Figure 4.6, the pure $g\text{-C}_3\text{N}_4$ showed an intrinsic absorption edge at around 430 nm. The absorption peaks in the range between 260 nm to 340 nm was due to the $\pi\text{-}\pi^*$ transition of the sp^2 conjugated aromatic s-heptazine units and the $n\text{-}\pi^*$ electronic transition of the C=O bonds (Wang et al., 2017e). In comparison, the CDs/ $g\text{-C}_3\text{N}_4$ composites showed higher absorption intensity over the whole spectrum from 200 nm to near 800 nm. The intensity of the absorption peak was increased with the CDs loading in the CDs/ $g\text{-C}_3\text{N}_4$. Moreover, the CDs/ $g\text{-C}_3\text{N}_4$ also exhibited a red shift of the absorption edge and an additional shoulder peak (broad band) from

430 nm to 800 nm. The shoulder peak was mainly attributed to the light absorption of CDs and the red shift of the absorption edge was due to the interfacial interaction between CDs and g-C₃N₄ (Wang et al., 2017d). The UV-vis DRS results of the CDs/g-C₃N₄ composites showed broadened of the absorption band until the near infrared region with significant absorption in the visible light region. The hypochromic shift of the band gap was attributed to the quantum confinement effect of the incorporated CDs which possess excellent photosensitising properties (Wong, 2017). The absorption area in the range of 350 nm to 500 nm represents the π - π^* electron transition. The transitions include bonding (σ and π), nonbonding (n) and antibonding (σ^* and π^*) orbitals. The π - π^* and n - π^* transition energies corresponded to the wavelength of the visible light (Fadllan et al., 2017). The broader range of the light absorption spectrum can enhance the photocatalytic performance of the photocatalyst under solar irradiation by generating more electron-hole pairs which are necessary for the formation of the ROS. In short, the incorporation of CDs into the pure g-C₃N₄ can increase the absorption intensity and broaden the absorption wavelength of the photocatalyst thus improve the photocatalytic reaction.

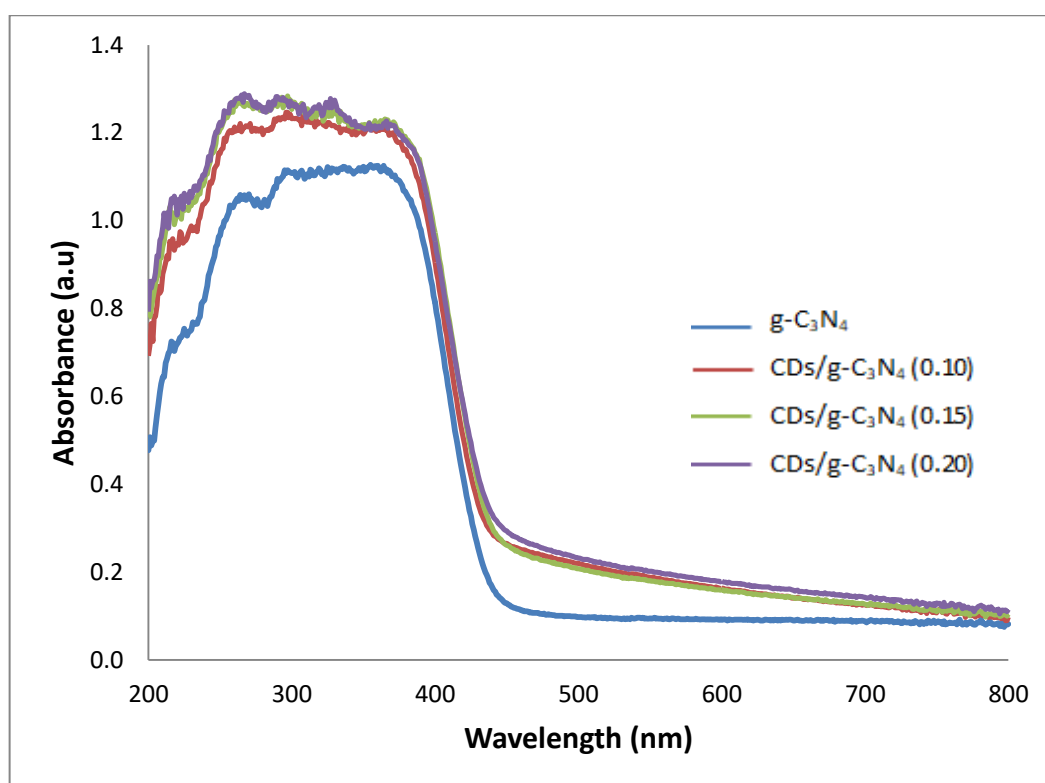


Figure 4.6: UV-vis DRS Absorption Spectra of g-C₃N₄ and CDs/g-C₃N₄ Composites

In addition, the band gap energy is determined according to the Tauc plot of $(F(R)*hv)^{1/2}$ against the photon energy, hv as illustrated in Figure 4.7. The value of $F(R)$ was obtained by using the Kubelka-Munk function as shown from Equation 4.1 to 4.3 as below:

$$F(R) = (1 - R)^2/2R \quad (4.1)$$

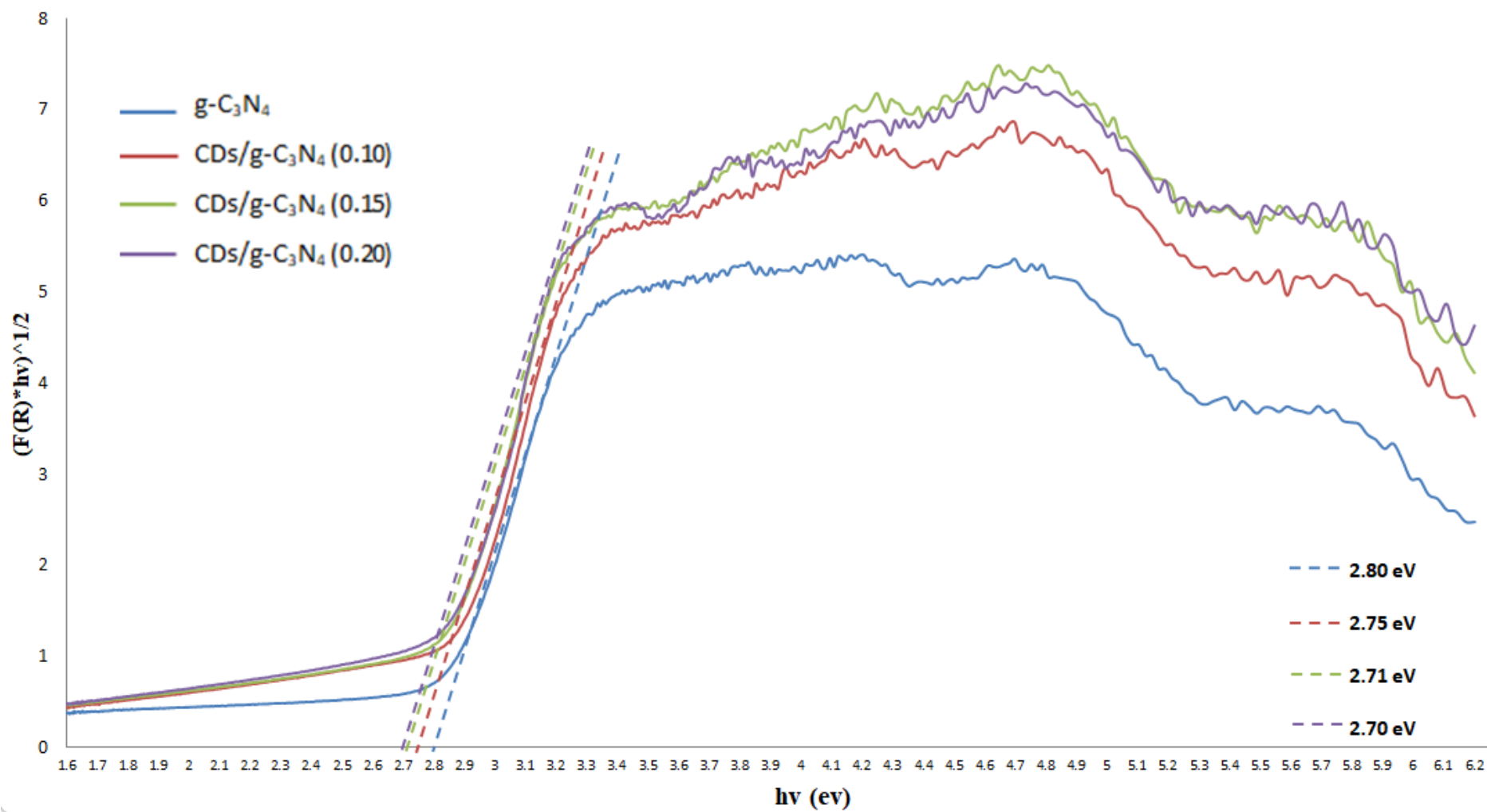
$$R = \%R/100 \quad (4.2)$$

$$hv = 1240/\lambda \quad (4.3)$$

where R is the intensity of diffuse reflectance while λ is the wavelength (Tai et al., 2018). The band gap energies of the CDs/g-C₃N₄ composites were determined by the interception between the tangent line to the x-axis. The band gap energies are shown in Table 4.3 and it was observed that the band gap energy reduced with the CDs weight percent in the composites. Reduction in the band gap energy implied better photocatalytic performance as the energy required to initiate the redox reaction was reduced. In short, based on the UV-DRS results, the light harvesting capability of the synthesized photocatalysts were arranged in the sequence of CDs/g-C₃N₄ (0.20) > CDs/g-C₃N₄ (0.15) > CDs/g-C₃N₄ (0.10) > g-C₃N₄.

Table 4.3: Summary of Band Gap Energy of Photocatalysts

Photocatalyst	Band gap (eV)
g-C ₃ N ₄ .	2.80
CDs/g-C ₃ N ₄ (0.10)	2.75
CDs/g-C ₃ N ₄ (0.15)	2.71
CDs/g-C ₃ N ₄ (0.20)	2.70

Figure 4.7: Tauc Plot of $g-C_3N_4$ and $CDs/g-C_3N_4$ Composites

4.1.5 X-ray Diffraction (XRD)

Figure 4.8 shows the XRD spectra of the pure g-C₃N₄ and the CDs/g-C₃N₄ composites. The detail XRD report is attached in Appendix F. It was interested whether the phase structures of the g-C₃N₄ nanosheets will be altered after incorporation with CDs. According to the XRD pattern of g-C₃N₄, two characteristic peaks at 27.129 ° and 12.900 ° are observed. The strong peak at 27.129 ° can be indexed to (002) planes with an interplanar distance of around 0.328 nm, corresponding to the graphite-like periodic repeated stacking of conjugated aromatic units. Furthermore, the minor peak at 12.9 ° can be indexed to (100) facet of g-C₃N₄ with the interplanar distance of around 0.686 nm which represented the in-plane structural packing motif of the tri-s-triazine units (Wang et al., 2017c). Other non-characteristic peaks at 77.7316 ° and 64.5532 ° might due to the presence of impurities during the preparation of the g-C₃N₄. The CDs/g-C₃N₄ composites showed similar XRD patterns as the pure the g-C₃N₄. However, the peaks positions were slightly shifted from 27.129 ° to 27.36 °; 27.38 ° and 27.40 ° as the weight percent of CDs increased. The shifting of the peak's position elucidated the successful conjugation of CDs into the g-C₃N₄ (Mewada et al., 2013). Moreover, the intensity of the peaks at 27 ° decreased after the introduction of CDs into g-C₃N₄ as shown in Table 4.4. This was due to the presence of CDs had prevented the polymerization of dicyandiamide as well as the crystallization of g-C₃N₄ (Fang et al., 2015). Moreover, the peak at 12.9 ° was disappeared for the composites which possibly due to strong interfacial interaction between the CDs and g-C₃N₄ that disturbed the periodic potential field of the heptazine (Wang et al., 2017d). Instead, minor peaks occurred at 25.5400 °; 25.000 ° and 25.0800 ° for CDs/g-C₃N₄ (0.10), CDs/g-C₃N₄ (0.15) and CDs/g-C₃N₄ (0.20) respectively. The peaks were attributed to the low-mass CDs in the nanoheterostructure (Lv et al., 2017). In overall, the doping of CDs into the g-C₃N₄ did not destroy the structure of g-C₃N₄ since the XRD patterns of the composites were similar to the one of pure g-C₃N₄.

Table 4.4: Intensities of Diffraction Peaks at 2θ of 27.×× °

Photocatalysts	Diffraction Peak (°)	Intensity
g-C ₃ N ₄	27.129	672
CDs/ g-C ₃ N ₄ (0.10)	27.360	432

Table 4.4 (Continued)

CDs/ g-C ₃ N ₄ (0.15)	27.380	389
CDs/ g-C ₃ N ₄ (0.20)	27.400	254

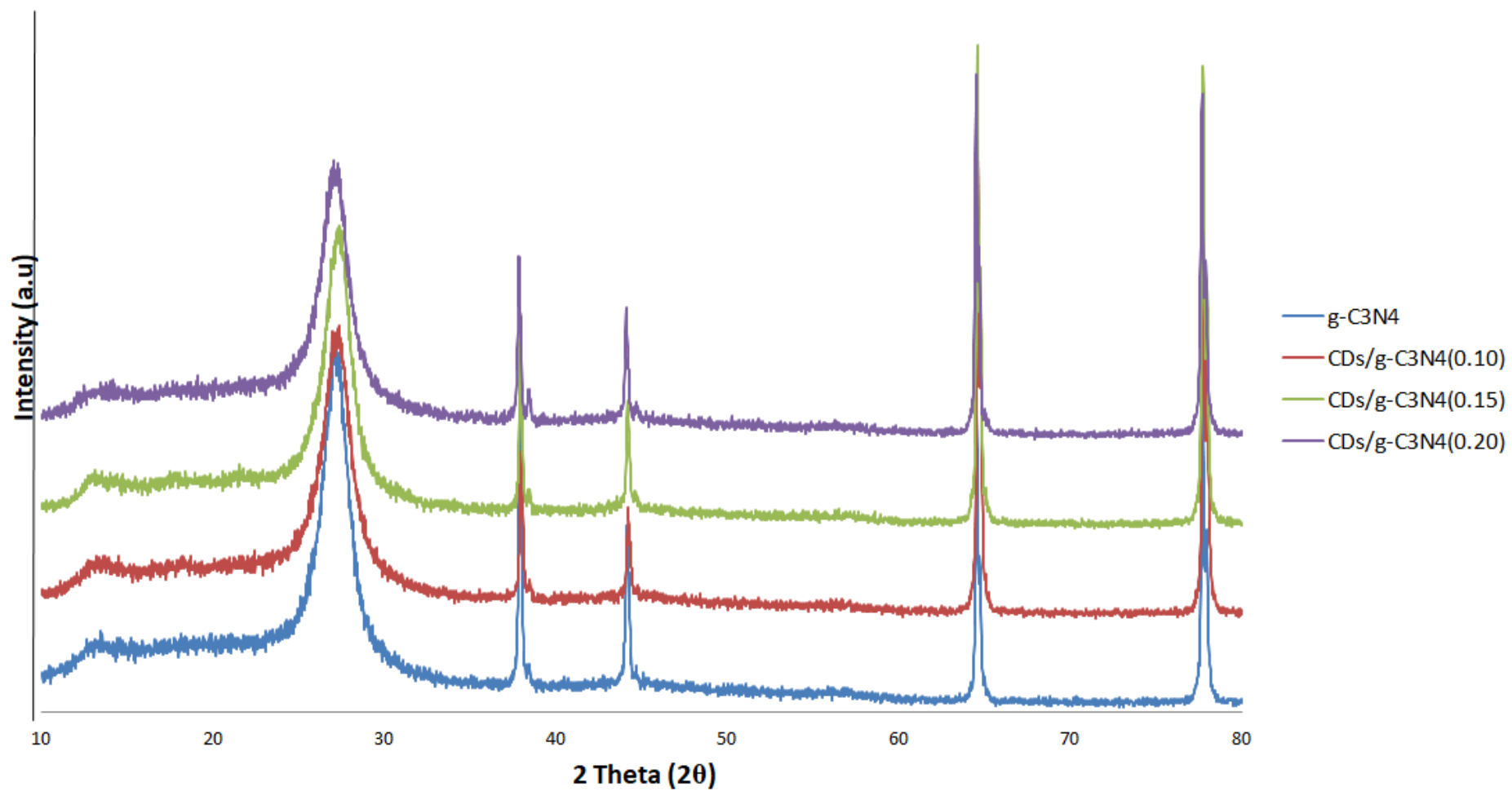
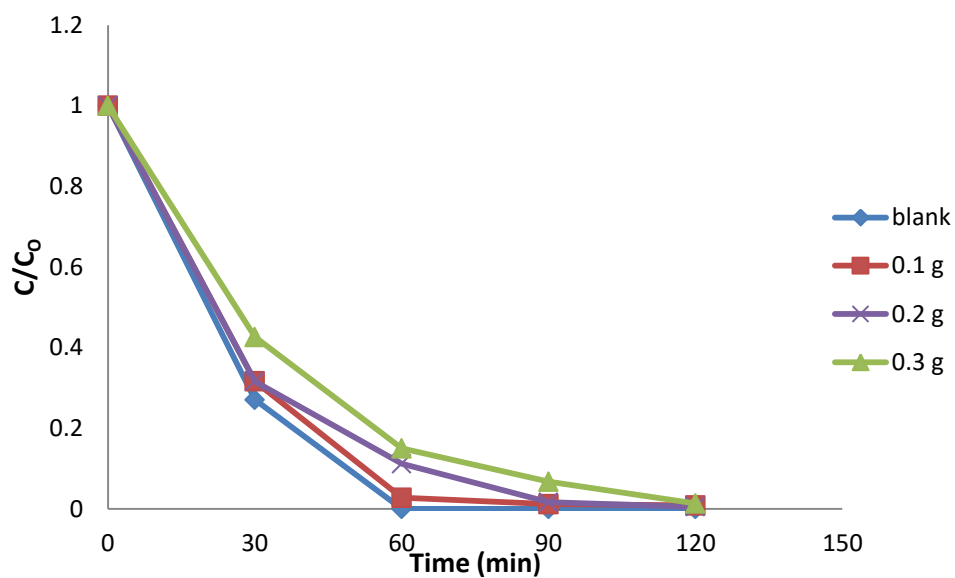


Figure 4.8: XRD Spectra of g-C₃N₄ and CDs/g-C₃N₄ Composites

4.2 Antibacterial Application of CDs under Solar Irradiation

Figure 4.9 and Table 4.5 show the inactivation rate of *E.coli* by the prepared CDs. Besides, Tables 4.6 to 4.9 demonstrate the number of viable *E.coli* in agar plates at different time intervals and CDs concentrations.

Based on the result obtained, the number of viable *E.coli* was reduced with the time which elucidated the *E.coli* in the solution were being killed as time passed by. In the proposed disinfection mechanism by the CDs, the *E.coli* was inactivated by the ROS generated. The ROS could cause lethal attack to the bacterial cell and damage the cell membrane which further lead to leach of intracellular components and dead of the cell (Huang et al., 2015). According to the result obtained, the rate of inactivation of *E.coli* was arranged in the order of blank > CDs (0.1 g) > CDs (0.2 g) > CDs (0.3 g). The results indicated that sunlight itself was efficient enough in killing the *E.coli* since the blank sample (without CDs) presented the best bactericidal performance among the samples prepared. According to study conducted by Vermeulen et al. (2008), wavelengths in the UV region, especially at 256 nm possess the bactericidal ability and the number of viable *E.coli* cells decreased exponentially with the radiation dosage. On the other hand, as photosensitizer, CDs have a broad light harvesting spectra in the UV-vis range and the photons absorbed will be used to generate the ROS for the photocatalytic disinfection. According to the result shown in Figure 4.9, the rate of disinfection of *E.coli* in the blank sample was better than CDs added samples. This might due to the poor solubility of CDs in aqueous solution which cloud impeded the photocatalytic disinfection performance. Besides, since both direct UV-vis irradiation and ROS produced by CDs took part in the inactivation of *E.coli*, both were competing for the photons. The higher rate of disinfection of blank sample over CDs-added samples might due to more photons were available for the inactivation of *E.coli* by direct UV-vis irradiation since no CDs competed for the energy. Therefore, it was suggested that the inactivation rate of *E.coli* induced by direct UV-vis irradiation was dominant in this case.

Figure 4.9: *E. coli* Inactivation RateTable 4.5: Inactivation Rate of *E. coli*

Sample	Inactivation Rate (%)
Blank	100
0.1 g CDs	99.02
0.2 g CDs	98.76
0.3 g CDs	97.84

Table 4.6: Viable *E. coli* after 30 min

Dilution	10^{-2}	10^{-3}	10^{-4}
Samples			
Blank			
CDs (0.1 g)			

Table 4.6 (Continued)

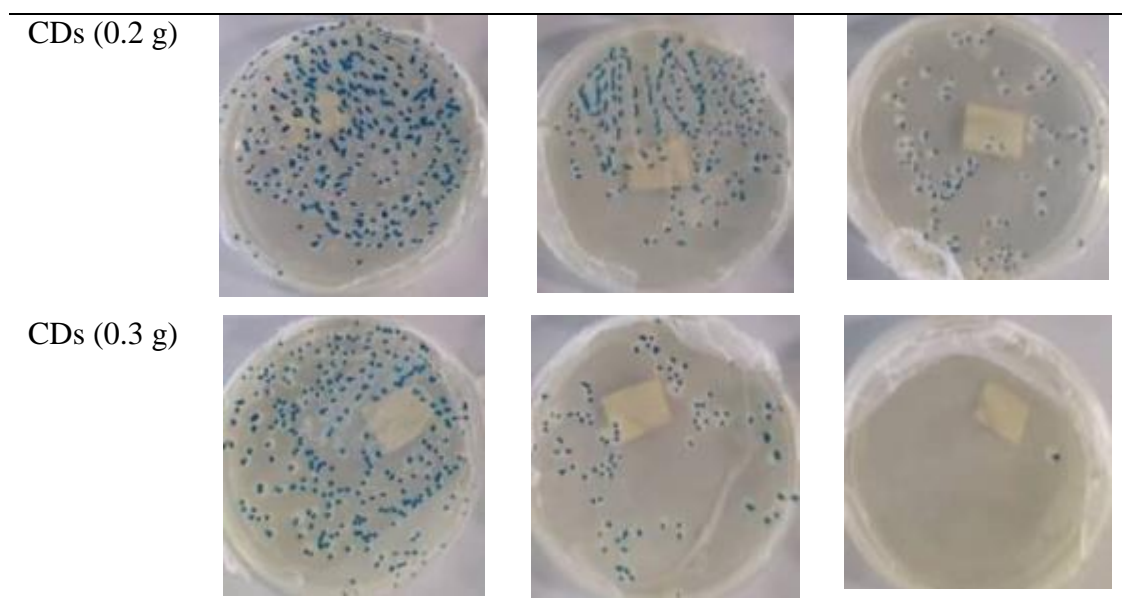
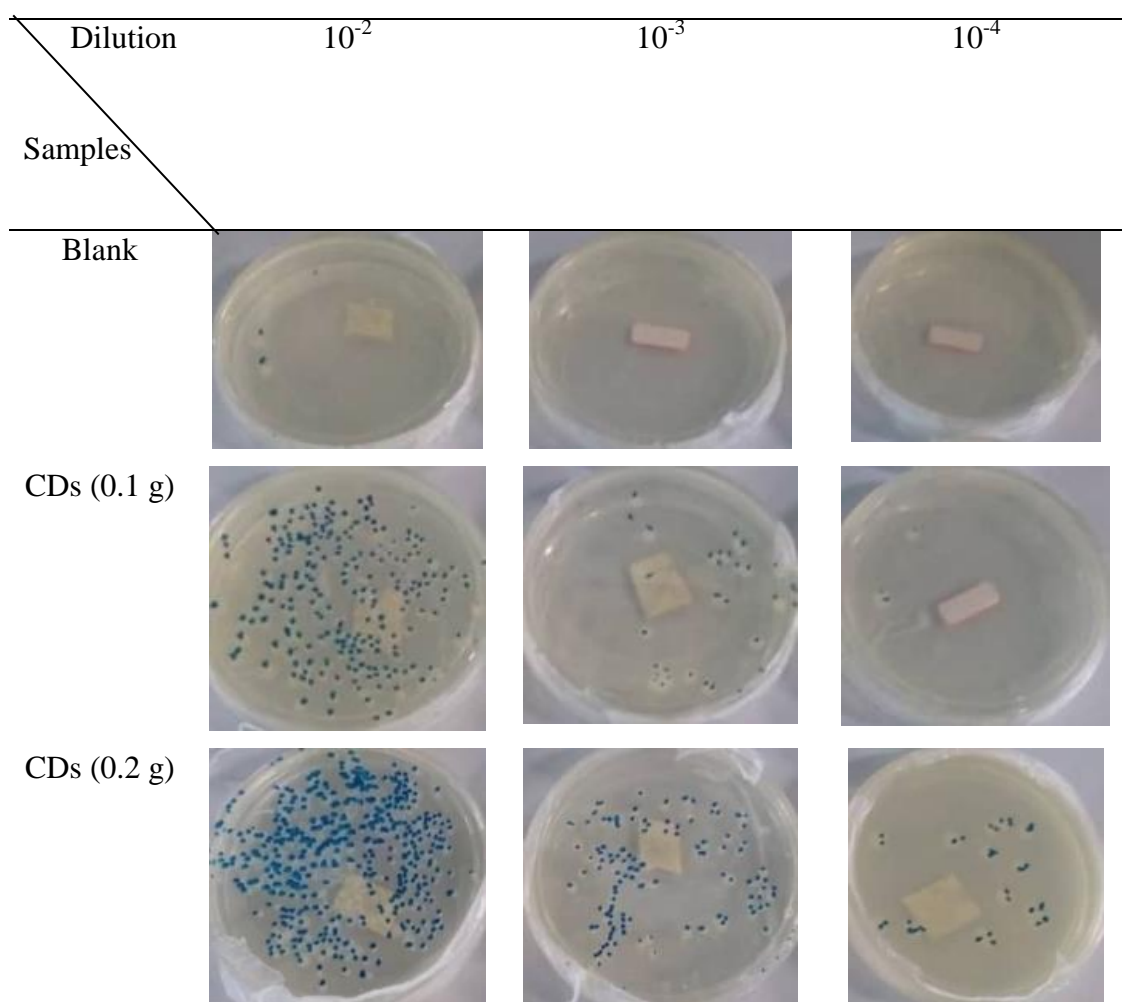
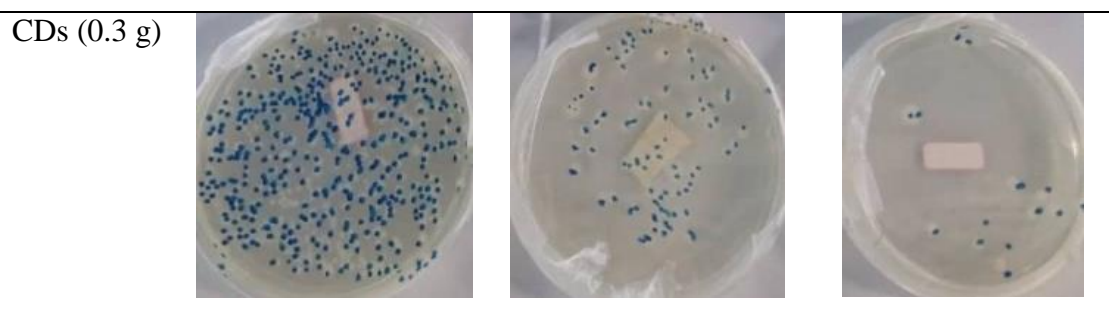
Table 4.7: Viable *E.coli* after 60 min

Table 4.7 (Continued)

Table 4.8: Viable *E.coli* after 90 min

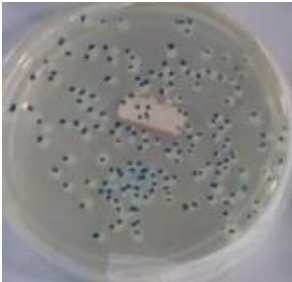
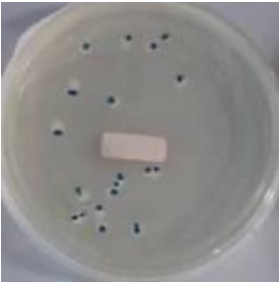
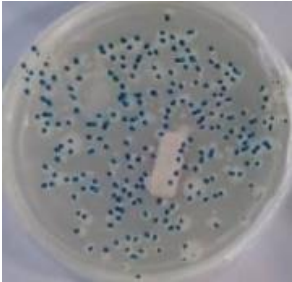
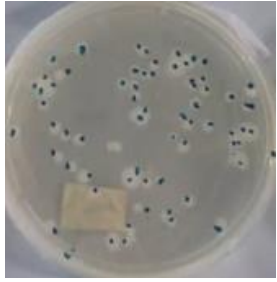
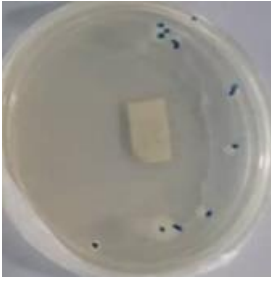
Dilution	10^{-2}	10^{-3}	10^{-4}
Blank			
CDs (0.1 g)			
CDs (0.2 g)			

Table 4.8 (Continued)

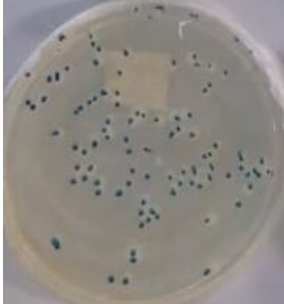
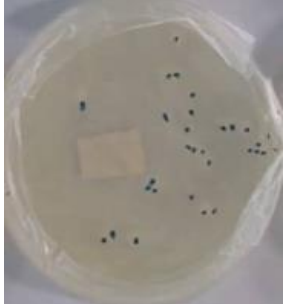
CDs (0.3 g)			
-------------	---	--	---

Table 4.9: Viable *E.coli* after 120 min

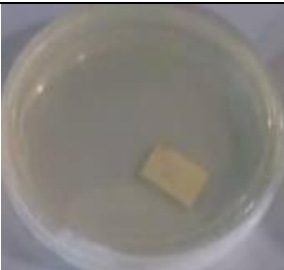
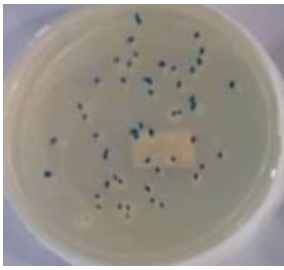
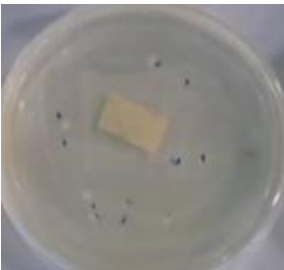
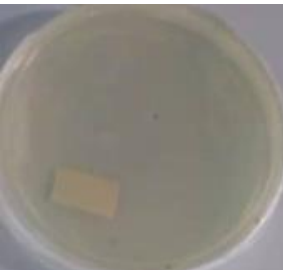
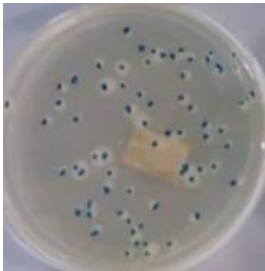
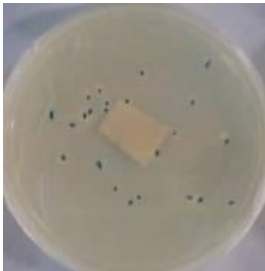
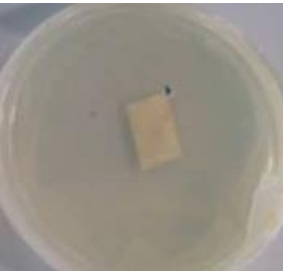
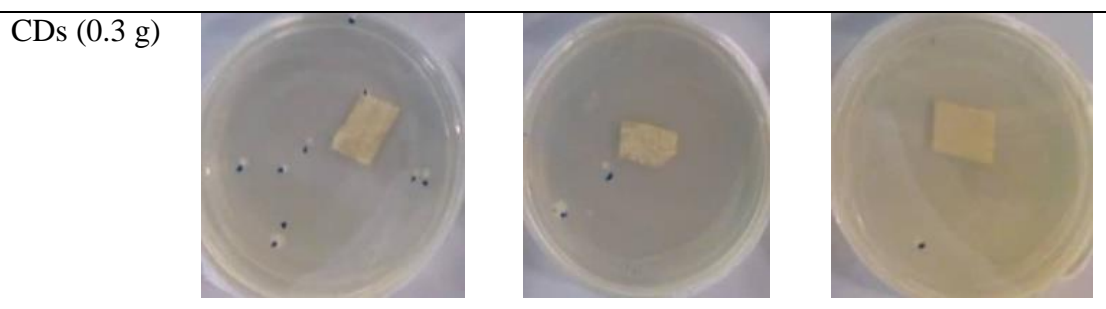
Dilution	10^{-2}	10^{-3}	10^{-4}
Blank			
CDs (0.1 g)			
CDs (0.2 g)			

Table 4.9 (Continued)



4.3 Application of CDs/g-C₃N₄ Composites in BPA Degradation under Solar Irradiation

The photodegradation performances of photocatalysts prepared are illustrated in Figure 4.10. The degradation rates of BPA were calculated based on Equation 4.4.

$$\text{Photodegradation rate} = \left[\frac{(C_0 - C)}{C_0} \right] \times 100 \% \quad (4.4)$$

where C_0 and C represent the initial and final concentrations of BPA respectively. Besides, the reaction kinetics of BPA degradation can be related to the pseudo-first-order reaction kinetics as shown in Equation 4.5.

$$\ln \left(\frac{C}{C_0} \right) = -kt \quad (4.5)$$

where k (min^{-1}) is the rate constant of first-order reaction, C_0 is the initial BPA concentration while C refers to the concentrations of BPA at time t (min). A line graph with the gradient represents the k values of the photocatalysts is shown in Figure 4.11. Besides, Figure 4.12 compares the k values of synthesised photocatalysts. The degradation rates and k values are tabulated in Table 4.10.

Table 4.10: Photodegradation Rate and k Values of CDs/g-C₃N₄ Composites

Sample	Photodegradation rate (%)	k (min^{-1})
Blank	0.00	0.00005
g-C ₃ N ₄	56.70	0.00230
CDs/g-C ₃ N ₄ (0.10)	76.97	0.00400
CDs/g-C ₃ N ₄ (0.15)	81.82	0.00470

Table 4.10 (Continued)

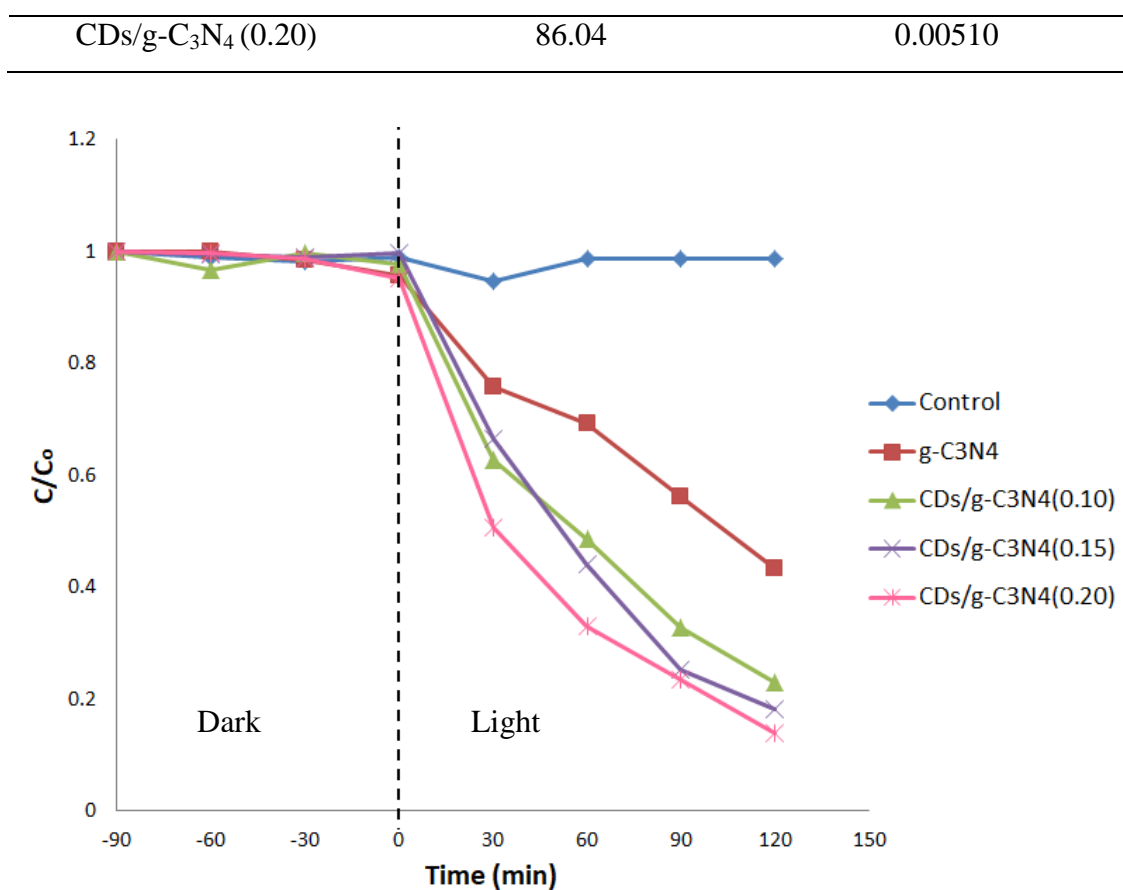


Figure 4.10: Photodegradation Rate of BPA by Photocatalysts

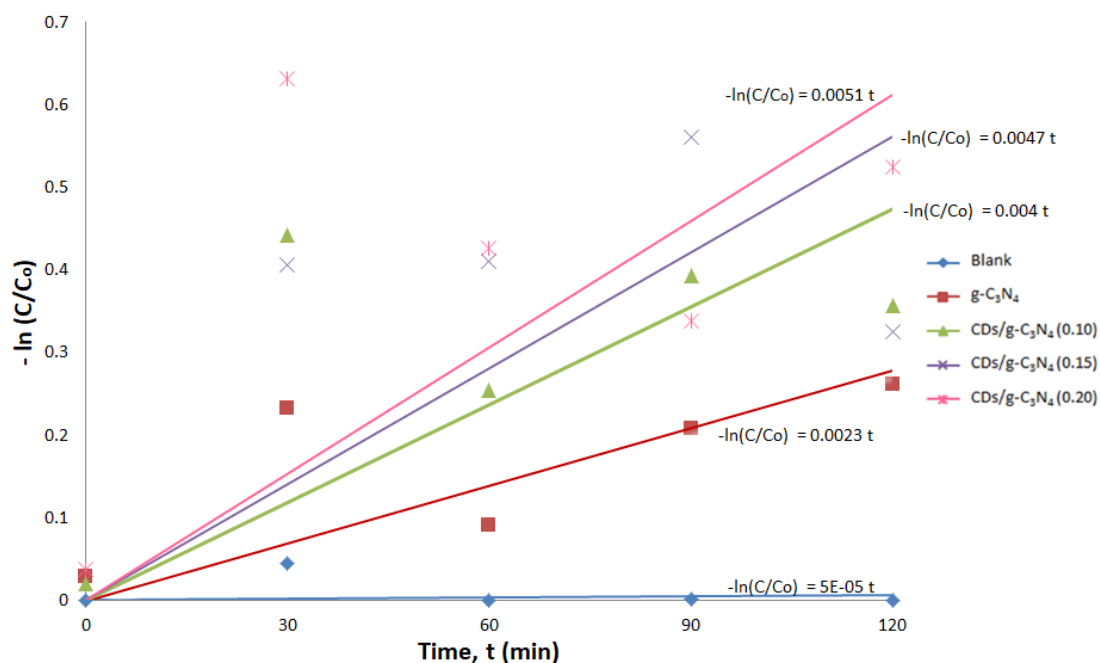


Figure 4.11: First-order Kinetic Plots of BPA Photodegradation by Photocatalysts

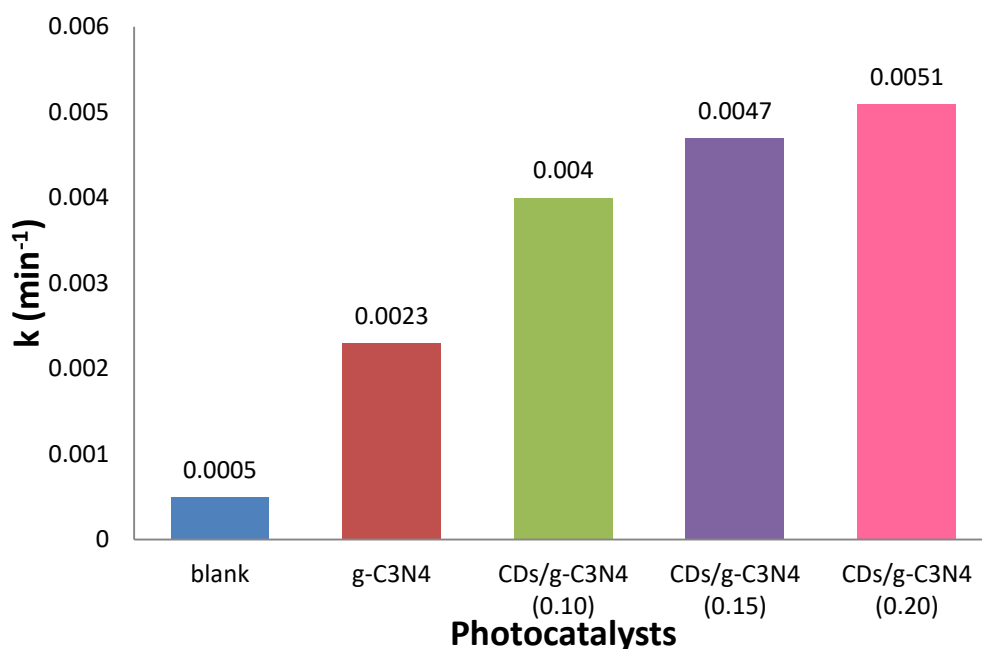


Figure 4.12: First-order Reaction Rate Constants of Photocatalysts

Based on result shown in Figure 4.10, no obvious BPA degradation was observed in the dark, which implied photons from sunlight were necessary to initiate the photocatalysis. Besides, the blank sample without CDs/g-C₃N₄ exhibited a stable C_0/C ratio which indicated there was almost no degradation of BPA throughout the experiment. The trend clarified that BPA had poor photolysis properties and was hardly degraded without the aid of photocatalyst. The photodegradation rate of BPA by the composites was ranged as CDs/g-C₃N₄ (0.20) > CDs/g-C₃N₄ (0.15) > CDs/g-C₃N₄ (0.10) > g-C₃N₄ as shown in Table 4.10. The trend was further supported by the first-order kinetic rate constant where the rate constant increased with the weight percentage of CDs in the composites.

The results indicated that incorporating CDs into g-C₃N₄ would enhance the photodegradation performance of pure g-C₃N₄ and the photodegradation rate increased with the concentration of the CDs in the composites. The significant increment of the photodegradation rate after doping of CDs into the pure g-C₃N₄ was due to enhanced quantum efficiency and light harvesting properties of the photocatalysts. The results were correlated well with the UV-vis DRS analysis which proven that increase in CDs loading can widen the solar-absorption spectra, increase light absorption intensity and reduce the band gap energy of the composites. Besides, the CDs also aided in the separation of the electrons-holes pairs which further

improved the photodegradation of BPA. However, it was observed that the photodegradation rate only increased slightly (around 5 %) from CDs/g-C₃N₄ (0.15) to CDs/g-C₃N₄ (0.20). This phenomenon was due to the shielding effect of carbon which masked the active sites and reduced the light absorption ability of the photocatalysts (Zhang, et al., 2016).

4.4 Scavengers Test

Scavenger test was conducted in order to identify the types of active species that took part in the photodegradation of BPA and their order of influence. The scavengers used in the test include benzoquinone (BQ), ethylenediamine-tetraacetic acid disodium salt (EDTA-2Na⁺), isopropyl alcohol (IPA) and dimethyl sulfoxide (DMSO). BQ was responsible to capture the superoxide radicals ($\cdot\text{O}_2^-$) in the solution and thus impeded the degradation of BPA by $\cdot\text{O}_2^-$. Besides, EDTA and DMSO were used to trap the holes (h^+) and electron (e^-) respectively and thus obstructed the following redox reactions for ROS formation. In addition, IPA acted as hydroxyl radicals ($\cdot\text{OH}$) catcher in the BPA solution which prohibited any degradation of BPA by $\cdot\text{OH}$.

The photodegradation of BPA as a function of time, kinetic plot and the k values of the photocatalysts are shown in Figure 4.13, Figure 4.14 and Figure 4.15 respectively. Besides, Table 4.11 tabulates the photodegradation rate and the k values of the photocatalysts. The rate of photodegradation is arranged in the order of blank (no scavenger) > DMSO > IPA > EDTA > BQ. The result was further supported by the k values. Therefore, the influence of the active radical species in the photodegradation rate of BPA was in the order of $\cdot\text{O}_2^- > \text{h}^+ > \cdot\text{OH} > \text{e}^-$. The blank sample (without addition of scavenger) showed the best photodegradation performance since no free radicals were being captured and the reactions could proceed continuously until BPA was being degraded. On the other hand, there was no significant BPA degradation in BQ-added solution, which indicated $\cdot\text{O}_2^-$ was the most important oxidising radicals for the photodegradation of BPA. Furthermore, the BPA degradation was suppressed with the addition of EDTA which implied h^+ played a significant role in the reaction. As shown in Equation 2.11 previously, h^+ was directly involved in the degradation of pollutant, thus absent of h^+ in the solution resulted in reduced degradation rate of BPA. Moreover, since h^+ involve in the direct

formation of hydroxyl radicals ($\cdot\text{OH}$) and the indirect formation of hydroperoxyl radicals ($\cdot\text{HO}_2$) and superoxide radicals ($\cdot\text{O}_2^-$), absent of h^+ caused less amount of free radicals being generated for the degradation process. In addition, IPA and EDTA-added samples showed similar effects on BPA degradation performance. In IPA-added solution, $\cdot\text{OH}$, which was one of the major free radicals for BPA degradation is absent in the solution. Therefore, the rate of degradation is reduced. Besides, e^- involved in the formation of $\cdot\text{O}_2^-$, $\cdot\text{OH}$ and $\cdot\text{HO}_2$, thus the number of free radicals for the degradation process was diminished.

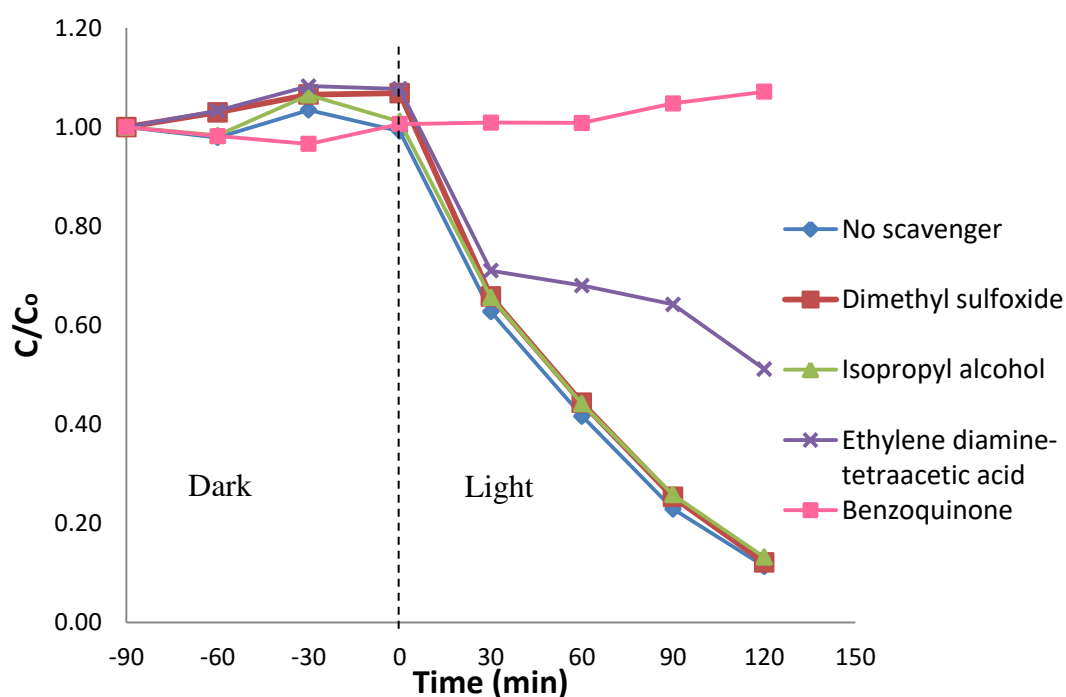


Figure 4.13: Photodegradation Rate of BPA for Scavengers Test

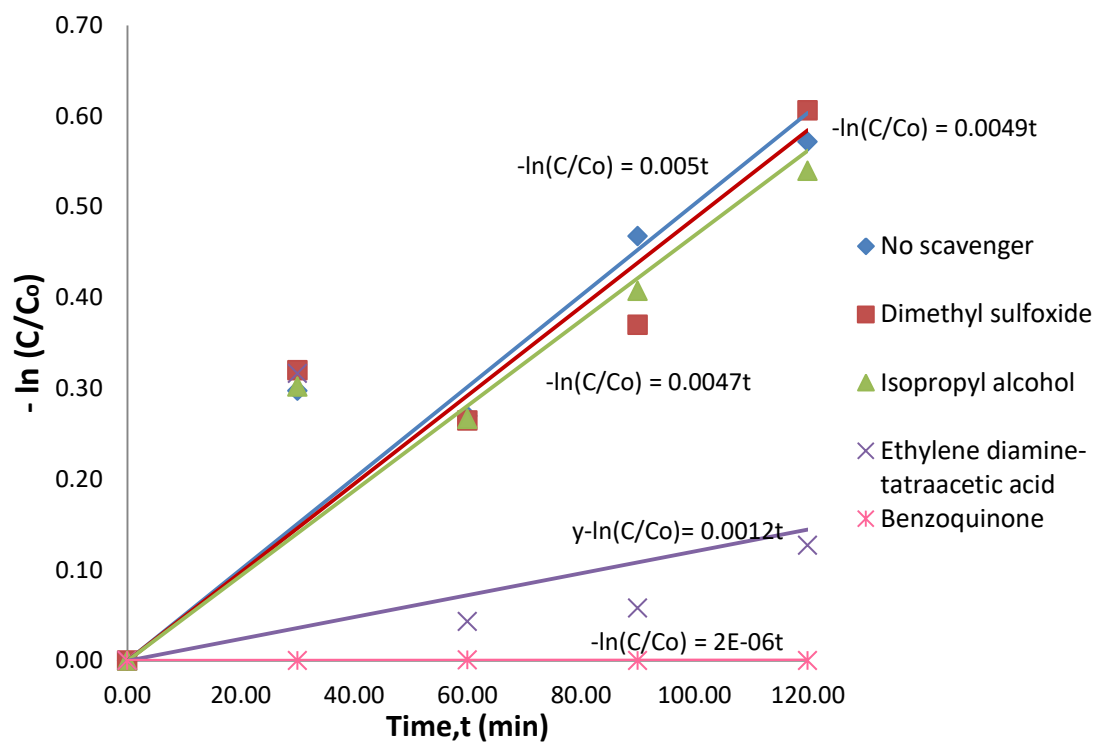


Figure 4.14: First-order Kinetic Plots of BPA Photodegradation for Scavengers Test

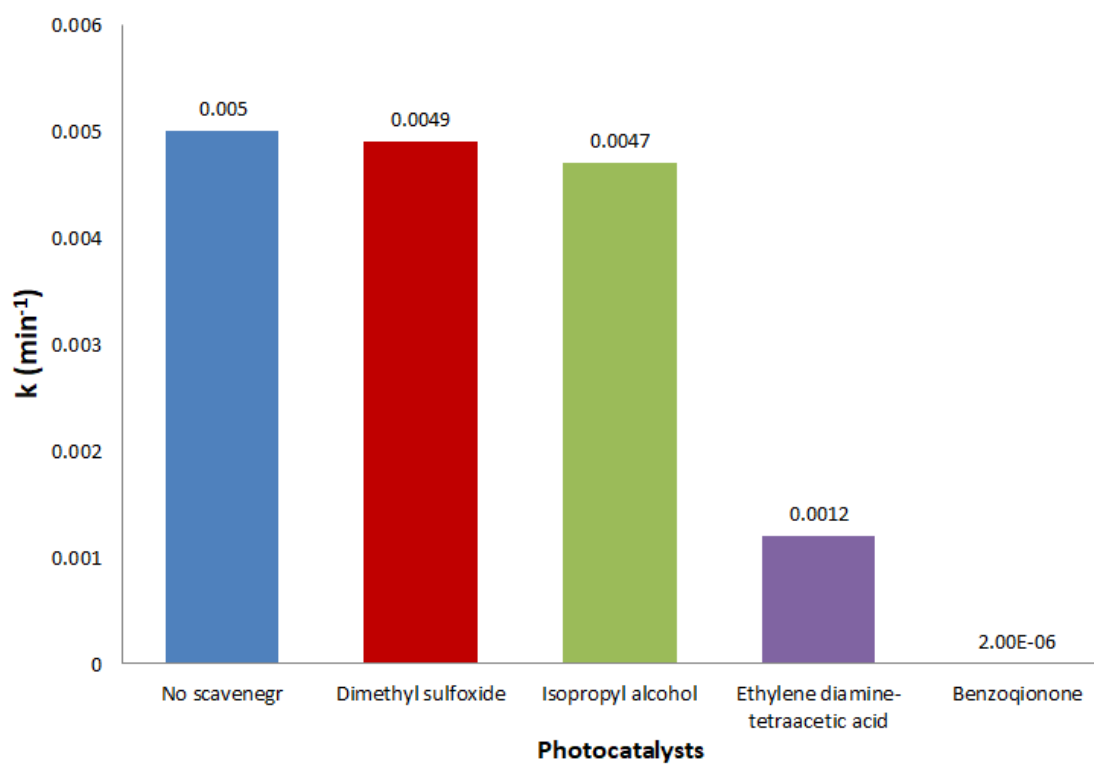


Figure 4.15: First-order Reaction Rate Constants of Photocatalysts for Scavenger Test

Table 4.11: Photodegradation Rate of BPA by CDs/g-C₃N₄ Composites

Sample	Photodegradation rate (%)	k (min ⁻¹)
No scavenger	0.00	0.0050
DMSO	56.70	0.0049
IPA	76.97	0.0047
EDTA	81.82	0.0012
BQ	86.04	2×10 ⁻⁶

4.5 Costing and Sustainability

The cost of synthesising CDs, g-C₃N₄ and CDs/g-C₃N₄ photocatalysts for one batch of experiment were calculated in order to investigate the economic feasibility for the generation of photocatalysts. The required amount for CDs for one batch of experiment was around 1 g while the amount of g-C₃N₄ and CDs/g-C₃N₄ were 4 g and 0.3 g respectively. The electricity bill was calculated based on Equation 4.5 according to the Tariff B (Low Voltage Commercial Tariff, RM 0.453/kWh) of the commercial electricity usage supplied by Tenaga Nasional Berhad (TNB). The total energy consumed and the material cost for one batch of experiment are listed in Table 4.10 and Table 4.11 respectively.

$$\text{Electricity bill (RM)} = \text{RM } 0.435/\text{kWh} \times \text{Consumption (kWh)} \quad (4.5)$$

Table 4.12: Energy Consumption for Preparation of CDs and CDs/g-C₃N₄

Equipment	Power (watt)	Duration (h)	Consumption (kWh)
(a) CDs			
Oven	1800.00	12.00	21.60
Centrifuge	455.00	0.75	0.34
Freeze Dryer	350.00	72.00	25.20
(b) g-C ₃ N ₄			
Furnace	1800.00	15.00	27.00

Table 4.12 (Continued)

(c) CDs/g-C ₃ N ₄			
Oven	1800.00	5.00	9.00
Centrifuge	455.00	0.75	0.34
Total Consumption (kWh)			83.48

Table 4.13: Material used for Preparation of CDs and CDs/g-C₃N₄

Materials	Price (RM)	Usage (g)	Cost (RM)
Urea (500 g)	16.00	100	3.20
Total Cost			3.20

$$\text{Total production cost} = \text{RM } 84.38 + \text{RM } 3.20 = \text{RM } 87.58$$

The total cost required to synthesise the photocatalysts was approximately RM 88.00 with about 96 % of the cost was attributed to electricity consumption. The cost of raw materials was relatively cheap since the waste papaya peels were collected from the fruit hawker. Beside, hydrothermal treatment adopted for the preparation of CDs is a green and environmental-friendly method since no harmful by-product generated.

In term of sustainability of the research, CDs synthesised from waste papaya peels was considered as a sustainable and green resource with high availability. Besides, for the light source, the harmful and electricity-intensive UV light was substituted with sustainable natural solar irradiation.

CHAPTER 5

CONCLUSION AND RECOMMENDATIONS

5.1 Conclusion

CDs with waste papaya peels as precursor were successfully synthesised through hydrothermal treatment. However, the CDs did not show evidently effect in inactivation of *E.coli*. This was possibly due to high solubility of CDs in aqueous solution which impede its performance and the compromising effect of competing the photons with UV-driven *E.coli* inactivation. In addition, CDs/g-C₃N₄ photocatalysts with CDs weight percentage of 10 wt.% , 15 wt.% and 20 wt.% were prepared. The FTIR characterisation proved the success incorporation of CDs onto the g-C₃N₄. Besides, the SEM showed the wrinkled structure of g-C₃N₄ offered a great support for the attachment of CDs. CDs/g-C₃N₄ with higher CDs content displayed more aggregated and packed morphological structure. The EDX also elucidated that the composites were comprised of nitrogen (N), carbon (C), and small amount of oxygen (O). Besides, the atomic percentages of CDs/g-C₃N₄ photocatalysts were higher than pure g-C₃N₄. The UV-vis DRS analysis indicated that the composites owned wider absorption spectrum than that of pure g-C₃N₄ by shifting the light absorption range of the photocatalyst towards the visible and NIR region. Moreover, the overall light absorption intensity of CDs/g-C₃N₄ was increased with the weight percentage of CDs. The band gap of the photoactalysts also reduced with the loading of CDs in the composites. As a result, the light harvesting ability of the photocatalysts were arranged in the sequence of CDs/g-C₃N₄ (0.20) > CDs/g-C₃N₄ (0.15) > CDs/g-C₃N₄ (0.10) > g-C₃N₄. In addition, the PL properties of CDs rendered it as photosensitizer to improve BPA photodegradation rate. In term of the BPA photodegradation performance, CDs/g-C₃N₄ showed better degradation rate than pure g-C₃N₄. Besides, the experimental results also revealed that BPA removal efficiency was improved by increasing the CDs concentration in the composites with the sequence of CDs/g-C₃N₄ (0.20) > CDs/g-C₃N₄ (0.15) > CDs/g-C₃N₄ (0.10) > g-C₃N₄. The highest absorption intensity of the CDs/g-C₃N₄ (0.20) over the entire solar spectrum and its lowest band gap energy rendered it the best performance in photocatalytic degradation of BPA. Furthermore, superoxide radical ($\cdot\text{O}_2^-$) and holes

(h^+) were identified as the major active species in the photodegradation. This study was considered practicable and economical because the CDs/g-C₃N₄ composites were synthesised from waste papaya peels instead of edible materials or harmful chemical. The positive results of BPA photodegradation also suggested CDs dopped g-C₃N₄ was a compromising photocatalyst for heterogeneous photocatalysis under sunlight irradiation. Lastly, the prepared composites rendered a sustainable and environmental friendly method for the pollutant treatment.

5.2 Recommendations for Future Work

Several improvements related to the research work can be considered to ameliorate the precision and reliability of the experimental results in order to ease the future work. The recommendations are listed below:

- I. It is encouraged to carry out X-ray photoelectron spectroscopy (XPS) and high-resolution transmission electron microscopy (HRTEM) analysis to study the ionic characteristic and the lattice structure of the prepared photocatalysts. Besides, it is also recommended to determine the quantum yield (QY) of CDs to identify the amount of photon energy produced.
- II. It is preferable to conduct the PL analysis for the CDs/g-C₃N₄ composite as well in order to investigate the charge separation efficiency which is another important parameter that affecting the photocatalytic performance of the photocatalyst.
- III. The antibacterial experiment of CDs is suggested to carry out under visible light range instead of sunlight.
- IV. Other experimental parameters such as pH of the solution and light intensity can be studied.
- V. CDs dopped with different materials such as nitrogen and chlorine can be synthesised to enhance the fluorescence properties of the composites.

REFERENCE

- Aljundi, I.H., 2011. Bromate formation during ozonation of drinking water: A response surface methodology study. *Desalination*, 277(1–3), pp.24–28.
- Ameta, R., Solanki, M.S., Benjamin, S. and Ameta, S.C., 2018. Photocatalysis. In: *Advanced Oxidation Processes for Waste Water Treatment*, pp.135–175.
- Balabanič, D., Hermosilla, D., Merayo, N., Klemenčič, A.K. and Blanco, Á., 2012. Comparison of different wastewater treatments for removal of selected endocrine-disruptors from paper mill wastewaters. *Journal of Environmental Science and Health - Part A Toxic/Hazardous Substances and Environmental Engineering*, 47(10), pp.1350–1363.
- Bergman, Å., Heindel, J., Jobling, S., Kidd, K. and Zoeller, R.T., 2012. *State of the science of endocrine disrupting chemicals, 2012. Toxicology Letters*.Switzerland: WHO
- Brussels, 2007. *Comission Staff Working Document on the implementation of the "Community Strategy for Endocrine Disrupters"-a range of substances suspected of interfering with the hormone systems of humans and wildlife*.Geneva: Commission of the European Communities
- Buckle, J., 2015. Infection. In: *Clinical Aromatherapy*. 3rd ed. London:Churchill Livingstone
- Cao, L., Wang, X., Mezziani, M.J., Lu, F., Wang, H., Luo, P.G., Lin, Y., Harruff, B.A., Veca, L.M., Murray, D., Xie, S.-Y. and Sun, Y.-P., 2007. Carbon Dots for Multiphoton Bioimaging. *Journal of the American Chemical Society*, 129(37), pp.11318–11319.
- Carr é G., Hamon, E., Ennahar, S., Estner, M., Lett, M.-C., Horvatovich, P., Gies, J.-P., Keller, V., Keller, N. and Andre, P., 2014. TiO₂ photocatalysis damages lipids and proteins in Escherichia coli. *Applied and environmental microbiology*, 80(8), pp.2573–2581.
- Chemistry LibreTexts, 2009. *Infrared Spectroscopy Absorption Table* - [online] Available at: <https://chem.libretexts.org/Ancillary_Materials/Reference/Reference_Tables/Spectroscopic_Parameters/Infrared_Spectroscopy_Absorption_Table> [Accessed 4 Mar. 2019].
- Chen, J., Shu, J., Anqi, Z., Juyuan, H., Yan, Z. and Chen, J., 2016a. Synthesis of carbon quantum dots/TiO₂nanocomposite for photo-degradation of Rhodamine B and cefradine. *Diamond and Related Materials*, 70, pp.137–144.
- Chen, Y., Lu, Q., Yan, X., Mo, Q., Chen, Y., Liu, B., Teng, L., Xiao, W., Ge, L. and Wang, Q., 2016b. Enhanced Photocatalytic Activity of the Carbon Quantum Dot-Modified BiOI Microsphere. *Nanoscale Research Letters*, 11(1), pp.1–7.

Choi, Y., Choi, Y., Kwon, O.-H. and Kim, B.-S., 2018. Carbon Dots: Bottom-Up Syntheses, Properties, and Light-Harvesting Applications. *Chemistry - An Asian Journal*, 13(6), pp.586–598.

Chong, M.N., Jin, B., Chow, C.W.K. and Saint, C., 2010. Recent developments in photocatalytic water treatment technology: A review. *Water Research*, 44(10), pp.2997–3027.

De, B. and Karak, N., 2013. A green and facile approach for the synthesis of water soluble fluorescent carbon dots from banana juice. *RSC Advances*, 3(22), pp.8286–8290.

Deng, Y. and Zhao, R., 2015. Advanced Oxidation Processes (AOPs) in Wastewater Treatment. *Current Pollution Reports*, 1(3), pp.167–176.

Dong, G., Zhang, Y., Pan, Q. and Qiu, J., 2014. A fantastic graphitic carbon nitride (g-C₃N₄) material: Electronic structure, photocatalytic and photoelectronic properties. *Journal of Photochemistry and Photobiology C: Photochemistry Reviews*, 20(1), pp.33–50.

Dong, H., Zeng, G., Tang, L., Fan, C., Zhang, C., He, X. and He, Y., 2015. An overview on limitations of TiO₂-based particles for photocatalytic degradation of organic pollutants and the corresponding countermeasures. *Water Research*, 79, pp.128–146.

Eatemadi, A., Daraee, H., Karimkhanloo, H., Kouhi, M., Zarghami, N., Akbarzadeh, A., Abasi, M., Hanifehpour, Y. and Joo, S.W., 2014. Carbon nanotubes: properties, synthesis, purification, and medical applications. *Nanoscale research letters*, 9(1), p.393.

Emam, A.N., Loutfy, S.A., Mostafa, A.A., Awad, H. and Mohamed, M.B., 2017. Cyto-toxicity, biocompatibility and cellular response of carbon dots–plasmonic based nano-hybrids for bioimaging. *RSC Advances*, 7(38), pp.23502–23504.

Fadllan, A., Marwoto, P., Aji, M.P., Susanto and Iswari, R.S., 2017. Synthesis of carbon nanodots from waste paper with hydrothermal method. *AIP Conference Proceedings*, 1788.

Farshbaf, M., Davaran, S., Rahimi, F., Annabi, N., Salehi, R. and Akbarzadeh, A., 2018. Carbon quantum dots: recent progresses on synthesis, surface modification and applications. *Artificial Cells, Nanomedicine and Biotechnology*, 46(7), pp.1331–1348.

Foster, H.A., Ditta, I.B., Varghese, S. and Steele, A., 2011. Photocatalytic disinfection using titanium dioxide: spectrum and mechanism of antimicrobial activity. *Applied Microbiology and Biotechnology*, 90(6), pp.1847–1868.

Gao, X., Du, C., Zhuang, Z. and Chen, W., 2016. Carbon quantum dot-based nanoprobes for metal ion detection. *Journal of Materials Chemistry C*, 4(29), pp.6927–6945.

García, H. and Navalón, S., 2017. *Nanoparticles for Catalysis*. 1st ed. Switzerland: MDPI AG.

Gore, A.C., Crews, D., Doan, L.L., Merrill, M. La, Patisaul, H. and Zota, A., 2014. *Introduction to Endocrine Disrupting Chemicals (EDCs) a Guide For Public Interest Organizations and Policy-makers*. Texas:Endocrine Society.

Guo, Y., Zhang, L., Cao, F. and Leng, Y., 2016. Thermal treatment of hair for the synthesis of sustainable carbon quantum dots and the applications for sensing Hg²⁺. *Scientific Reports*, 6(1), p.35795.

He, J., 2015. *Preparation and Photocatalysis of Graphite Carbon Nitride Based Photocatalysts*. MPhil.Curtin University. Available at: <<https://espace.curtin.edu.au/handle/20.500.11937/521>> [Accessed 10 Aug. 2018]

He, M., Zhang, J., Wang, H., Kong, Y., Xiao, Y. and Xu, W., 2018. Material and Optical Properties of Fluorescent Carbon Quantum Dots Fabricated from Lemon Juice via Hydrothermal Reaction. *Nanoscale Research Letters*, 13(1), p.175.

Hebbelstrup Jensen, B., Olsen, K.E.P., Struve, C., Krogfelt, K.A. and Petersen, A.M., 2014. Epidemiology and clinical manifestations of enteroaggregative *Escherichia coli*. *Clinical microbiology reviews*, 27(3), pp.614–30.

Helmfrid, I., Berglund, M., Löfman, O. and Wingren, G., 2012. Health effects and exposure to polychlorinated biphenyls (PCBs) and metals in a contaminated community. *Environment International*, 44, pp.53–58.

Himaja, A.L., Karthik, P.S. and Singh, S.P., 2015. Carbon Dots: The Newest Member of the Carbon Nanomaterials Family. *The Chemical Record*, 15(3), pp.595–615.

Huang, G., Chen, X., Wang, C., Zheng, H., Huang, Z., Chen, D. and Xie, H., 2017a. Photoluminescent carbon dots derived from sugarcane molasses: Synthesis, properties, and applications. *RSC Advances*, 7(75), pp.47840–47847.

Huang, G., Xia, D., An, T., Ng, T.W., Yip, H.Y., Li, G., Zhao, H. and Wong, P.K., 2015. Dual Roles of Capsular Extracellular Polymeric Substances in Photocatalytic Inactivation of *Escherichia coli*: Comparison of *E. coli* BW25113 and Isogenic Mutants. *Applied and Environmental Microbiology*, 81(15), pp.5174–5183.

Huang, Y.Q., Wong, C.K.C., Zheng, J.S., Bouwman, H., Barra, R., Wahlström, B., Neretin, L. and Wong, M.H., 2012. Bisphenol A (BPA) in China: A review of sources, environmental levels, and potential human health impacts. *Environment International*, 42, pp.91–99.

Ibhadon, A. and Fitzpatrick, P., 2013. Heterogeneous Photocatalysis: Recent Advances and Applications. *Catalysts*, 3(1), pp.189–218.

Jang, J., Hur, H.-G., Sadowsky, M.J., Byappanahalli, M.N., Yan, T. and Ishii, S.,

2017. Environmental *Escherichia coli*: ecology and public health implications-a review. *Journal of Applied Microbiology*, 123(3), pp.570–581.

Jhonsi, M.A., Ananth, D.A., Nambirajan, G., Sivasudha, T., Yamini, R., Bera, S. and Kathiravan, A., 2018. Antimicrobial activity, cytotoxicity and DNA binding studies of carbon dots. *Spectrochimica Acta - Part A: Molecular and Biomolecular Spectroscopy*, 196, pp.295–302.

Kabasenche, W.P. and Skinner, M.K., 2014. DDT, epigenetic harm, and transgenerational environmental justice. *Environmental Health*, 13(1), p.62.

Kang, X., Kang, Y., Hong, X., Sun, Z., Zhen, C., Hu, C., Liu, G. and Cheng, H., 2018. Improving the photocatalytic activity of graphitic carbon nitride by thermal treatment in a high-pressure hydrogen atmosphere. *Progress in Natural Science: Materials International*, 28(2), pp.183–188.

Kasibabu, B.S.B., D'souza, S.L., Jha, S. and Kailasa, S.K., 2015. Imaging of Bacterial and Fungal Cells Using Fluorescent Carbon Dots Prepared from Carica papaya Juice. *Journal of Fluorescence*, 25(4), pp.803–810.

Ke, J., Li, X., Zhao, Q., Liu, B., Liu, S. and Wang, S., 2017. Upconversion carbon quantum dots as visible light responsive component for efficient enhancement of photocatalytic performance. *Journal of Colloid and Interface Science*, 496, pp.425–433.

Khan, M.M., Adil, S.F. and Al-Mayouf, A., 2015a. Metal oxides as photocatalysts. *Journal of Saudi Chemical Society*, 19(5), pp.462–464.

Khan, M.M., Adil, S.F. and Al-Mayouf, A., 2015b. Metal oxides as photocatalysts. *Journal of Saudi Chemical Society*, 19(5), pp.462–464.

Khor, J.M., 2018. Synthesis and Characterization of Dried Leaves Derived Carbon Quantum Dots For Metal Ions Sensing and Photocatalytic Application. Ph.D. Universiti Tunku Abdul Rahman.

Konieczna, A., Rutkowska, A. and Rachoń, D., 2015. Health risk of exposure to Bisphenol A (BPA). *Roczniki Panstwowego Zakladu Higieny*, 66(1), pp.5–11.

Korajkic, A., McMinn, B.R., Harwood, V.J., Shanks, O.C., Fout, G.S. and Ashbolt, N.J., 2013. Differential decay of enterococci and *Escherichia coli* originating from two fecal pollution sources. *Applied and environmental microbiology*, 79(7), pp.2488–2492.

Krishnan, S., Rawindran, H., Sinnathambi, C.M. and Lim, J.W., 2017. Comparison of various advanced oxidation processes used in remediation of industrial wastewater laden with recalcitrant pollutants. *IOP Conference Series: Materials Science and Engineering*, 206, pp.1–7.

Kumar, P., Boukherroub, R. and Shankar, K., 2018. Sunlight-driven water-splitting using two-dimensional carbon based semiconductors. *Journal of Materials*

Chemistry A, 6(27), pp.12876–12931.

Kumar, S., Karthikeyan, S. and Lee, A., 2018a. g-C₃N₄-Based Nanomaterials for Visible Light-Driven Photocatalysis. *Catalysts*, 8(2), pp.1–33.

Kumar, S., Karthikeyan, S. and Lee, A., 2018b. g-C₃N₄-Based Nanomaterials for Visible Light-Driven Photocatalysis. *Catalysts*, 8(2), p.74.

Lee, K.M., Lai, C.W., Ngai, K.S. and Juan, J.C., 2016. Recent developments of zinc oxide based photocatalyst in water treatment technology: A review. *Water Research*, 88, pp.428–448.

Li, J.-Y., Liu, Y., Shu, Q.-W., Liang, J.-M., Zhang, F., Chen, X.-P., Deng, X.-Y., Swihart, M.T. and Tan, K.-J., 2017. One-Pot Hydrothermal Synthesis of Carbon Dots with Efficient Up- and Down-Converted Photoluminescence for the Sensitive Detection of Morin in a Dual-Readout Assay. *Langmuir*, 33(4), pp.1043–1050.

Lim, J.Y., Yoon, J. and Hovde, C.J., 2010. A brief overview of Escherichia coli O157:H7 and its plasmid O157. *Journal of microbiology and biotechnology*, 20(1), pp.5–14.

Lim, S.Y., Shen, W. and Gao, Z., 2015. Carbon quantum dots and their applications. *Chemical Society Reviews*, 44(1), pp.362–381.

Lin, H., Ding, L., Zhang, B. and Huang, J., 2018. Detection of nitrite based on fluorescent carbon dots by the hydrothermal method with folic acid. *Royal Society Open Science*, 5(5), p.172149.

Lin, J., 2011. *Conventional Water Treatment Processes for Removing Pharmaceutical and Endocrine Disrupting Compounds*. PhD. University of Massachusetts Amherst.

Lv, S., Li, Y., Zhang, K., Lin, Z. and Tang, D., 2017. Carbon Dots/g-C₃N₄ Nanoheterostructures-Based Signal-Generation Tags for Photoelectrochemical Immunoassay of Cancer Biomarkers Coupling with Copper Nanoclusters. *ACS Applied Materials and Interfaces*, 9(44), pp.38336–38343.

Maeda, K. and Domen, K., 2010. Photocatalytic Water Splitting: Recent Progress and Future Challenges. *The Journal of Physical Chemistry Letters*, 1(18), pp.2655–2661.

Mewada, A., Pandey, S., Shinde, S., Mishra, N., Oza, G., Thakur, M., Sharon, M. and Sharon, M., 2013. Green synthesis of biocompatible carbon dots using aqueous extract of *Trapa bispinosa* peel. *Materials Science & Engineering C*, 33(5), pp.2914–2917.

Miller, T.S., Jorge, A.B., Suter, T.M., Sella, A., Corà F. and McMillan, P.F., 2017. Carbon nitrides: Synthesis and characterization of a new class of functional materials. *Physical Chemistry Chemical Physics*, 19(24), pp.15613–15638.

Molinari, R., Argurio, P., Bellardita, M. and Palmisano, L., 2017. 3.5 Photocatalytic Processes in Membrane Reactors. In: *Comprehensive Membrane Science and Engineering*. Elsevier, pp.101–138.

Monneret, C., 2017. What is an endocrine disruptor? *Comptes Rendus Biologies*, 340(9–10), pp.403–405.

Mujtaba, I.M., Srinivasan, R. and Elbashir, N.O., 2017. *The water-food-energy nexus : processes, technologies, and challenges*. Boca Raton: CRC Press.

Myers, J.A., Curtis, B.S. and Curtis, W.R., 2013. Improving accuracy of cell and chromophore concentration measurements using optical density. *BMC Biophysics*, 6 (1), pp. 4-15.

Nazarkovsky, M.A., Bogatyrov, V.M., Czech, B., Galaburda, M.V., Wójcik, G., Kolomys, O.F., Strelchuk, V.V., Malysheva, M.L., Oranska, O.I. and Gun'ko, V.M., 2017. Synthesis and properties of zinc oxide photocatalyst by high-temperature processing of resorcinol-formaldehyde/zinc acetate mixture. *Journal of Photochemistry and Photobiology A: Chemistry*, 334, pp.36–46.

O'Shea, K.E. and Dionysiou, D.D., 2012. Advanced Oxidation Processes for Water Treatment. *The Journal of Physical Chemistry Letters*, 3(15), pp.2112–2113.

Ochoa, T.J. and Contreras, C.A., 2011. Enteropathogenic escherichia coli infection in children. *Current opinion in infectious diseases*, 24(5), pp.478–83.

Okhuysen, P.C. and DuPont, H.L., 2010. Enteroaggregative *Escherichia coli* (EAEC): A Cause of Acute and Persistent Diarrhea of Worldwide Importance. *The Journal of Infectious Diseases*, 202(4), pp.503–505.

Ong, W.J., Tan, L.L., Ng, Y.H., Yong, S.T. and Chai, S.P., 2016. Graphitic Carbon Nitride (g-C₃N₄)-Based Photocatalysts for Artificial Photosynthesis and Environmental Remediation: Are We a Step Closer to Achieving Sustainability? *Chemical Reviews*, 116(12), pp.7159–7329.

Ouyang, K., Dai, K., Walker, S.L., Huang, Q., Yin, X. and Cai, P., 2016. Efficient Photocatalytic Disinfection of *Escherichia coli* O157:H7 using C70-TiO₂ Hybrid under Visible Light Irradiation. *Scientific reports*, 6, p.25702.

Palaniappan, R.U.M., Zhang, Y., Chiu, D., Torres, A., Debroy, C., Whittam, T.S. and Chang, Y.-F., 2006. Differentiation of *Escherichia coli* pathotypes by oligonucleotide spotted array. *Journal of clinical microbiology*, 44(4), pp.1495–501.

Pawar, R.C. and Lee, C.S., 2015. *Heterogeneous nanocomposite-photocatalysis for water purification*. United States: William Andrew Publishing.

Qu, D., Liu, J., Miao, X., Han, M., Zhang, H., Cui, Z., Sun, S., Kang, Z., Fan, H. and Sun, Z., 2018. Peering into water splitting mechanism of g-C₃N₄-carbon dots metal-free photocatalyst. *Applied Catalysis B: Environmental*, 227, pp.418–424.

- Ravishankar, T.N., Ramakrishnappa, T., Nagaraju, G. and Rajanaika, H., 2015. Synthesis and Characterization of CeO₂ Nanoparticles via Solution Combustion Method for Photocatalytic and Antibacterial Activity Studies. *ChemistryOpen*, 4(2), pp.146–147.
- Ribeiro, E., Ladeira, C. and Viegas, S., 2017. Occupational Exposure to Bisphenol A (BPA): A Reality That Still Needs to Be Unveiled. *Toxics*, 5(3), p.22.
- Sahu, S., Behera, B., Maiti, T.K. and Mohapatra, S., 2012. Simple one-step synthesis of highly luminescent carbon dots from orange juice: application as excellent bio-imaging agents. *Chemical Communications*, 48(70), p.8835.
- El Saliby, I., McDonagh, A., Erdei, L. and Kyong Shon, H., 2016. Water Reclamation by Heterogeneous Photocatalysis over Titanium Dioxide. In: *Green Technologies for Sustainable Water Management*. Reston, VA: American Society of Civil Engineers, pp.679–704.
- Schneider, J., Bahnemann, D. (Detlef), Ye, J., Puma, G.L. and Dionysiou, D.D., 2016. *Photocatalysis: fundamentals and perspectives*. United States: Royal Society of Chemistry.
- Scruggs, C., Hunter, G., Snyder, E., Long, B., Shane Snyder, V. and Nevada Water Authority Caroline Scruggs, S., 2004. *EDCS in wastewater: What's the Next Step?* Kansas: Water Environment Federation.
- Shon, H.K., Phuntsho, S., Okour, Y., Cho, D.L., Kim, J.B., Na, S. and Kim, J.-H., 2008. *Visible Light Responsive Titanium Dioxide (TiO₂)-a review*, 19(1), pp.1-16
- Sun, X. and Lei, Y., 2017. Fluorescent carbon dots and their sensing applications. *TrAC Trends in Analytical Chemistry*, 89, pp.163–180.
- Tai, J.Y., Leong, K.H., Saravanan, P. and Sim, L.C., 2018. Bioinspired Synthesis of Carbon Dots/g-C₃N₄ Nanocomposites for Photocatalytic Application. *E3S Web of Conferences*, 65, p.05015.
- Tan, X.W., Romainor, A.N.B., Chin, S.F. and Ng, S.M., 2014. Carbon dots production via pyrolysis of sago waste as potential probe for metal ions sensing. *Journal of Analytical and Applied Pyrolysis*, 105, pp.157–165.
- Umar, M. and Aziz, H.A., 2013. Photocatalytic Degradation of Organic Pollutants in Water. 13, pp.169-203.
- Vasimalai, N., Vilas-Boas, V., Gallo, J., Cerqueira, M. de F., Menéndez-Miranda, M., Costa-Fernández, J.M., Diéguez, L., Espiña, B. and Fernández-Argüelles, M.T., 2018. Green synthesis of fluorescent carbon dots from spices for in vitro imaging and tumour cell growth inhibition. *Beilstein Journal of Nanotechnology*, 9(1), pp.530–544.
- Vermeulen, N., Keeler, W.J., Nandakumar, K. and Leung, K.T., 2008. The bactericidal effect of ultraviolet and visible light on *Escherichia coli*. *Biotechnology*

and *Bioengineering*, 99(3), pp.550–556.

Wang, A., Wang, C., Fu, L. and Yucheng, W.W., 2017a. Recent Advances of Graphitic Carbon Nitride-Based Structures and Applications in Catalyst, Sensing, Imaging, and LEDs. *Applied Catalysis B: Environmental*, 194, pp. 1–21.

Wang, F., Chen, P., Feng, Y., Xie, Z., Liu, Y., Su, Y., Zhang, Q., Wang, Y., Yao, K., Lv, W. and Liu, G., 2017b. Facile synthesis of N-doped carbon dots/g-C₃N₄ photocatalyst with enhanced visible-light photocatalytic activity for the degradation of indomethacin. *Applied Catalysis B: Environmental*, 207, pp.103–113.

Wang, F., Chen, P., Feng, Y., Xie, Z., Liu, Y., Su, Y., Zhang, Q., Wang, Y., Yao, K., Lv, W. and Liu, G., 2017c. Facile synthesis of N-doped carbon dots/g-C₃N₄ photocatalyst with enhanced visible-light photocatalytic activity for the degradation of indomethacin. *Applied Catalysis B: Environmental*, 207, pp.103–113.

Wang, J., Li, C., Zhuang, H. and Zhang, J., 2013a. Photocatalytic degradation of methylene blue and inactivation of Gram-negative bacteria by TiO₂ nanoparticles in aqueous suspension. *Food Control*, 34(2), pp.372–377.

Wang, R., Li, G., Dong, Y., Chi, Y. and Chen, G., 2013b. Carbon Quantum Dot-Functionalized Aerogels for NO₂ Gas Sensing. *Analytical Chemistry*, 85(17), pp.8065–8069.

Wang, W.J., Yu, J.C. and Wong, P.K., 2012. Photocatalysts for Solar-Induced Water Disinfection: New Developments and Opportunities. *Materials Science Forum*, 734, pp.63–89.

Wang, X., Cheng, J., Yu, H. and Yu, J., 2017d. A facile hydrothermal synthesis of carbon dots modified g-C₃N₄ for enhanced photocatalytic H₂-evolution performance. *Dalton Transactions*, 46(19), pp.6417–6424.

Wang, X., Cheng, J., Yu, H. and Yu, J., 2017e. A facile hydrothermal synthesis of carbon dots modified g-C₃N₄ for enhanced photocatalytic H₂-evolution performance. *Dalton Transactions*, 46(19), pp.6417–6424.

Wang, Y. and Hu, A., 2014. Carbon quantum dots: synthesis, properties and applications. *Journal of Materials Chemistry C*, 2(34), p.6921.

Wen, J., Xie, J., Chen, X. and Li, X., 2017. A review on g-C₃N₄-based photocatalysts. *Applied Surface Science*, 391, pp.72–76.

Wen, X., Yu, P., Toh, Y.R., Ma, X. and Tang, J., 2014. On the upconversion fluorescence in carbon nanodots and graphene quantum dots. *Chemical Communications*, 50(36), pp.4703–4706.

Wong, J.L., 2017. Synthesis and Characterization of Sugarcane Juice Derived Carbon Dots/G-C₃N₄ Composite. PhD. University Tunku Abdul Rahman.

Wu, Z.L., Liu, Z.X. and Yuan, Y.H., 2017. Carbon dots: materials, synthesis,

properties and approaches to long-wavelength and multicolor emission. *Journal of Materials Chemistry B*, 5(21), pp.3794–3809.

Xin, G. and Meng, Y., 2013. Pyrolysis synthesized g-C₃N₄ for photocatalytic degradation of methylene blue. *Journal of Chemistry*, 2013, pp.1-5.

Xu, B., Ahmed, M.B., Zhou, J.L., Altaee, A., Xu, G. and Wu, M., 2018. Graphitic carbon nitride based nanocomposites for the photocatalysis of organic contaminants under visible irradiation: Progress, limitations and future directions. *Science of The Total Environment*, 633, pp.546–559.

Xu, X., Ray, R., Gu, Y., Ploehn, H.J., Gearheart, L., Raker, K. and Scrivens, W.A., 2004. Electrophoretic Analysis and Purification of Fluorescent Single-Walled Carbon Nanotube Fragments. *Journal of the American Chemical Society*, 126(40), pp.12736–12737.

Yan, S.C., Li, Z.S. and Zou, Z.G., 2009. Photodegradation Performance of g-C₃N₄ Fabricated by Directly Heating Melamine. *Langmuir*, 25(17), pp.10397–10401.

Yang, Y., Cui, J., Zheng, M., Hu, C., Tan, S., Xiao, Y., Yang, Q. and Liu, Y., 2012. One-step synthesis of amino-functionalized fluorescent carbon nanoparticles by hydrothermal carbonization of chitosan. *Chem. Commun.*, 48(3), pp.380–382.

Yang, Y., Wu, D., Han, S., Hu, P. and Liu, R., 2013. Bottom-up fabrication of photoluminescent carbon dots with uniform morphology via a soft–hard template approach. *Chemical Communications*, 49(43), p.4920.

Yasmina, M., Mourad, K., Mohammed, S.H. and Khaoula, C., 2014. Treatment Heterogeneous Photocatalysis; Factors Influencing the Photocatalytic Degradation by TiO₂. *Energy Procedia*, 50, pp.559–566.

Yong, Z., Ren, J., Hu, H., Li, P., Ouyang, S., Xu, H. and Wang, D., 2015. Synthesis , Characterization , and Photocatalytic Activity of g-C₃N₄/KTaO₃ Composites under Visible Light Irradiation. *Journal of Nanomaterials*, 2015, pp.1–7.

Yu, B.Y. and Kwak, S.-Y., 2012. Carbon quantum dots embedded with mesoporous hematite nanospheres as efficient visible light-active photocatalysts. *Journal of Materials Chemistry*, 22(17), p.8345.

Yu, C., Xuan, T., Chen, Y., Zhao, Z., Sun, Z. and Li, H., 2015. A facile, green synthesis of highly fluorescent carbon nanoparticles from oatmeal for cell imaging. *Journal of Materials Chemistry C*, 3(37), pp.9514–9518.

Zeng, Q., Shao, D., He, X., Ren, Z., Ji, W., Shan, C., Qu, S., Li, J., Chen, L. and Li, Q., 2016. Carbon dots as a trackable drug delivery carrier for localized cancer therapy in vivo. *Journal of Materials Chemistry B*, 4(30), pp.5119–5126.

Zhai, X., Zhang, P., Liu, C., Bai, T., Li, W., Dai, L. and Liu, W., 2012. Highly luminescent carbon nanodots by microwave-assisted pyrolysis. *Chemical Communications*, 48(64), p.7955.

Zhang, B., Liu, C. and Liu, Y., 2010. A Novel One-Step Approach to Synthesize Fluorescent Carbon Nanoparticles. *European Journal of Inorganic Chemistry*, 2010(28), pp.4411–4414.

Zhang, H., Ming, H., Lian, S., Huang, H., Li, H., Zhang, L., Liu, Y., Kang, Z. and Lee, S.-T., 2011. Fe₂O₃/carbon quantum dots complex photocatalysts and their enhanced photocatalytic activity under visible light. *Dalton Transactions*, 40(41), p.10822.

Zhang, J. and Yu, S.-H., 2016. Carbon dots: large-scale synthesis, sensing and bioimaging. *Materials Today*, 19(7), pp.382–393.

Zhang, Z., Zheng, T., Xu, J. and Zeng, H., 2017. Carbon Quantum Dots / Bi₂WO₆ Composites for Efficient Photocatalytic Pollutant Degradation and Hydrogen Evolution. 12(7), pp.1–9.

Zhao, Z., Ma, Y., Fan, J., Xue, Y., Chang, H., Masubuchi, Y. and Yin, S., 2018. Synthesis of graphitic carbon nitride from different precursors by fractional thermal polymerization method and their visible light induced photocatalytic activities. *Journal of Alloys and Compounds*, 735, pp.1297–1305.

Zhao, Z., Sun, Y. and Dong, F., 2015. Graphitic carbon nitride based nanocomposites: a review. *Nanoscale*, 7(1), pp.15–37.

Zhu, C., Zhai, J. and Dong, S., 2012. Bifunctional fluorescent carbon nanodots: green synthesis via soy milk and application as metal-free electrocatalysts for oxygen reduction. *Chemical Communications*, 48(75), p.9367.

Zhu, J., Xiao, P., Li, H. and Carabineiro, S.A.C., 2014. Graphitic Carbon Nitride: Synthesis, Properties, and Applications in Catalysis. *ACS Applied Materials & Interfaces*, 6(19), pp.16449–16465.

Zhu, S. and Wang, D., 2017. Photocatalysis: Basic Principles, Diverse Forms of Implementations and Emerging Scientific Opportunities. *Advanced Energy Materials*, 7(23), pp.4–6.

Zhu, S., Zhang, J., Tang, S., Qiao, C., Wang, L., Wang, H., Liu, X., Li, B., Li, Y., Yu, W., Wang, X., Sun, H. and Yang, B., 2012. Surface chemistry routes to modulate the photoluminescence of graphene quantum dots: From fluorescence mechanism to up-conversion bioimaging applications. *Advanced Functional Materials*, pp.1–7.

Zhu, Y.-P., Ren, T.-Z. and Yuan, Z.-Y., 2015. Mesoporous Phosphorus-Doped g-C₃N₄ Nanostructured Flowers with Superior Photocatalytic Hydrogen Evolution Performance. *ACS Applied Materials & Interfaces*, 7(30), pp.16850–16856.

Zuo, J., Jiang, T., Zhao, X., Xiong, X., Xiao, S. and Zhu, Z., 2015. Preparation and Application of Fluorescent Carbon Dots. *Journal of Nanomaterials*, 2015, pp.1–13.

APPENDICES

APPENDIX A: Sample Calculations

Preparation of *E.coli* stock solution at 1×10^9 CFU/mL

The *E.coli* cultured was dilute with different dilutions of 1 (original *E.coli* solution), 1/2, 1/4, 1/8, 1/16 to plot the calibration curve. In order to prepare *E.coli* stock solution of 1×10^9 CFU/mL, OD₆₀₀ by spectrophotometer was used to identify the absorbance at different dilutions. For *E.coli* culture, OD₆₀₀ of 1 represent 8×10^8 CFU/mL of solution (Myers, Curtis and Curtis, 2013). Figure A shows the absorbance vs dilution.

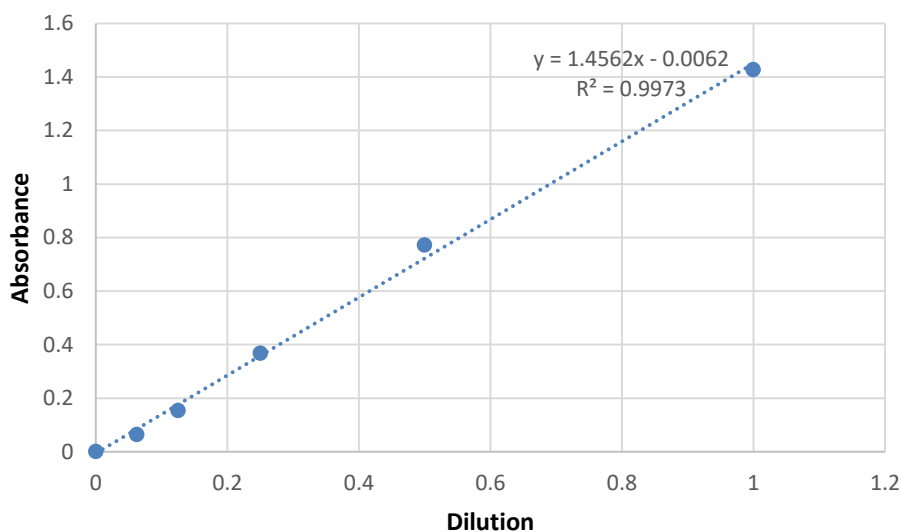


Figure A: Absorbance against Dilution of cultured *E.coli* solution

Since OD₆₀₀ of 1 = 8×10^8 cells

$$\text{Absorbance of } 1 \times 10^9 \text{ cells} = \frac{1 \times 10^9}{8 \times 10^8} = 1.25$$

Based on Equation of the line graph:

$$\text{Absorbance} = 1.4562 \text{ Dilution} - 0.0062$$

$$1.25 = 1.4562 \text{ Dilution} - 0.0062$$

$$\text{Dilution} = 0.8627$$

$$\text{Dilution factor, DF} = \frac{1}{0.8627}$$

Therefore, in order to prepare *E.coli* stock solution with 1×10^9 CFU/mL and with a final volume, $V_{final} = 50$ mL:

$$DF = \frac{V_{final}}{V_{initial}}$$

$$\frac{1}{0.8627} = \frac{50}{V_{initial}}$$

$$V_{initial} = 43.135 \text{ mL}$$

Therefore, 43.135 mL of cultured *E.coli* solution was topped up until 50 mL to prepare *E.coli* stock solution with 1×10^9 CFU/mL. The stock solution was then used to prepare the *E.coli* samples used for the experiment.

Determination of Number of Viable *E.coli*

Sample Calculation: Number of viable *E.coli* in blank solution at $t = 30$ min with dilution of 10^{-4}

Number of colony in agar plate = 60

Dilution = 10^{-4}

$$\text{Number of viable } E. coli / \text{mL} = \frac{\text{number of colony in agar plate}}{\text{dilution} \times \text{volume plated (mL)}}$$

$$\text{Number of viable } E. coli / \text{mL} = \frac{60}{10^{-4} \times 0.1} = 6,000,000 \text{ cells/mL}$$

Preparation of CDs/g-C₃N₄ Composites

Sample Calculation: CDs/g-C₃N₄ (0.10)

To synthesise the CDs/g-C₃N₄ composite with 10 wt.% of CDs, the CDs required to couple with 1 g of g-C₃N₄ was calculated as follow:

$$\frac{\text{mass of CDs required}}{\text{Total mass of composite}} = 0.1$$

$$\frac{\text{mass of CDs required}}{1 + \text{mass of CDs required}} = 0.1$$

$$\text{mass of CDs required} = 0.1111 \text{ g}$$

Preparation of BPA solution with different concentrations from stock solution of 100 ppm (mg/L)

Sample calculation: 20 ppm BPA solution

$$C_1V_1 = C_2V_2$$

Where

C_1 = Concentration of stock solution, ppm

V_1 = Volume of stock solution, mL

C_2 = Concentration of diluted solution, ppm

V_2 = Volume of diluted solution, mL

$$100V_1 = 20 (200)$$

$$V_1 = 40 \text{ mL of stock solution}$$

∴ 40 mL of stock solution (100 ppm) has to be added into 160 mL of distilled water to produce 200 mL of BPA solution with 20 ppm.

Determination of the Photodegradation Rate of Photocatalysts

Sample Calculation: Photocatalytic degradation of BPA by CDs/g-C₃N₄ (0.20)

$$\text{Photodegradation rate, \%} = \frac{C_0 - C}{C_0} \times 100 \%$$

$$\text{Initial BPA concentration, } C_0 = \frac{133190 - 18596}{133190} \times 100 \% = 86.04 \%$$

APPENDIX B: EDX Results

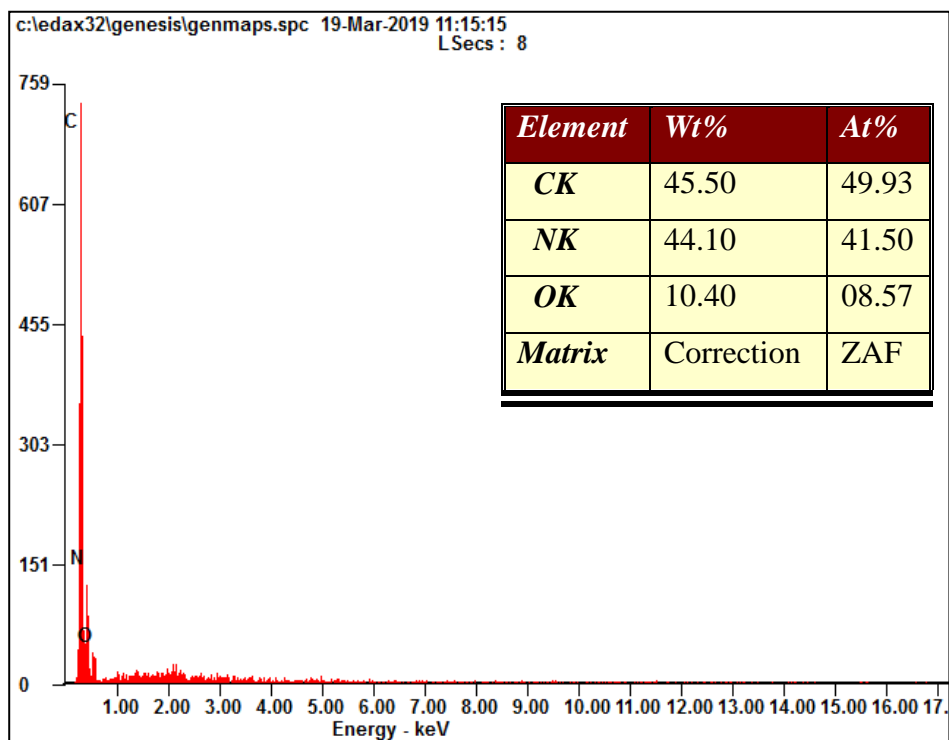


Figure B-1: EDX Result of g-C₃N₄

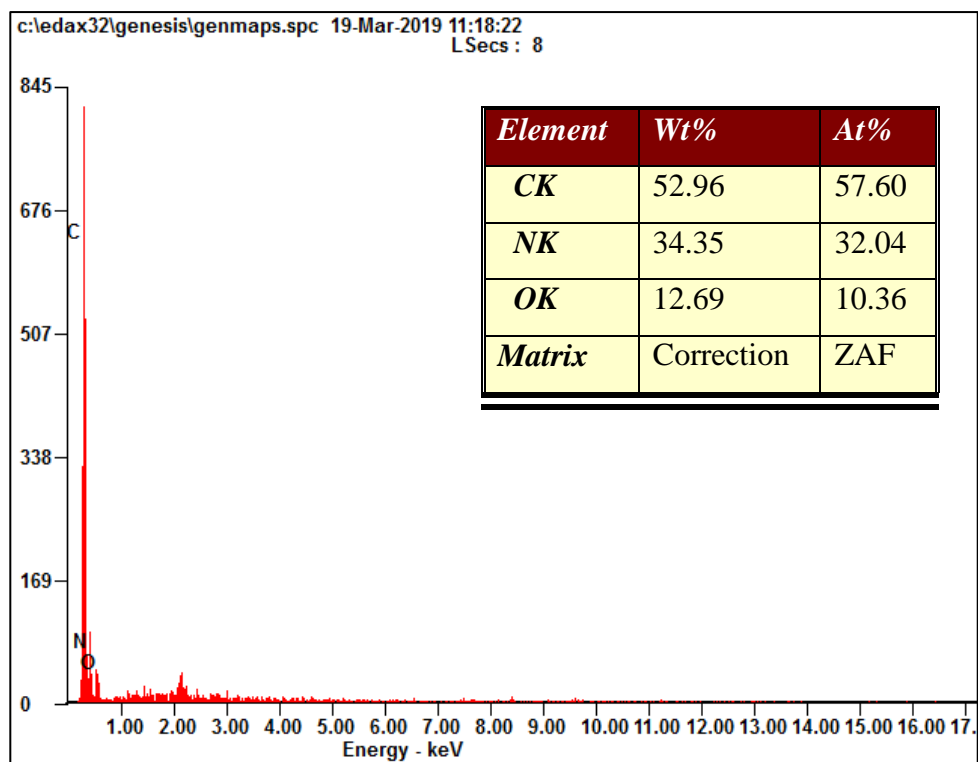
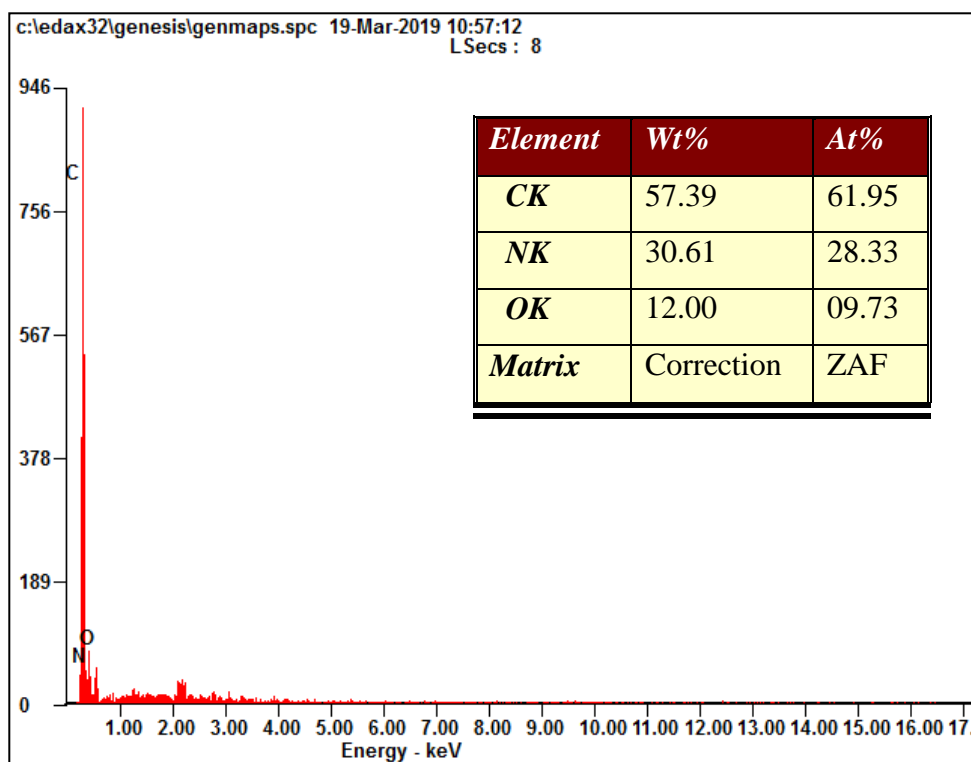
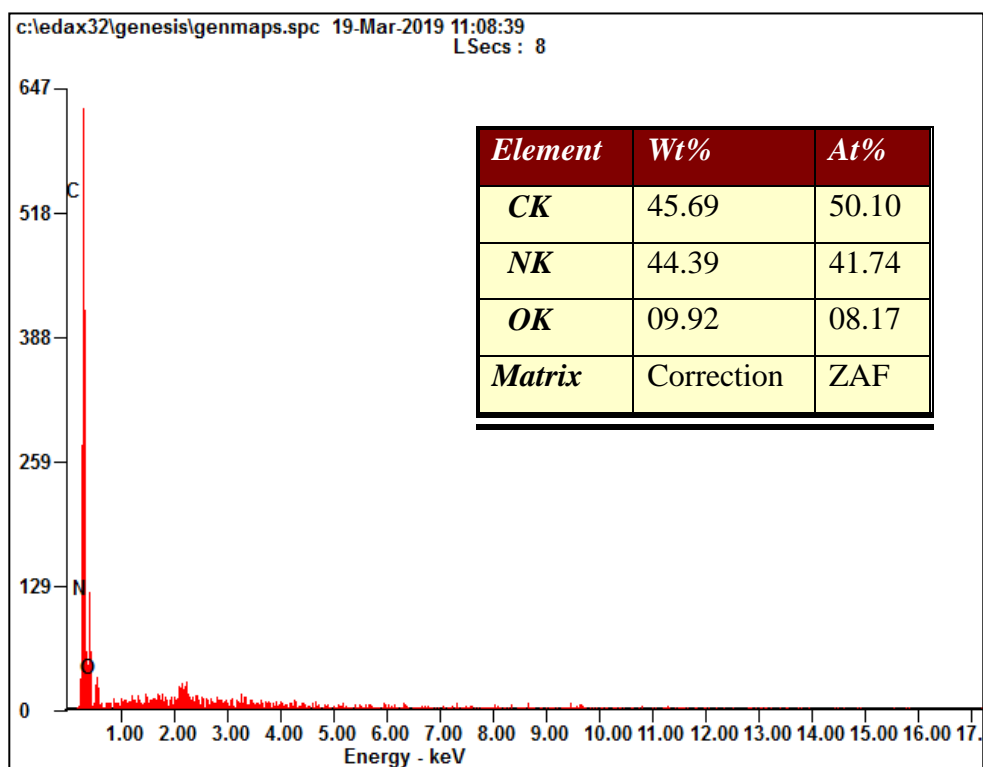


Figure B-2: EDX Result of CDs/g-C₃N₄ (0.10)

Figure B-3: EDX Result of CDs/g-C₃N₄ (0.15)Figure B-4: EDX Result of CDs/g-C₃N₄ (0.20)

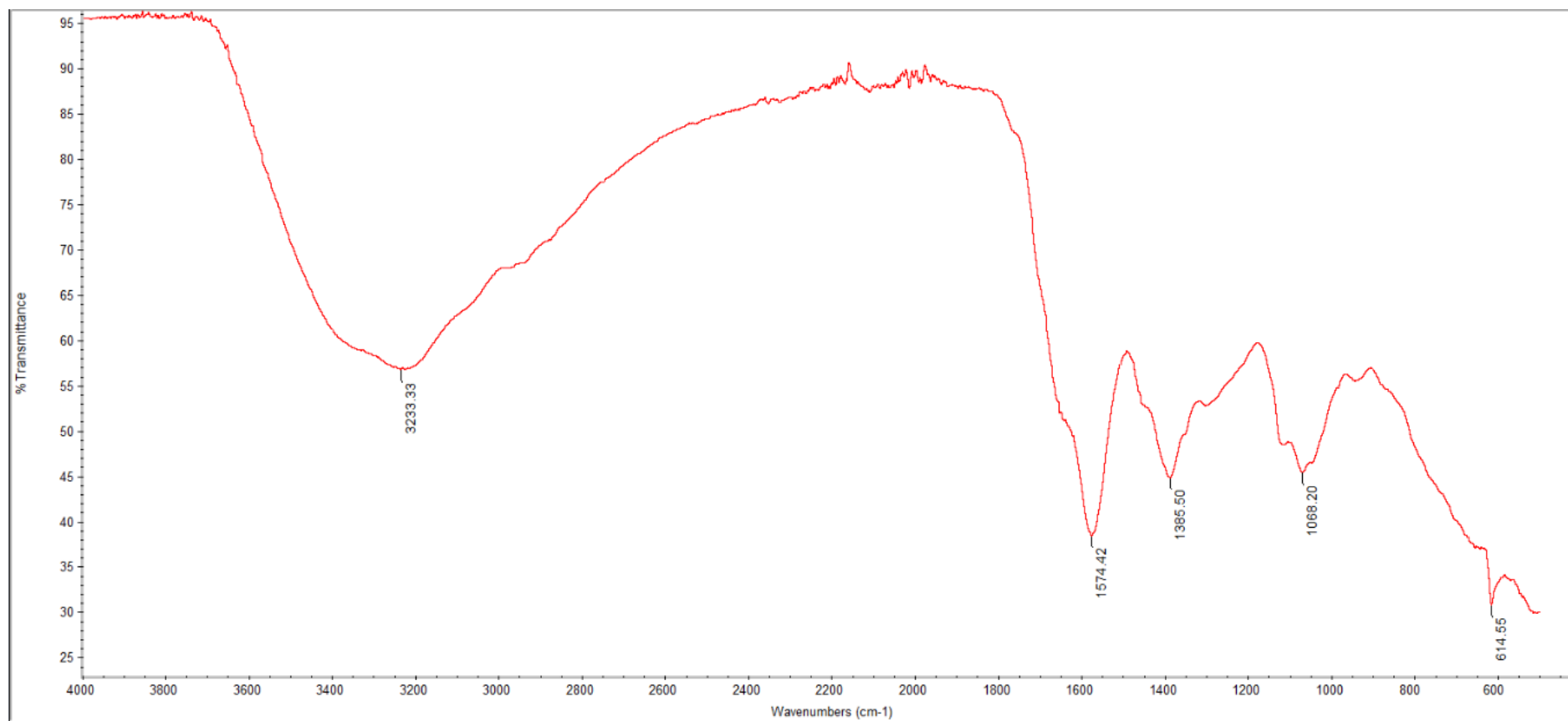
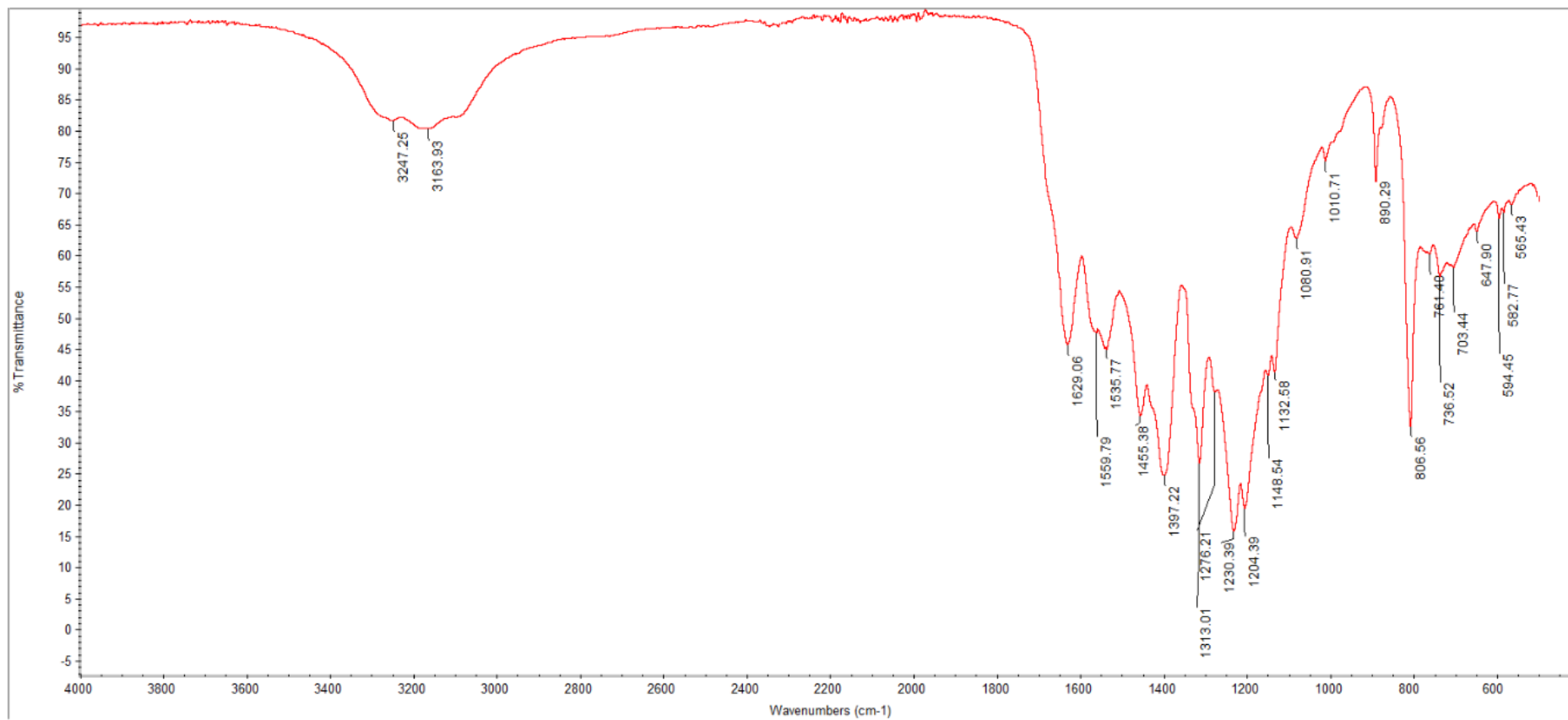
APPENDIX C: FTIR Results

Figure C-1: FTIR Spectra of CDs

Figure C-2: FTIR Spectra of g-C₃N₄

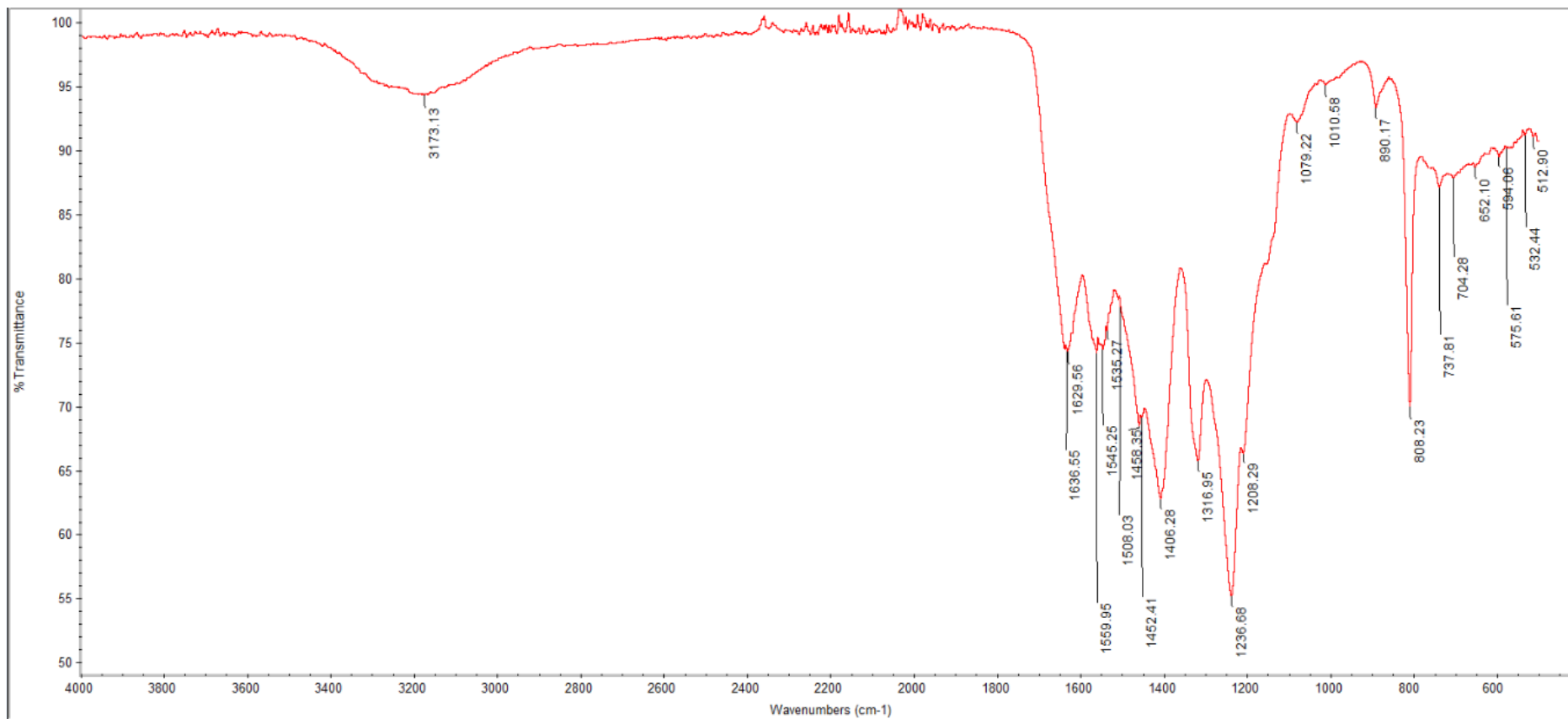


Figure C-3: FTIR Spectra of CDs/g-C₃N₄ (0.10)

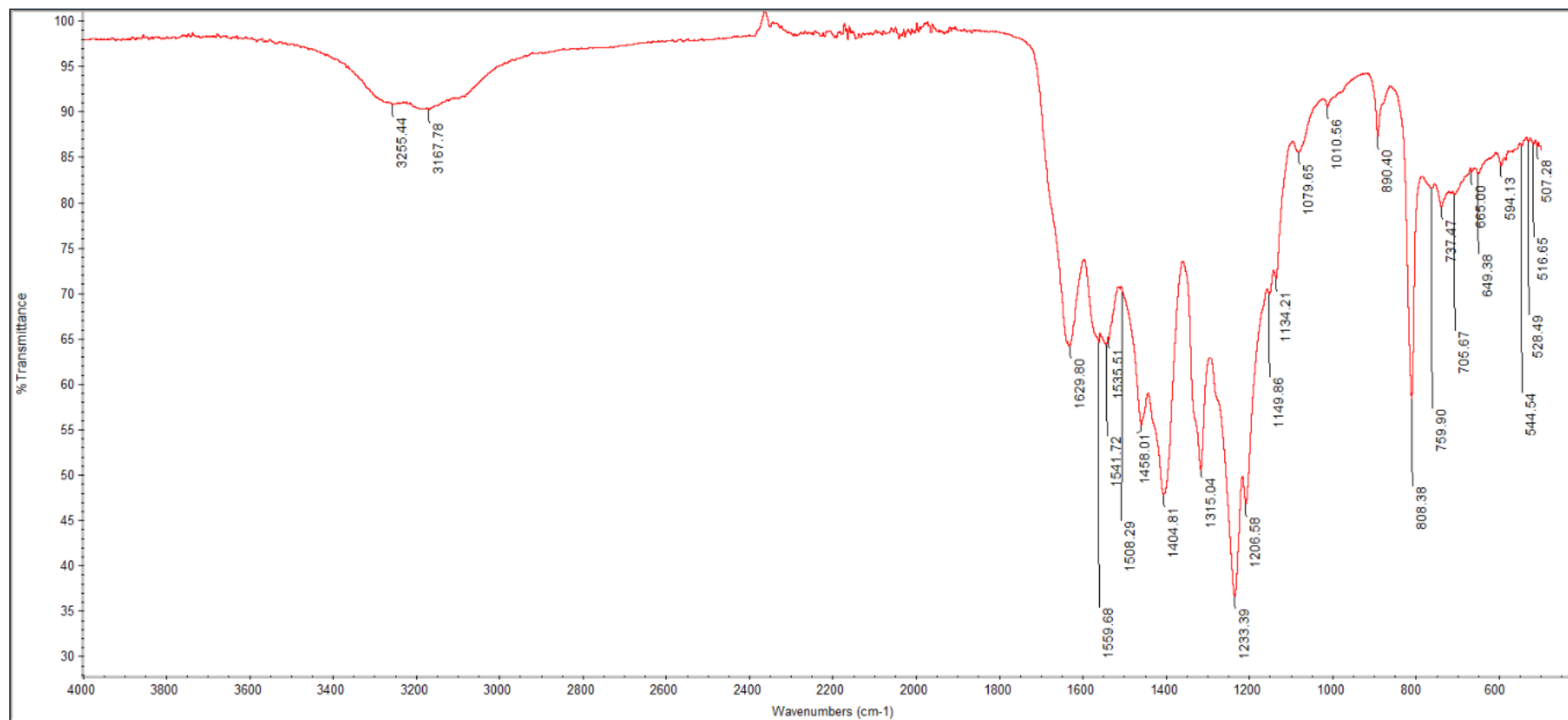


Figure C-4: FTIR Spectra of CDs/g-C₃N₄ (0.15)

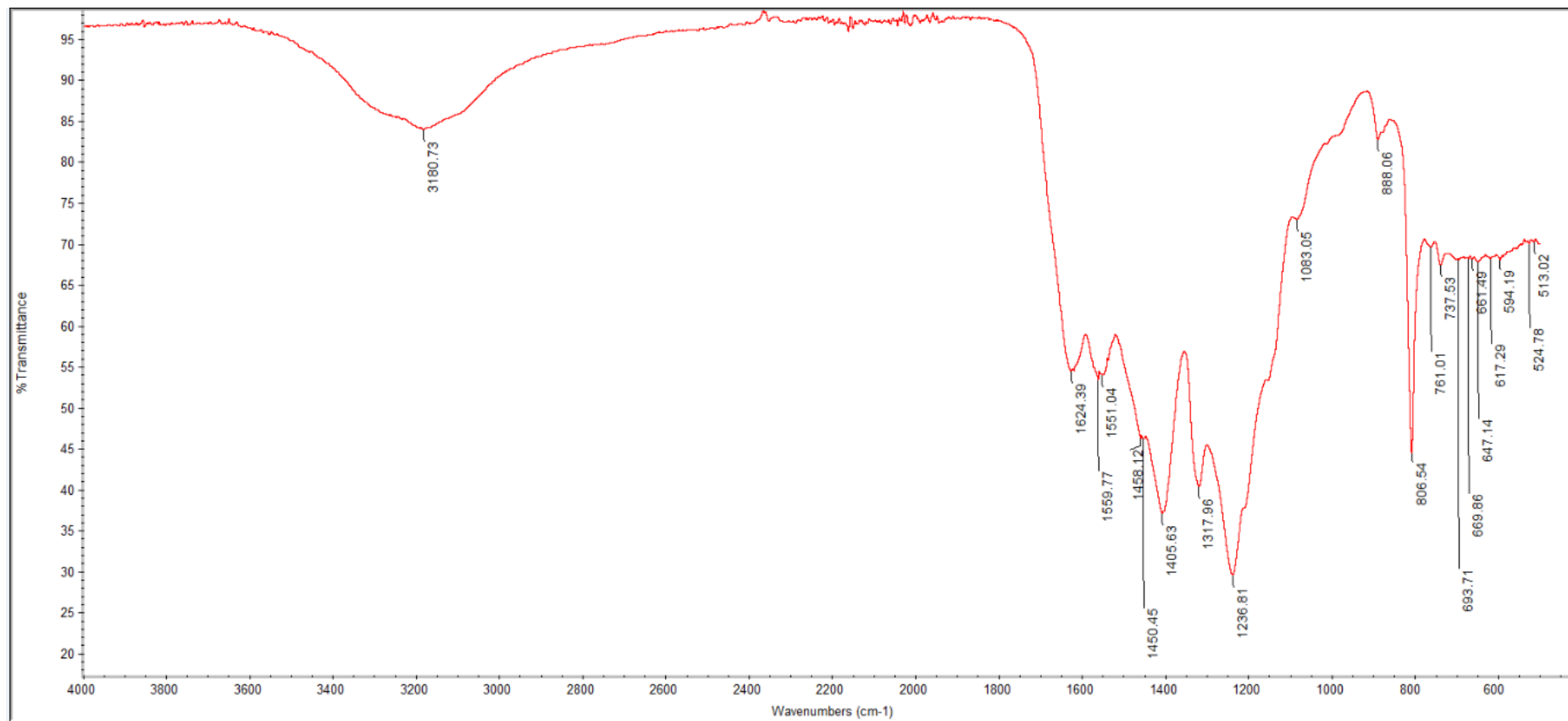
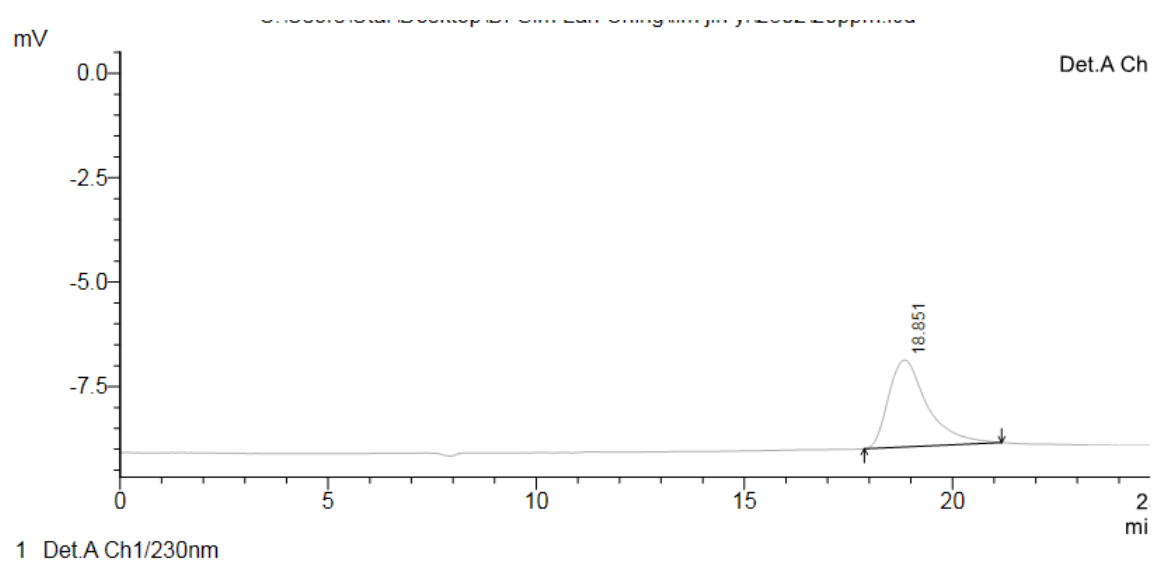


Figure C-5: FTIR Spectra of CDs/g-C₃N₄ (0.20)

APPENDIX D: HPLC Results



1 Det.A Ch1/230nm

PeakTable					
Detector A Ch1 230nm					
Peak#	Ret. Time	Area	Height	Area %	Height %
1	18.851	135257	2077	100.000	100.000
Total		135257	2077	100.000	100.000

Figure D: HPLC Result for Calibration curve (20 ppm BPA solution)

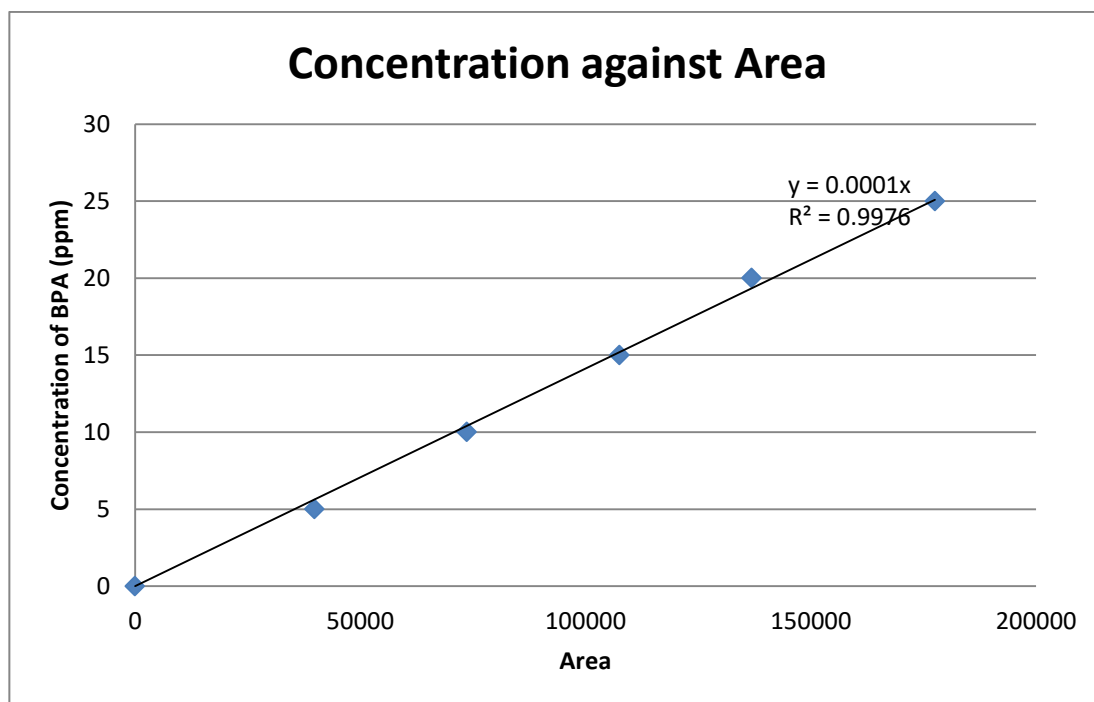
APPENDIX E: Calibration Curve of BPA Concentration

Figure E: HPLC Calibration Curve for BPA Concentration

APPENDIX F: XRD Results

```

*** Basic Data Process ***

Group      : DrSim
Data       : g-C3N4

# Strongest 3 peaks
no. peak   2Theta      d      I/I1    FWHM      Intensity  Integrated Int
           (deg)      (Å)    (deg)    (deg)     (Counts)  (Counts)
1         6      27.1290   3.28430  100    1.73800    672    53206
2        13      77.7316   1.22757   62    0.57090    415    11668
3        12      64.5532   1.44249   50    0.59180    337     8170

# Peak Data List
peak      2Theta      d      I/I1    FWHM      Intensity  Integrated Int
no.      (deg)      (Å)    (deg)    (deg)     (Counts)  (Counts)
1        12.9000   6.85710   6    1.44000     42     2990
2        14.4400   6.12908   4    1.96000     26     4997
3        23.5000   3.78262   4    1.16000     28     3058
4        24.1200   3.68678   6    0.00000     40         0
5        25.3600   3.50925  19    1.20000    125    11246
6        27.1290   3.28430  100    1.73800    672    53206
7        29.0400   3.07238  12    1.00000     78     5900
8        29.8800   2.98789   5    0.76000     33     1678
9        37.8849   2.37294  43    0.58790    286     8090
10       44.1435   2.04994  28    0.59290    188     6271
11       63.6800   1.46015   3    2.80000     22     4793
12       64.5532   1.44249  50    0.59180    337     8170
13       77.7316   1.22757  62    0.57090    415    11668

```

Figure F-1: XRD Result of g-C₃N₄

```

*** Basic Data Process ***

Group      : DrSim
Data       : CD_g-C3N4_10

# Strongest 3 peaks
no. peak   2Theta      d      I/I1    FWHM      Intensity  Integrated Int
           (deg)      (Å)    I/I1    (deg)     (Counts)  (Counts)
1    20    64.6139    1.44128  100    0.15630    1477    13344
2    23    77.7781    1.22696   92    0.17120    1363    13061
3    11    27.3600    3.25710   29    0.00000     432      0

# Peak Data List
peak      2Theta      d      I/I1    FWHM      Intensity  Integrated Int
no.      (deg)      (Å)    I/I1    (deg)     (Counts)  (Counts)
1         25.5400    3.48492   4    0.22000     53    1054
2         25.7000    3.46359   4    0.00000     66      0
3         25.8600    3.44252   5    0.00000     77      0
4         25.9800    3.42689   7    0.00000    105      0
5         26.1400    3.40628  11    0.00000    158      0
6         26.3600    3.37835  13    0.00000    199      0
7         26.5800    3.35088  19    0.00000    276      0
8         26.7200    3.33364  21    0.00000    313      0
9         26.9600    3.30451  27    0.00000    398      0
10        27.1600    3.28062  29    0.00000    430      0
11        27.3600    3.25710  29    0.00000    432      0
12        27.6400    3.22473  24    0.00000    356      0
13        27.8000    3.20654  21    0.00000    307      0
14        28.0200    3.18186  15    0.59720    224    4835
15        28.4200    3.13798   7    0.34500    104    1710
16        28.6600    3.11224   4    0.00000     63      0
17        28.8000    3.09743   4    0.20000     52     931
18        37.9574    2.36858  27    0.15630    394    3918
19        44.2114    2.04695  15    0.15970    227    2422
20        64.6139    1.44128  100    0.15630    1477    13344
21        64.9000    1.43562   8    0.14620    114    1586
22        77.3600    1.23254   4    0.17460     58    1132
23        77.7781    1.22696   92    0.17120    1363    13061
24        78.1600    1.22191   9    0.16160    130    1733

```

Figure F-2: XRD Results of CDs/g-C₃N₄ (0.10)

```

*** Basic Data Process ***

Group      : DrSim
Data       : CD_g-C3N4_15

# Strongest 3 peaks
no. peak   2Theta      d      I/I1    FWHM      Intensity  Integrated Int
no.        (deg)         (Å)                    (deg)      (Counts)   (Counts)
  1      18      64.5893     1.44177   100     0.15150     1435     11673
  2      20      77.7536     1.22728    96     0.16530     1378     13385
  3      14      37.9258     2.37048    33     0.14740      467      3805

# Peak Data List
peak       2Theta      d      I/I1    FWHM      Intensity  Integrated Int
no.        (deg)         (Å)                    (deg)      (Counts)   (Counts)
  1      26.0800     3.41398    3     0.17780      46       695
  2      26.3200     3.38339    7     0.17340      94       715
  3      26.5600     3.35336   12     0.41720     171     2499
  4      26.7000     3.33609   16     0.00000     230        0
  5      26.9000     3.31174   22     0.00000     322        0
  6      27.1800     3.27826   27     0.00000     390        0
  7      27.3800     3.25476   27     0.00000     389        0
  8      27.5000     3.24083   26     0.00000     378        0
  9      27.6400     3.22473   24     0.00000     347        0
 10      27.7600     3.21107   20     0.60860     290     5478
 11      28.2600     3.15538    7     0.22660     101     1286
 12      28.4400     3.13582    4     0.13000      63       589
 13      37.7400     2.38172    5     0.10500      69       656
 14      37.9258     2.37048   33     0.14740     467     3805
 15      38.4217     2.34101    4     0.13440      54       542
 16      44.1799     2.04833   20     0.15570     282     2779
 17      64.2000     1.44957    3     0.16000      49       906
 18      64.5893     1.44177   100     0.15150     1435     11673
 19      64.8800     1.43601    6     0.18000      82      1573
 20      77.7536     1.22728    96     0.16530     1378     13385
 21      78.1435     1.22213    7     0.17100     107     1465

```

Figure F-3: XRD Results of CDs/g-C₃N₄ (0.15)

```

*** Basic Data Process ***

Group      : DrSim
Data       : CD_g-C3N4_20

# Strongest 3 peaks
no. peak   2Theta      d      I/I1    FWHM      Intensity  Integrated Int
          no.      (deg)    (Å)      (deg)    (Counts)  (Counts)
  1     19     64.5157    1.44324  100     0.14740    1054      8898
  2     22     77.6895    1.22813   97     0.16840    1021     10096
  3     13     37.8349    2.37596   40     0.15250     417      3653

# Peak Data List
peak      2Theta      d      I/I1    FWHM      Intensity  Integrated Int
no.      (deg)    (Å)      (deg)    (Counts)  (Counts)
  1      26.0000    3.42430    5     0.08400     53        454
  2      26.3800    3.37583   11     0.34860    114       1884
  3      26.8000    3.32387   23     0.67280    245       6268
  4      27.0600    3.29252   27     0.00000    284         0
  5      27.2400    3.27117   27     0.00000    280         0
  6      27.4000    3.25243   24     0.00000    254         0
  7      27.5800    3.23161   20     0.00000    216         0
  8      27.7000    3.21788   16     0.00000    165         0
  9      27.8800    3.19752   12     0.00000    122         0
 10      28.0200    3.18186    7     0.18660     76         827
 11      28.1800    3.16415    4     0.30220     44         534
 12      37.6000    2.39026    4     0.09720     40         406
 13      37.8349    2.37596   40     0.15250    417       3653
 14      38.3940    2.34264    8     0.13200     84         674
 15      44.0977    2.05196   27     0.15220    280       2523
 16      44.3000    2.04306    4     0.09100     43         273
 17      44.6841    2.02638    3     0.15830     34         383
 18      64.1000    1.45159    3     0.10860     34         512
 19      64.5157    1.44324  100     0.14740   1054      8898
 20      64.8200    1.43720    5     0.12580     57         644
 21      65.0543    1.43259    3     0.13140     36         334
 22      77.6895    1.22813   97     0.16840   1021     10096
 23      78.1015    1.22268    7     0.21850     71        1125

```

Figure F-4: XRD Results of CDs/g-C₃N₄ (0.20)